A New Feature of the Quiet Sun Corona During Solar Minimum

by

Zhenguang Huang

A dissertation submitted in partial fulfillment
of the requirements for the degree of
Doctor of Philosophy
(Atmospheric, Oceanic and Space Sciences and Scientific Computing)
in the University of Michigan
2014

Doctoral Committee:

Professor Tamas I. Gombosi, Co-Chair
Associate Research Scientist Richard A. Frazin, Co-Chair
Associate Professor Susan T. Lepri
Research Associate Professor Ward B. Manchester IV
Professor Kenneth G. Powell
Associate Research Scientist Bartholomeus van der Holst

To my family,

My parents Ziyuan Huang and Guoying Zhang

ACKNOWLEDGEMENTS

First and foremost, I would like to express my deepest gratitude to my advisors, Dr. Tamas I. Gombosi and Dr. Richard A. Frazin, for their valuable guidance and support throughout my graduate study. I have been really fortunate to have them as my advisors, who are exceptionally intelligent and knowledgeable in space science, especially in solar physics. I have benefited so much from them. They have showed me how to be a good scientist, how to explore problems logically, and how to prepare scientific manuscripts.

I would like to thank the rest of my dissertation committee: Dr. Susan T. Lepri, Dr. Ward B. Manchester IV, Dr. Kenneth G. Powell, and Dr. Bartholomeus van der Holst, for serving on my committee and providing insightful suggestions on my research. I especially would like to thank Dr. Bartholomeus van der Holst and Dr. Ward B. Manchester IV, for their help in numerical simulations of the solar corona and inspiring discussions in science.

I would like to thank my collaborators, Dr. Alberto M. Vásquez and Federico A. Nuevo, in Argentina . I appreciate their help in providing the DEMT data and valuable conservations.

My sincere thanks also go to the the rest of professors, scientists, and research fellows in the department of Atmospheric, Oceanic and Space Sciences. I especially would like to thank Dr. Gábor Tóth and Dr. Enrico Landi. Dr. Gábor Tóth helped me a lot in numerical simulations; while Dr. Enrico Landi provided me a global picture of the quiet Sun study.

I would like to thank the administrative staff, for their assistant in various paperwork. I am also grateful to the IT group, for their quick response and help whenever my desktop had issues.

I would like to thank all my friends, for their friendship and support. Special thanks to my officemates, who have provided a family-like atmosphere.

Last but not the least, I would like to thank my family, especially my parents Ziyuan Huang and Guoying Zhang, for their love, understanding, and support. I would not have accomplished my Ph.D. without them.

TABLE OF CONTENTS

LIST OF FIGURES

Figure

LIST OF TABLES

Table

ABSTRACT

A New Feature of the Quiet Sun Corona During Solar Minimum

by

Zhenguang Huang

Co-Chairs: Tamas I. Gombosi and Richard A. Frazin

Quiet Sun (QS) loops have received much less attention than active region loops, partly due to the relative difficulty in identifying individual QS loop structures. However, understanding the physical processes that heat the quiet corona is critically important, as the quiet corona overlies most of the Sun's surface (especially during solar minimum). To study QS loops, we developed a novel technique called Michigan Loop Diagnostic Technique (MLDT). MLDT combines Differential Emission Measure Tomography and a potential field source surface model to obtain the electron temperature and density at each point along a QS loop.

We applied MLDT to study QS loops using EUVI/STEREO and MDI/SOHO observations taken during Carrington Rotation (CR) 2077. The MLDT identified two types of QS loops: "Up Loops" (UL) in which the temperature increases with height, and "Down Loops" (DL) in which the temperature decreases with height. DLs are ubiquitous in the low-latitude ($\pm 30°$latitude) quiescent corona, while ULs dominate at higher latitudes. ULs have been widely observed and studied in active regions. The identification of DLs was a surprise in solar physics and these loops constitute a new class of plasma structures populating the solar corona.

The discovery of DLs is not widely accepted as the community considers DLs are unstable against thermal instabilities. To address the thermal stability, we performed time-accurate 3D MHD simulations, first creating DLs by increasing the heating near the footpoints, and then imposing a small pressure perturbation near the apex. The evolution of the DL returned to its steady state solution about three hours after the perturbation, thus confirming that DLs are thermodynamically stable against small pressure perturbations.

We further studied DLs properties in 11 CRs to reveal more properties of DLs. DLs are always found to be located at low latitudes and are anti-correlated with sunspot numbers; moreover, they had systematically larger values of plasma beta than ULs.

Down loops are a newly discovered structure of the quiet Sun corona during solar minimum that may shed light on the physics of coronal heating: the coronal heating is enhanced near the footpoints of DLs while the heating is more uniform in ULs.

CHAPTER I

Introduction

The Sun, the closest star to the Earth, plays an essential role in the solar system. Studying the Sun is important not only because it is closely related to daily human life, but also because it is an ideal laboratory where we can test our knowledge in physics under various conditions. One of the most challenging questions in solar physics asks how the corona is being heated. The solar corona is the Sun's outer atmosphere; it extends to very large heliocentric distances. It was believed that the corona was in a similar temperature range as the photosphere, where the temperature is about 6000K calculated from a black body radiation, until *Grotrian* (1939) realized the corona reaches a very high temperature (more than 10^6K) when he studied the spectral lines observed from the solar corona. The science community was shocked because the corona is heated to more than two orders of magnitude higher within several thousand kilometers and no theories at that time could explain the heating.

As we will see later in this dissertation, understanding the coronal heating is critical because it is closely related to the solar wind acceleration. The solar wind is a stream of plasma from the Sun that fills all the space within the solar system. The solar wind is the core of the Sun-Earth environment affecting space weather predictions because eruptive events on the Sun, such as coronal mass ejections (CMEs), travel along the solar wind. When these events hit the earth's magnetosphere, they can

cause geomagnetic storms and generate geomagnetically induced currents in electric systems. Large geomagnetically induced currents can result in electric blackouts and such an event is called a space weather event. One famous space weather event is the Quebec blackout which lasted over nine hours and affected several million people.

Tremendous attention has been paid to the coronal heating problem but it is still highly debated. The aim of this dissertation is to understand the coronal heating problem, more specifically, in quiet Sun (QS) corona. For historical reasons which we will discuss later in this chapter, the QS corona receives much less attention in coronal heating studies. We argue that the QS corona is as important as the active regions, as it should share similar physical processes that heat the active regions. The motivation of this dissertation is to fill the gap in our knowledge of the coronal heating problem by studying the heating processes in the quiet corona. We start our discussions by reviewing some basic background about the Sun's atmosphere.

1.1 The Structure of the Sun's Atmosphere

Unlike the Earth, which has a solid surface, it is tricky to define the surface of the Sun because the Sun is a gas star. Scientists define the surface of the Sun as the location where the optical depth at a $\lambda = 5,000$Å is unity. The Sun's atmosphere then can be separated into 4 layers as shown in Figure 1.1: the photosphere, the chromosphere, the transition region (which is not shown in the figure) and the corona. The temperature and density profile in the Sun's atmosphere is displayed in Figure 1.2. We will discuss the properties of each layer in the following subsections.

1.1.1 The Photosphere

The photosphere can be considered as the apparent solar surface when viewing in visible light. Figure 1.3 is a typical image of the photosphere. The photosphere starts from the surface of the Sun to about 500km above and it is the layer which can be

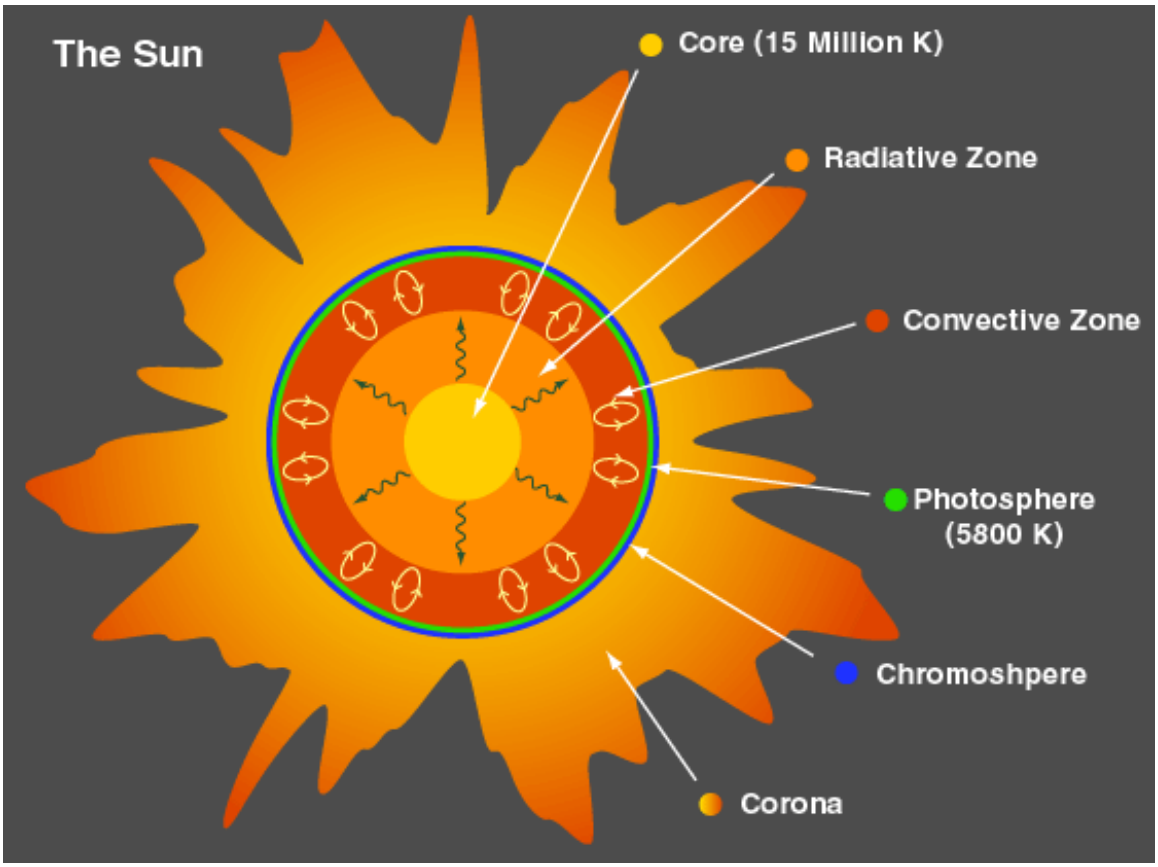

Figure 1.1: A cut-view of the structure of the Sun (from `http://blogs.agu.org/martianchronicles/2010/05/28/solar-system-tour-the-sun/`)

seen in white-light observations. Most of the Sun's radiation is emitted in this layer. The effective temperature (which is calculated from the blackbody temperature by the Stefan-Boltzmann law) of the photosphere is around 5800K, except the regions called sunspots where the effective temperature is around 4500K. As suggested in Figure 1.2, the temperature monotonically decreases with height in this layer. The lowest temperature is about 4300K, located at the interface of the photosphere and the chromosphere. The reason for this temperature decrease is that there are no heating sources in this layer. The radiative cooling is important in this layer while the heat conduction is less important as the temperature is relatively low.

The density in this layer drops from 10^{12} to $10^{10}\mathrm{cm}^{-3}$ shown in Figure 1.2. The

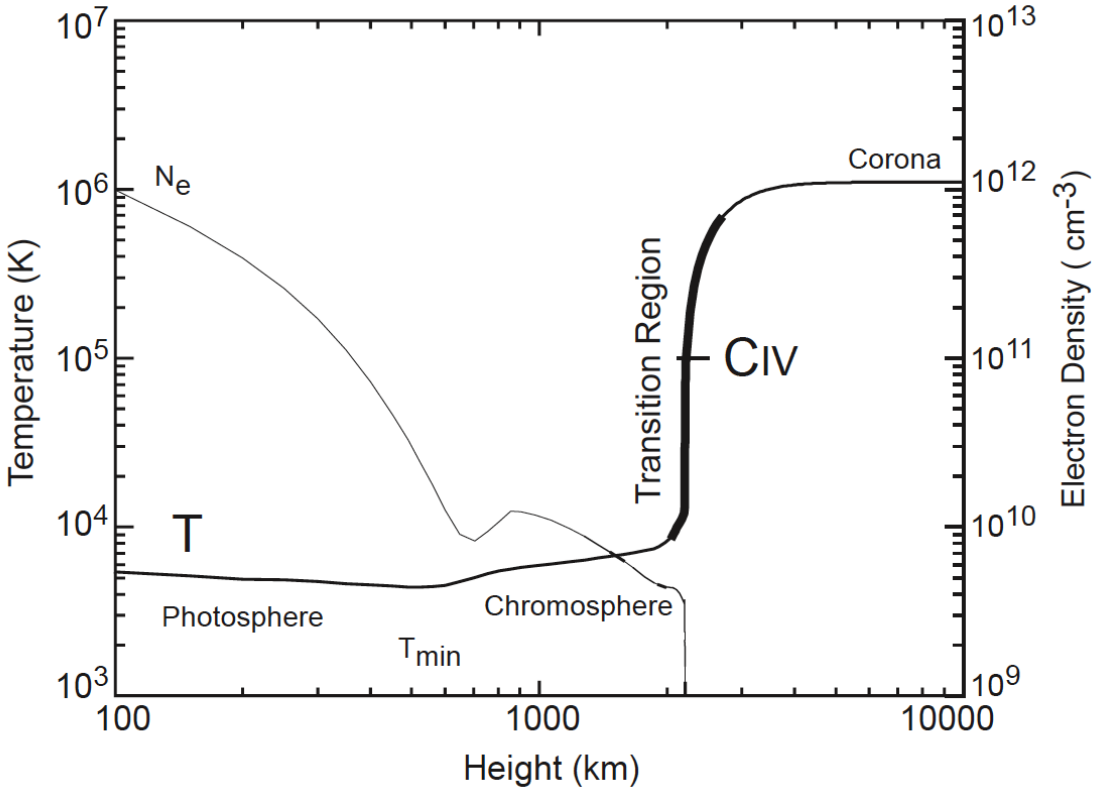

Figure 1.2: The temperature and density profile in the Sun's atmosphere (from *Gary et al.* (2007)).

gas is considered to be in hydrostatic equilibrium, which means the pressure gradient balances gravity. In this thin layer, the stratified solution (neglecting all horizontal variations) for the plasma density is

$$n(h) = n(0)\exp(-\frac{h}{H_p}) \tag{1.1}$$

where n is the number density of the gas, h is the height and H_p is the hydrostatic scale height given by $H_p = kT/\bar{m}g$, k is the Boltzmann constant, T is the temperature, $\bar{m}$ is the mean molecular mass and g is the local gravitational acceleration.

About 90% of the molecules are hydrogen while 9% of them are from helium. The remaining 1% come from all other heavy elements like Ca and Fe. The ionization

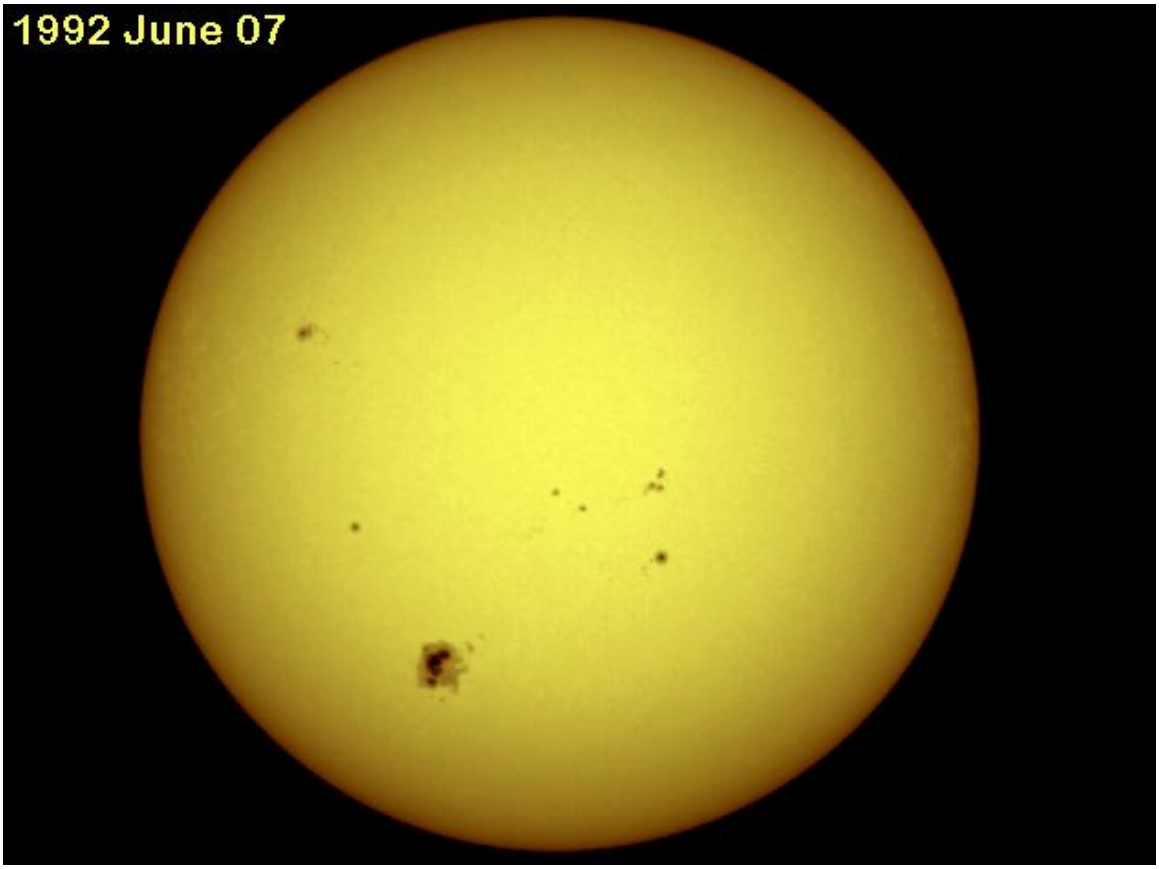

Figure 1.3: An image of the photosphere. (from `http://solarscience.msfc.nasa.gov/surface.shtml`). The black regions in the image are called sunspots.

rate in this layer is small due to the relatively low temperature, so the gas is treated mostly as neutral gas.

1.1.2 The Chromosphere

The chromosphere is the layer above the photosphere; it is transparent in visible light so we cannot see this layer in white-light observations. But the chromosphere is not transparent in other spectral lines, like the $H\alpha$ line or the CaII K line (they are also called the chromospheric emission lines). Some of those lines can be seen by human eyes, so the chromosphere can be observed in a solar eclipse for a very short time (around several seconds) during the eclipse totality. It is a brightly colored ring

very close to the solar limb and that is how this layer receives its name (color-sphere). The thickness of this layer is several thousand kilometers. In modern observations, the chromosphere is observed in either the $H\alpha$ line or the CaII K line. Figure 1.4 are two typical images of the chromosphere from two different wavelengths.

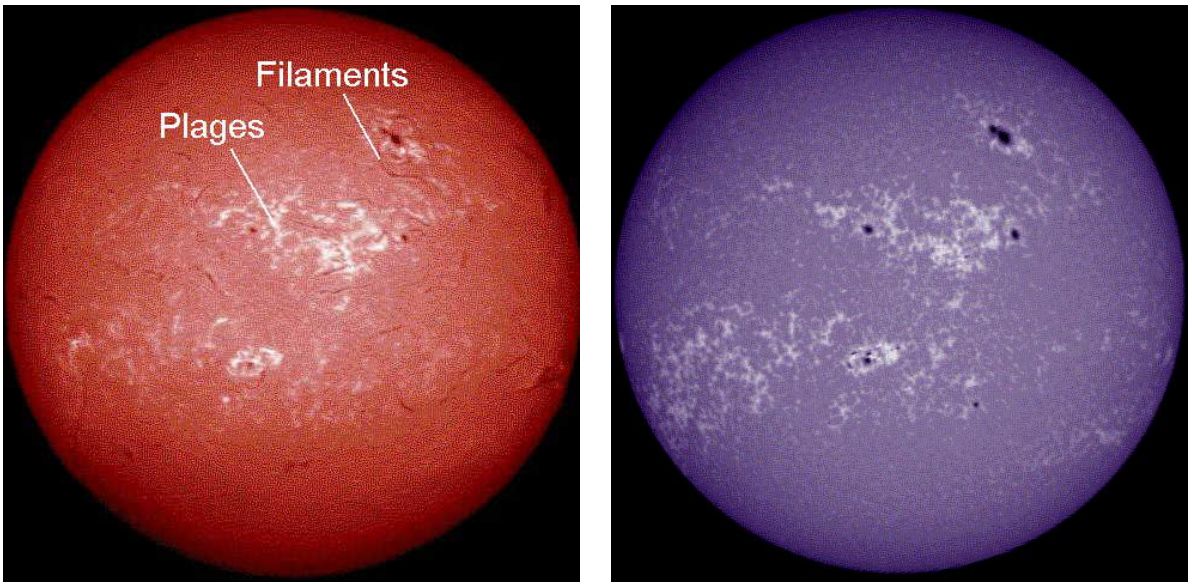

Figure 1.4: Two images of chromosphere: the left image is observed in the $H\alpha$ line while the right image is observed in the CaII K line. (from `http://www.astr.ua.edu/ay102/Lab7/Lab_7_Chromsphere.html`)

The temperature in the chromosphere increases from 4300K to 10^4K. The positive temperature gradient indicates that there are heating sources in this layer because otherwise the temperature will decrease like the photosphere. The heating mechanism in this region is not understood very well. Some models propose that the heating comes from acoustic waves (*Schatzman*, 1949; *Narain and Ulmschneider*, 1990; *Carlsson and Stein*, 1997; *Wedemeyer et al.*, 2004). In these models, the acoustic waves, which are generated by the convection motion in the convection zone, propagate outward into the photosphere and the chromosphere. In the photosphere, the energy deposition by acoustic waves is not important; while in the chromosphere, the density is low enough so the physical conditions may favor that the acoustic waves steepen into shocks and dissipate their energy to the chromosphere. *Wedemeyer et al.* (2004)

developed a 3-D radiation hydrodynamic model, which includes the acoustic waves excited by convection motions, and showed that the chromosphere can be heated by acoustic waves. Some other models suggest that in the chromosphere, the magnetic field becomes important so the MHD waves like Alfvén waves play an important role in the energy dissipation (*Osterbrock*, 1961; *Narain and Ulmschneider*, 1990). *van Ballegooijen et al.* (2011) developed a 3-D magnetohydrodynamic (MHD) model incorporating Alfvén turbulence dissipation as the heating source of the solar atmosphere and proposed that Alfvén turbulence is a candidate to heat the chromosphere.

1.1.3 The Transition Region

The transition region is a very thin layer that separates the chromosphere and the corona. The thickness of this layer is around 100km while the temperature increases rapidly from 10^4K to over 10^6K within this short distance. The physical process that can heat the material so quickly and still maintain this huge temperature gradient is the greatest mystery in solar physics. It is considered as the most complex layer in the solar atmosphere.

The heat conduction becomes important in this region as the temperature gradient is very high. The radiative loss in this layer is also important. Due to the high temperature, the ionization rate becomes high so the gas is considered as ionized gas starting from this region. The partially ionized gas in this layer is considered to be in non-local thermal equilibrium and requires more complex treatments than the relatively simple local thermal equilibrium equations.

1.1.4 The Corona

The corona, which extends from the transition region to very large heliocentric distance, is the outmost region of the Sun's atmosphere. At large heliocentric distance, the corona cannot be distinguished from the solar wind. The solar wind can extend

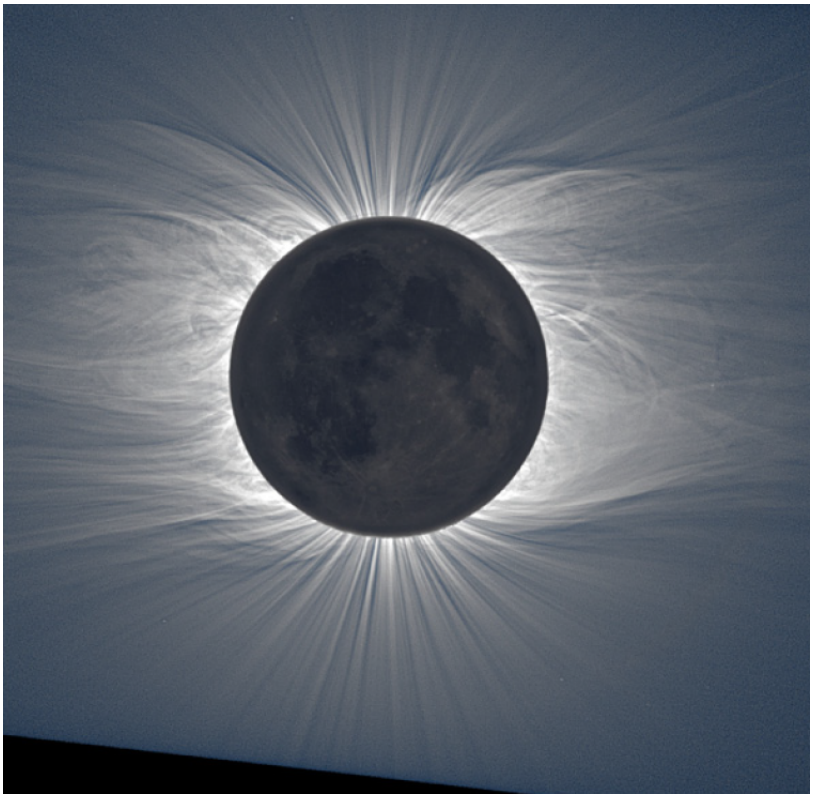

Figure 1.5: The lower corona during a total solar eclipse. (from *Pasachoff et al.* (2011)).

to around 100 AU (Astronomical Unit $\cong 1.5 \times 10^8$km), where the termination shock locates and is considered as the boundary of the solar system (*Burlaga et al.*, 2005; *Stone et al.*, 2008; *McComas et al.*, 2009). Figure 1.5 shows the lower corona during a total solar eclipse.

The temperature in the corona is very hot, from $1 \sim 2$MK in the quiet corona regions to $4 \sim 5$MK in the active regions. Due to the high temperature, the ionization rate in the corona is high so the corona is considered as fully ionized gas (plasma). Three physical processes are considered important in the corona: the heating source that can heat the corona to such a high temperature, the heat conduction and the radiative cooling. We will discuss the coronal heating problem in more detail in the next section.

1.2 The Coronal Heating Problem

Since *Grotrian* (1939) recognized the coronal spectral lines as belonging to highly ionized states of iron, understanding the physical process that can heat the corona to such a high temperature has been one of the hottest topics in solar physics. However, despite several decades of effort, the coronal heating problem remains one of the major open issues in solar physics.

There are two major directions to investigate the coronal heating problem. One approach studies the heating mechanism in closed magnetic field regions (coronal loops) (*Aschwanden and Schrijver*, 2002; *Klimchuk*, 2006; *Reale*, 2010) while the other approach associates the coronal heating problem and the solar wind problem, then seeks for a mechanism which can explain both the coronal heating and the solar wind acceleration (*Cranmer et al.*, 2007; *Cranmer*, 2009; *Chandran et al.*, 2011; *van der Holst et al.*, 2014). The coronal loop study emphasizes the loop properties observed in extreme ultraviolet images or x-ray images. The solar wind study pays more attention to the fast and slow solar wind properties, like the preferential heating in heavy ions, which the coronal loop study hardly considers.

In coronal loop study, scientists have proposed many mechanisms for heating the corona. Most of them can be separated into two different groups (*Reale*, 2010): Direct Current (DC) heating, and dissipation of waves as Alternating Current (AC) heating. In AC heating, it is assumed that magnetohydrodynamic (MHD) waves are damped by MHD turbulence, which dissipates energy through different mechanisms and heats the corona (*Osterbrock*, 1961; *Hollweg*, 1986; *O'Neill and Li*, 2005; *Ofman*, 2009). *Narain and Ulmschneider* (1996) pointed out that Alfvén waves are the best candidate because acoustic and slow-mode waves are strongly damped while fast-mode waves are strongly refracted and reflected. Alternatively, in DC heating, nanoflares (moderate and frequent explosive events) are responsible for the coronal heating (*Parker*, 1988; *Katsukawa and Tsuneta*, 2001; *Reale et al.*, 2005; *Klimchuk*, 2006; *Patsourakos and*

Klimchuk, 2006).

In solar wind study, two similar groups of models have been proposed (*Cranmer*, 2009): reconnection/loop-opening (RLO) models, and wave/turbulence-driven (WTD) models. Despite the differences in names, the physics behind RLO models and DC heating is very similar. In DC heating, the intermittent property is important; in RLO models, on the other hand, the solar wind is heated by continuous reconnections of small-scale magnetic elements. If we consider the small-scale magnetic reconnections as nanoflares then the DC heating and RLO models share the same physics: the heating comes from magnetic reconnection. AC heating and WTD models also share the same physics: waves are the responsible heating source. It is possible that the major heating mechanism in coronal loops differs from the one in solar wind. A large fraction of solar wind models favor Alfvén wave heating; however *Cranmer et al.* (2007) pointed out closed loops in the low corona are heated by nanoflares driven by the continual stressing of their magnetic footpoints.

1.2.1 Solar Wind

The solar wind is a stream of plasma flow ejected from the solar corona and extends to very large heliocentric distance (probably ends at the termination shock). The first solar wind model was developed by *Parker* (1958) by considering the coronal expansion, which means the corona is not in hydrostatic equilibrium. We follow the derivation in *Gombosi* (1998). The governing equations for the corona are as follows when considering single-fluid, fully ionized plasma and neglecting the magnetic field and heat conduction:

$$\frac{1}{r^2}\frac{d}{dr}(r^2\rho u) = 0 \tag{1.2}$$

$$\rho u\frac{du}{dr} + \frac{dp}{dr} + \rho G\frac{M_\odot}{r^2} = 0 \tag{1.3}$$

where ρ, u, p, G and $M_\odot$ represent the mass density, radial velocity, pressure, gravitation constant and solar mass, respectively. The solution for an isothermal solar corona is then obtained by solving the equation set. The solution is then given by

$$\frac{1}{2}u^2 - a_s^2 \ln u = 2a_s^2 \ln r + g_\odot \frac{R_\odot^2}{r} + C \tag{1.4}$$

where $a_s^2 = \gamma \frac{p}{\rho}$ is the sound speed for the isothermal corona, $g_\odot$ is the surface gravitational acceleration of the Sun, and $R_\odot$ is the solar radius.

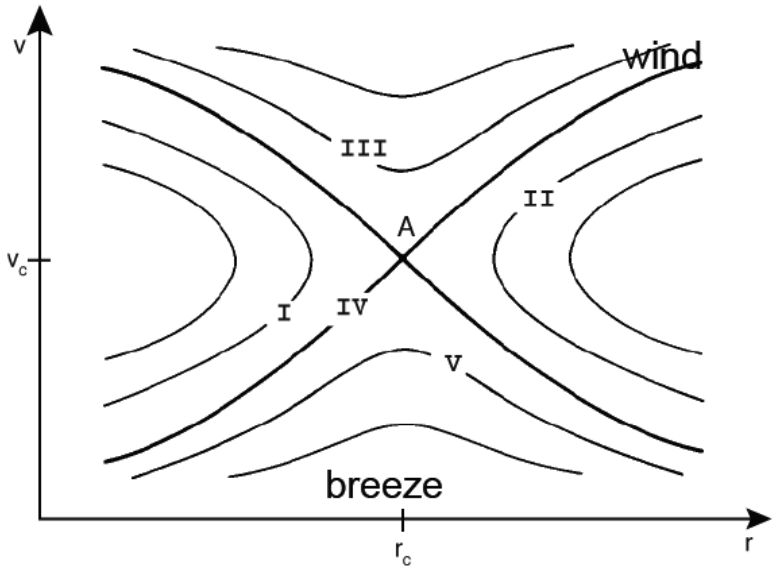

Figure 1.6: Mathematically admissible classes of isothermal solutions of an expanding corona. (reproduced from *Gombosi* (1998)).

Figure 1.6 plots all possible mathematical solutions of an expanding corona. The solution IV was favored by Parker, which starts subsonically at the base of the corona and accelerates to supersonic speed. Parker's solar wind model was confirmed several years later by *Neugebauer and Snyder* (1966). Even though Parker's solar wind model is considered the first solar wind model, some physical details are missing in the model. For example, the heating source that maintains the isothermal corona is absent. Scientists soon realized that the physical process that accelerates the solar

wind and heats the corona might be the same. As mentioned above, two groups of models have been developed to address different physical processes in the solar wind acceleration and the coronal heating problem: RLO models and WTD models.

In RLO models, small-scale reconnections of small-scale magnetic elements provide the energy to heat the corona and accelerate the solar wind (*Fisk et al.*, 1999; *Fisk*, 2003; *Schwadron and McComas*, 2003; *Fisk and Zhao*, 2009). Observational support for RLO models includes flux emergence, fragmentation, merging, and cancellation in the quiet photospheric network (*Schrijver et al.*, 1997; *Schrijver and Title*, 2003). *Fisk et al.* (1999) developed a solar wind model based on reconnections between small magnetic loops which emerge within supergranules in the solar photosphere and their surrounding magnetic field lines. Their model can successfully produce the fast solar wind the coronal temperature. *Feldman et al.* (2005) studied the morphological features in the solar corona as well as their physical properties and found that the emergence of new magnetic flux can accelerate the solar wind. *Tu et al.* (2005) studied the Doppler-velocity and radiance maps of spectral lines in a coronal hole and they found the solar wind starts flowing out of the corona at heights above the photosphere between 5 megameters and 20 megameters. They proposed that the solar wind comes from the reconnection between magnetic loops and open field lines.

WTD models, on the other hand, are much more popular in solar wind study, possibly due to relatively easy implementations in numerical simulations. Observations of Alfvén waves in the chromosphere, transition region, and the corona suggest that Alfvén waves contain enough energy to heat the corona and power the solar wind. (*De Pontieu et al.*, 2007; *McIntosh et al.*, 2011). In WTD models, it is assumed that convection motions in the solar interior will drive fluctuations that propagate up into the corona and those fluctuations generate MHD waves (usually Alfvén waves) there. The reflections of these waves will develop strong MHD turbulence which can dissipate the energy to heat the corona and accelerate the solar wind (*Coleman*, 1968;

Hollweg, 1986; *Isenberg*, 1990; *Li et al.*, 1999; *Matthaeus et al.*, 1999; *Dmitruk et al.*, 2001; *Suzuki*, 2006; *Verdini and Velli*, 2007; *Chandran et al.*, 2009). *Cranmer et al.* (2007) developed the first 1-D model that can provide a self-consistent solar wind solution starting from the photosphere and include shock heating, Alfvén wave heating and solar wind acceleration. Their model can produce a realistic range of fast and slow solar wind results by varying only the coronal magnetic field. *Chandran et al.* (2011) developed a 1-D solar wind model that includes separate energy equations for the electrons and protons, proton temperature anisotropy, collisional and collisionless heat flux, and an analytical treatment of low-frequency, reflection-driven, Alfvén wave turbulence. Their model results are consistent with various observations, such as the proton density observed by Ulysses, the velocity profile observed by Helios and electron temperature observed in a coronal hole. One of the most advanced 3-D global solar wind model is developed by *van der Holst et al.* (2014). Their model includes three temperatures (isotropic electron temperature, parallel and perpendicular ion temperatures) and incorporates Alfvén waves as the heating source. They showed that by choosing correct boundary conditions, their model can capture the coronal features observed in EUV images of Carrington Rotation (CR) 2107 provided by EUVI/STEREO and AIA/SDO.

1.2.2 Coronal Loops

Active region loops have received most of the attention in coronal loop studies. Figure 1.7 shows an example of active region loops. In this figure, fine structures related to active loops can be distinguished from the background corona. The loop geometry (like the loop length, cross section, etc) can be obtained from images (see *Aschwanden* (2004) for a detailed discussion). Different coronal loop models are developed to match the simulated differential emission measure along the loop to the observed values (*Rosner et al.*, 1978; *Aschwanden and Schrijver*, 2002; *Cheng*

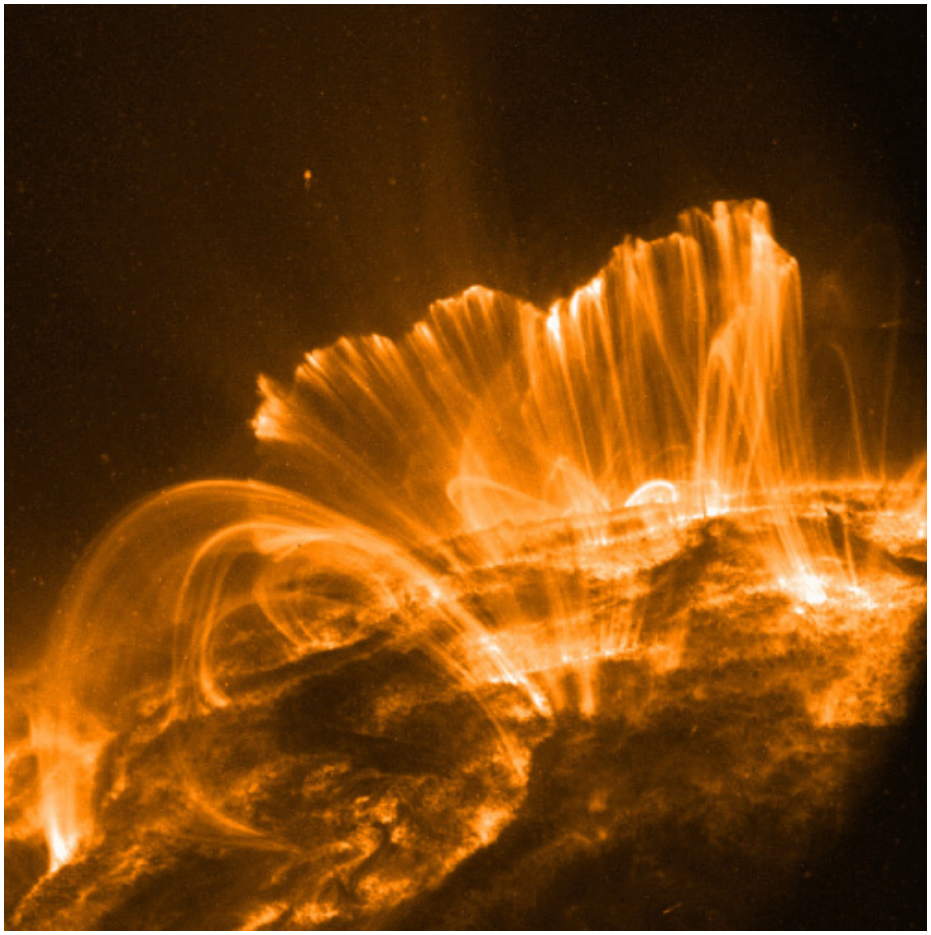

Figure 1.7: Active region loops observed by TRACE (taken from *Reale* (2010)).

et al., 1983; *Reale*, 2010; *Cargill et al.*, 2012). One of the major imperfections in these comparisons is the line-of-sight effect inherent in 2-D images (*Aschwanden*, 2004); however, *Aschwanden et al.* (2008) developed a triangulation technique to reconstruct 3-D coronal loops based on EUVI telescopes onboard STEREO A and B.

One of the very first loop models is the RTV model developed by *Rosner et al.* (1978). Their model considered the coronal loop in hydrostatic equilibrium. They used an ad-hoc uniform heating function in the model. This produced an important scaling law: $T_{max} = 1.4 \times 10^3 (pL)^3$, where T_{max} is the maximum temperature of the loop, p is the pressure, and L is the loop half-length. The magnetic field is 'neglected' in this model — it only provides the geometry of the loop and does not involve the physical processes in the loop. They assume the pressure is constant along the loop.

Thus if the temperature decreases with height, the density increases with height, which leads to a heavier fluid on top of a light fluid and causes Rayleigh-Taylor instability. The temperature in the RTV model will then always increase with height.

Other hydrostatic loop models are also presented in the literature (*Craig et al.*, 1978; *Serio et al.*, 1981; *Aschwanden and Schrijver*, 2002). These models improve the RTV model by considering non-uniformity in pressure and adding more flexibility to the ad-hoc heating functions. *Serio et al.* (1981) considered loops with non-uniform pressure. When they increased the heating near the footpoints, they found a different class of loops, which they named it class II loop, with a local temperature minimum at the apex. Furthermore, they found that if the heating scale height is smaller than 1/3 of the loop half-length, the density near the apex is higher than the density below. This, again, is the picture of the Rayleigh-Taylor instability, the loop becomes unstable and might correspond to prominence solutions. *Aschwanden and Schrijver* (2002) developed analytical approximations to hydrostatic solutions of coronal loops. They expressed the loop temperature, density, and pressure profile in terms of three independent parameters: the loop half-length, the heating scale length, and either the loop-top temperature or the base heating rate. They also found loops with temperature profiles similar to the class II loop in *Serio et al.* (1981).

Porter and Klimchuk (1995) studied lifetimes of 47 coronal loops from Yohkoh and showed that they were much longer than their computed cooling times. This suggested that the loops were in a state of quasi-static equilibrium. *Kano and Tsuneta* (1995) also studied scaling laws of coronal loops observed with Yohkoh and concluded that the results are consistent with the scaling law predicted by the RTV model when considering measurement uncertainties in temperature and the loop length.

The simple scaling laws from hydrostatic loop models can be easily applied in different applications (*Schrijver et al.*, 2004; *Gontikakis et al.*, 2008). *Gontikakis et al.* (2008) used a simple tool with scaling laws to study coronal heating in a solar active

region. They obtained scaling laws that relate both the mean volumetric heating to the loop length, and the heating flux through the loop footpoints to the magnetic field strength at the footpoints. They found that coronal heating is stronger close to the footpoints of the loops as well as asymmetric along them. They attributed the observed small coronal-loop width expansion to both the preferential heating of coronal loops of small cross-section variation, and the cross-section confinement due to the random electric currents flowing along the loops.

Hydrostatic loop models are simple and powerful; however, they have a major limitation: loops are in quasi-equilibrium state. Some loops are not in quasi-equilibrium, for example, flares. *Craig and McClymont* (1976) considered fluid motions in their flare model and showed that the mass motions may be inferred in soft X-ray differential emission measure. *Nagai* (1980) considered loops not in quasi-equilibrium states and developed a hydrodynamic loop model then applied it in solar flare study. He showed that the coupling between the corona and the chromosphere is important and thermal conduction plays a significant role in solar flares. *Cheng et al.* (1983) simulated the dynamic response of a coronal loop to a large energy input. They found the most important dynamic responses are chromospheric ablation of heated plasma and the formation of compressed cool plasma. *Fisher et al.* (1985a,b,c) used their hydrodynamic loop model to study the plasma response, the chromospheric evaporation and the dynamics of the chromosphere due to short bursts of energetic nonthermal electron heating, respectively. They found that those bursts of heating are a potential candidate for explaining the coronal heating.

One of the major topics in hydrodynamic loop models is the temperature response due to different heating. *Cargill* (1994) presented observational consequences of a nanoflare heated corona by adopting an analytic formalism for the cooling of impulsively heated loops. He predicted a steep scaling as $T^{4.5}$ in the emission measure for $T > 10^6$K plasma. *Klimchuk et al.* (2008) developed a highly efficient model called

Enthalpy-Based Thermal Evolution of Loops (EBTEL). EBTEL is a 0-D code that can describe the evolution of the average temperature, pressure, and density along a coronal strand. They showed that their code can correctly capture the plasma responses as other 1-D hydrodynamic loop models and it is much more efficient. *Cargill et al.* (2012) improved the EBTEL by including gravitational stratification and a physically motivated approach to radiative cooling, which leads to a better tracking of density in the simulation. They showed that the improved EBTEL can provide quick-look results of loop evolution in response to a given heating function. They proposed that the new EBTEL code can test whether nanoflare heating exists in active regions if searching a large range of parameter space. Explicit analytical approximations for the hydrodynamic evolution of the electron temperature and electron density in 1-D coronal loops are derived by *Aschwanden and Tsiklauri* (2009). They showed that the analytical expressions can be used to efficiently model the hydrodynamic evolution of coronal loops (and flare loops) and test whether the nanoflare heating is the heating mechanism for the solar corona.

Siphon flows, which are driven by pressure imbalance between the loop footpoints, are another important topic in coronal loop studies. *Cargill and Priest* (1980) discussed the effects of subsonic and shocked flows in symmetric or asymmetric coronal loops. *Noci* (1981) showed several different types of steady flows: always subsonic; subsonic in one branch of the loop, supersonic in the second; subsonic-supersonic with stationary shocks which adjust the flow to the boundary conditions in the second footpoint. He suggested the subsonic-supersonic flows can cause the intensity drop which is observed in some UV loops. *Thomas* (1988) developed a steady siphon flow model in isolated, thin magnetic flux tubes surrounded by field-free gas with plasma beta larger than unity. He applied the model to study siphon flows in the solar photosphere and interpreted that the Evershed flow, which is in the penumbral photosphere of a sunspot, is a possible siphon flow along isolated magnetic flux tubes. *Orlando et al.*

(1995a) applied a hydrodynamic model developed by *Orlando et al.* (1995b) to study stationary siphon flows in a semicircular solar coronal loop and showed that shock position depends on the volumetric heating rate of a loop.

It is important to point out that nearly all coronal loop models only compare their simulation results with active region loops. It is difficult to study quiet Sun loops because they look "fuzzy" in the image, which can be seen in Figure 1.7. As the magnetic field is everywhere in the corona, it is impossible that there are no other loops except the very distinct active loops in the image. Scientists sometimes call the corona outside the active regions the diffuse background, which sounds unimportant. However, there are many more loops filling the diffuse corona, and those loops are QS loops which are rarely studied. One cannot skip studying these loops in the coronal heating problem because the diffuse corona overlies most of the Sun's surface (especially at solar minimum). We discuss our current knowledge of the quiet Sun corona in the next section.

1.3 Current Observations of the Quiet Sun Corona

Quiet Sun, defined as closed magnetic field regions excluding active regions (*Aschwanden*, 2004), looks stable and shows only little dynamics in large scale over a long period of time. Figure 1.8 shows an example of a QS region. It can be readily seen that the QS looks very different from the active region shown in Figure 1.7: it looks "fuzzy". This makes investigating quiet Sun difficult. Quiescent streamers and quiescent filaments are two important structures in QS regions. We review some of the important observational aspects of these two structures in this section.

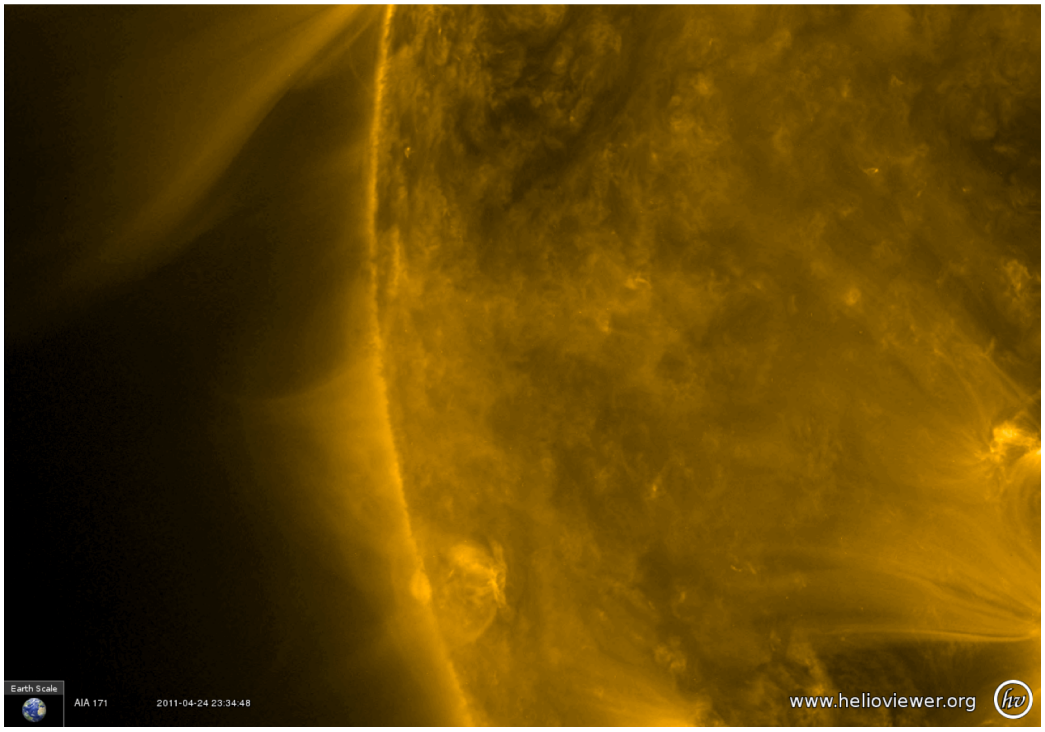

Figure 1.8: A quiet Sun region observed by AIA/SDO at the wavelength of 171 Å. (from `http://www.helioviewer.org/`)

1.3.1 Streamer

Streamers are loop-like structures associated with closed magnetic field lines. There are three kinds of streamers: helmet streamers, found over an active region; quiescent streamers, found in quiet Sun region; and unipolar streamers (pseudostreamers), that separate open field lines of the same polarity. Helmet streamers and quiescent streamers separate open field lines of different polarities. Helmet streamers and quiescent streamers have been studied for a long time (*Sturrock and Smith*, 1968; *Hundhausen*, 1972; *Borrini et al.*, 1981; *Feldman et al.*, 1999; *Koutchmy and Livshits*, 1992; *Koutchmy et al.*, 1994; *Wang et al.*, 1997; *Warren and Warshall*, 2002; *Ofman et al.*, 2011). Pseudostreamers became a hot topic recently (*Wang et al.*, 2012; *Zhao et al.*, 2013) after *Wang et al.* (2007) revisited the pseudostreamer observed during the solar eclipse of March 29 2006 and realized its importance in solar wind studies. *Wang et al.* (2007) proposed that pseudostreamers are a source for fast solar wind.

Helmet streamers and pseudostreamers are associated with complex magnetic geometry (*Low*, 1996; *Wang et al.*, 2012; *Zhao et al.*, 2013), indicating they have strong dynamics. As we are interested in quiet Sun structures in this dissertation, we limit our discussions to quiescent streamers.

A quiescent streamer can be separated into three components: a streamer core; streamer legs (edges of the streamer); and a streamer cusp just above the uppermost closed field line of the streamer, where the streamer legs begin to narrow into a stalk. (*Steinolfson et al.*, 1982; *Ofman*, 2000; *Akinari*, 2007). Figure 1.9 shows an empirical configuration of a quiescent streamer in a sketch, showing the streamer core, streamer leg, and the cusp location. We discuss plasma density, temperature, and element abundance in quiescent streamers in the following paragraphs.

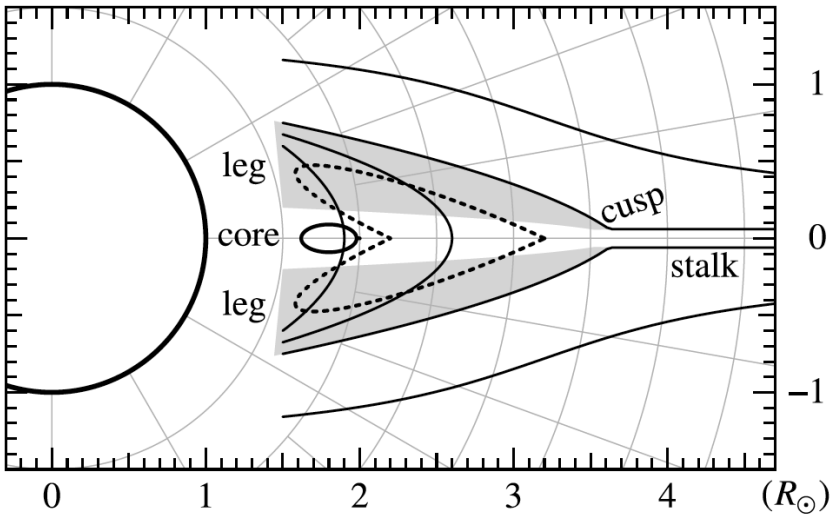

Figure 1.9: An empirical configuration of a quiescent streamer. (from *Akinari* (2007))

The density in quiescent streamers is greater than in coronal hole regions (*Koutchmy and Livshits*, 1992). One method that can be applied to determine the density is direct inversion of line-of-sight electron column density from white-light coronagraph images (*van de Hulst*, 1950). The electron density can then be obtained by assuming some special streamer geometries, for example, axial symmetry (*Koutchmy*, 1988;

Koutchmy and Livshits, 1992; *Guhathakurta and Fisher*, 1995). Another approach involves spectral line analysis (*Feldman et al.*, 1999; *Li et al.*, 1998a; *Gibson et al.*, 1999; *Feldman and Landi*, 2008). *Landi et al.* (2006) derived the electron density of a streamer region to be around $10^8 \mathrm{cm}^{-3}$ at 1.10 $R_\odot$ by using the spectra data from the Solar Ultraviolet Measurements of Emitted Radiation (SUMER) on SOHO. Tomography techniques can determine the 3-D electron density in the quiet Sun corona (*Frazin et al.*, 2009; *Barbey et al.*, 2011). *Vásquez et al.* (2010) obtained the 3-D electron density from $1.03R_\odot$ to $1.2R_\odot$ for Carrington Rotation (CR) 2077 and found their results are of order 0.8 smaller than the value obtained by *Landi et al.* (2006) at the same height. They explained that the difference comes from the boundary and the core of a more complex streamer structure.

The temperature in quiescent streamers is higher than coronal hole regions (*Koutchmy and Livshits*, 1992). The temperature can be determined from spectral line analysis (*Feldman et al.*, 1999; *Li et al.*, 1998a; *Gibson et al.*, 1999; *Feldman and Landi*, 2008). *Parenti et al.* (2000) used Coronal Diagnostic Spectrometer (CDS) and (UltraViolet Coronograph Spectrometer (UVCS) onbard SOHO and found that temperature in quiescent streamers increases with height below 1.2 $R_\odot$. *Feldman and Landi* (2008) argued an isothermal solar corona exists in quiescent streamer regions. *Vásquez et al.* (2011) derived 3-D electron temperature between $1.03R_\odot$ and $1.20R_\odot$ using Differential Emission Measure Tomography (DEMT) technique (*Frazin et al.*, 2009) for CR-2068. They found their electron temperature is consistent with temperature determined from spectral line analysis. They also confirmed that the QS corona is in hydrostatic equilibrium state. Recently, *Landi and Testa* (2014) studied 60 quiescent streamers during solar cycle 23 and 24 (from 1996 to 2013), which were observed by SUMER/SOHO and EIS/Hinode; they showed that the temperature in coronal streamers does not have significant variations in different solar cycles.

Element abundance is an important topic closely related to solar wind study and

can reveal the origins of fast and slow solar wind (*Feldman et al.*, 2005; *He et al.*, 2010). Early studies show a correlation between the element abundance in quiescent streamers and that in slow solar wind, which indicates the slow solar wind comes from quiescent streamers (*Raymond et al.*, 1997; *Noci et al.*, 1997). *Feldman et al.* (1998) studied first ionization potential (FIP) elements in streamers and in north pole regions; they found low FIP elements are enriched by about a factor of 4 in the streamer with little enrichment in the north polar coronal hole. Their results agreed well with the Ulysses in situ observations in both fast and slow solar wind and supported the idea that fast wind comes from coronal hole and slow wind from streamers. *Feldman et al.* (2005) used SUMER/SOHO data to investigate plasma density, temperature and element abundances and confirmed that the slow solar wind comes from quiescent streamer regions.

1.3.2 Filaments and Prominences

Filaments and prominences are essentially the same structures; they are commonly seen in the solar atmosphere. The difference between how these structures are named depends on the location at which they are seen. Filaments are observed as dark threads in chromospheric Hα images on the solar disk; they are called prominences when observed at the solar limb (*Parenti*, 2014). Filaments have been observed for a long time (*Tandberg-Hanssen*, 1974, 1998). Figure 1.10 shows three dark filaments observed by He II 304 Å from EIT/SOHO. Prominences are denser (with electron density $10^9 \sim 10^{11}\mathrm{cm}^{-3}$) and cooler (with temperature less than 10^4K) than surrounding coronal material (about 100 times denser and cooler) (*Hirayama*, 1986; *Labrosse et al.*, 2010). Prominences can be classified into two groups based on their lifetimes: quiescent and active (*Tandberg-Hanssen*, 1995; *Mackay et al.*, 2010). Quiescent prominences are relatively stable structures that live for a long time (from several days to several months). They are mostly found outside active regions. Ac-

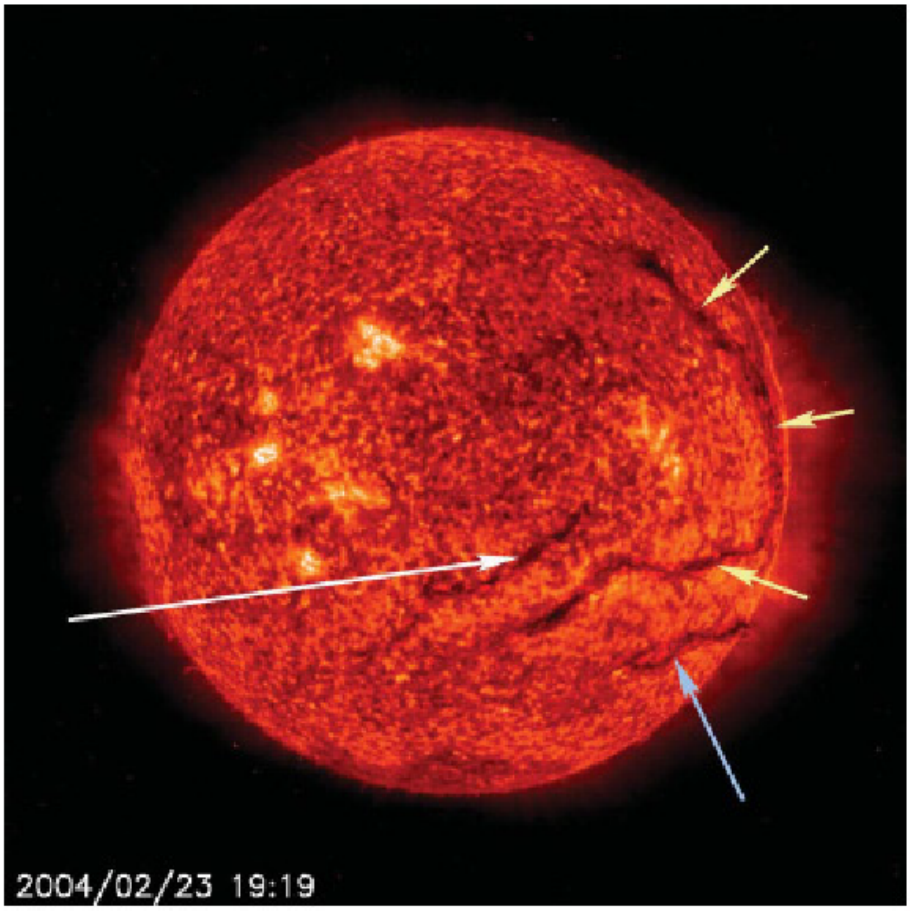

Figure 1.10: Three dark filaments observed by He II 304 Å from EIT/SOHO. (from *Parenti* (2014))

tive prominences are dynamic features typically seen in active regions. The lifetime of active prominences is shorter than that of the associated active region (*Labrosse et al.*, 2010). *Gilbert et al.* (2000) showed a strong relationship between active prominences and Coronal Mass Ejections (CMEs) (also reviewed by *van Driel-Gesztelyi and Culhane* (2009)). Again, as we are interested in QS structures, only quiescent prominences are discussed in this section. More specifically, we discuss plasma density and temperature; while dynamic process and fine structures are reported in prominence core (*Engvold*, 1976; *Lin et al.*, 2005; *Chae*, 2007, 2010; *Oliver*, 2009) and Prominence-Corona-Transition-Region (PCTR) (*Parenti and Vial*, 2007; *Vial et al.*, 2012; *Cirtain et al.*, 2013; *Alexander et al.*, 2013).

As reviewed by *Labrosse et al.* (2010) and *Parenti* (2014), plasma diagnostics techniques are generally applied to determine electron density, temperature, and ionization degree. We discuss three structures of quiescent prominences: prominence core, PCTR and coronal cavity here. The prominence core is observed by hydrogen and helium spectral lines as the core is made of cool plasma; while the PCTR is mainly studied by transition-region spectral lines because the PCTR is hotter. The coronal cavity is investigated with a combination of white-light, EUV and soft X-ray images (*Fuller and Gibson*, 2009).

The prominence core is made of cool and dense material. The radiation processes there are considered to be very complex and require a solution of the non local thermodynamic equilibrium radiative transfer problem (*Labrosse et al.*, 2010). The electron density in the prominence core can be measured by several different methods, including the Stark effect (*Hirayama*, 1971; *Zirker*, 1985), the Hanle effect (*Bommier et al.*, 1986, 1994), ratios between different spectral lines (*Landman*, 1986), emission measure (*Bastian et al.*, 1993; *Li et al.*, 1998b) and more. *Labrosse et al.* (2010) provided the range of electron density as 10^9 to $10^{11}\mathrm{cm}^{-3}$ based on various models. The electron temperature can be obtained from spectroscopy techniques (*Noyes et al.*, 1972; *Ofman et al.*, 1998). In the Hvar reference atmosphere provided by *Engvold et al.* (1990), the electron temperature is between 4300 to 8500K. Ionization degree and abundances are difficult to measure due to partially-ionized environment and uncertainties in the absolute UV line photometry along with uncertainties in atomic parameters (*Labrosse et al.*, 2010). The Hvar reference atmosphere estimates the value of $N(\mathrm{H}^+)/N(\mathrm{H}^0)$ between 0.2 and 0.9. Element abundances for C, N, O and Si were obtained by *Mariska* (1980) and helium abundance was derived by *Del Zanna et al.* (2004).

The Prominence-Corona-Transition-Region (PCTR) consists of optically thin plasma; so we can apply plasma diagnostic techniques to EUV and UV emissions lines to study

plasma properties in PCTR (*Labrosse et al.*, 2010). The electron density can be determined by line ratios of EUV observations (*Orrall and Schmahl*, 1976; *Mariska et al.*, 1979; *Widing et al.*, 1986; *Kucera and Landi*, 2006) or emission measures (*Chae*, 2003). *Labrosse et al.* (2010) summarized the values to be in the range of $10^9 \sim 10^{11}\mathrm{cm}^{-3}$ with a few exceptions. The electron temperature can be derived by Differential Emission Measure (DEM) (*Wiik et al.*, 1993; *Kucera and Landi*, 2006; *Parenti and Vial*, 2007). *Parenti and Vial* (2007) obtained the DEM for a quiescent prominence and a quiet Sun corona region and concluded that the temperature for the quiescent prominence is at around $\log T(\mathrm{K}) = 5.1$, which is smaller than that in the quiet Sun region.

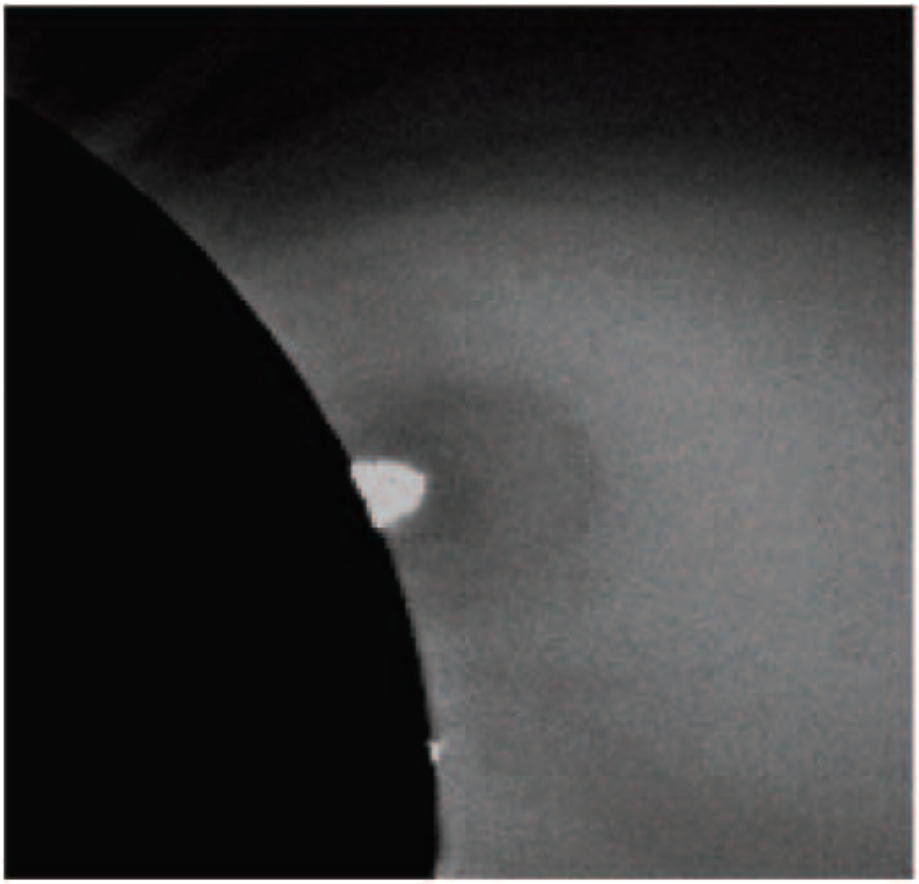

Figure 1.11: A quiescent prominence with cavity observed on March 18 1988 from the National Center for Atmospheric Research/High Altitude Observatory Newkirk White-Light Coronal Camera. (from *Gibson et al.* (2006))

Coronal cavities are observed as dark regions in the white-light, EUV and soft X-ray images. They are around prominence (see Figure 1.11 for an example) and sometimes are associated with CME (*St. Cyr and Webb*, 1991; *Gibson et al.*, 2006, 2010). White-light coronagraph data can be used to calculate the density in coronal cavity. Due to the weak EUV and soft X-ray emissions in coronal cavities, white-light coronagraph data are generally used to measure the density and temperature (*Guhathakurta et al.*, 1992; *Fuller et al.*, 2008); though some attempts have been made by using EUV spectroscopy (*Kucera et al.*, 2012). *Fuller et al.* (2008) used white-light coronagraph images to derive the electron density in a coronal cavities and found that cavity density is depleted by a maximum of 40% with respect to the surrounding helmet streamer at low altitudes (up to 1.18 $R_{\odot}$). But the density in the cavity is consistently higher than that in coronal holes. They assumed a hydrostatic equilibrium model in coronal cavity and then obtained the hydrostatic density scale height to infer the temperature. They concluded that the hydrostatic temperature in the cavity is higher than the surrounding streamer material. *Vásquez et al.* (2009) used a new technique called Differential Emission Measure Tomography (DEMT), which allows determination of the 3-D electron density and temperature in the coronal, to study coronal cavity. They confirmed the conclusions that cavities have lower density and higher temperature than the neighboring material.

The lifetime of quiescent prominences is between several days to a few months. *Bernasconi et al.* (2005) developed an automated detection technique to statistically study filament properties. They analyzed five years of Big Bear Solar Observatory (BBSO) Hα filtergrams and detected 19211 filaments. They found that the lifetime of filaments is within several days. A filament ends its life in of of the two directions: one direction is to go to the same thermal conditions as the surrounding corona material through various heating processes (*Parenti*, 2014); the other direction is filament eruption trigger by a thermal or dynamical instability (*Mackay et al.*, 2010). In the

next section, we review some of the basic instability mechanisms in the solar corona.

1.4 Stability of the Sun's Atmosphere

In this section, we only discuss three kinds of instabilities in the solar corona: Rayleigh-Taylor instability, hydrostatic instability and radiatively-driven instability. More discussions of various instabilities mechanisms, like Kelvin-Helmholtz instability, can be found in *Aschwanden* (2004).

1.4.1 Rayleigh-Taylor Instability

Rayleigh-Taylor instability, which was first proposed by *Taylor* (1950), is an instability of an interface between two stratified fluids of different densities; more specifically, the instability develops when the heavier fluid is on top of the lighter fluid.

The magnetic field exists everywhere in the solar corona, meaning that we must consider magneto Rayleigh-Taylor instability. Derivations of magneto Rayleigh-Taylor instability require more sophisticated approach and are carried in various magnetic configurations (*Kruskal and Schwarzschild*, 1954; *Harris*, 1962; *Chandrasekhar*, 1961; *Sinars et al.*, 2010; *Lau et al.*, 2011). Generally speaking, the magnetic field present in the solar corona can provide extra support for the heavier fluid on top of the lighter fluid; so the two fluid configuration with magnetic field support is more stable than those without magnetic field support. *Kruskal and Schwarzschild* (1954) studied a plasma supported by the pressure of a horizontal magnetic field against gravity. They found that along the horizontal direction, the magnetic curvature force can restore the small perturbations to its initial position, thus the plasma is stable against perturbations in the horizontal direction. In the perpendicular direction, no restoring forces are found to stabilize the system. So the plasma is unstable against perturbations in the perpendicular direction. *Lau et al.* (2011) studied magneto Rayleigh-Taylor instability of a finite slab using ideal MHD model. They found that if there are mag-

netic field on both sides of the slab, the feedthrough of the magneto Rayleigh-Taylor instability may be significantly reduced, which means the magnetic field can stabilize the system to some extent.

1.4.2 Hydrostatic Instability

The hydrostatic instability, which is also called convective thermal instability (*Aschwanden*, 2004), is driven by vertical heat transfer and mass exchange. A detail derivation of the instability can be found in *Gombosi* (1998). The stable condition is given as

$$\frac{dT}{dz} > -\frac{\gamma - 1}{\gamma}\frac{\bar{m}}{k}g = -\frac{g}{C_p} = \Gamma_{ad} \tag{1.5}$$

where γ is the adiabatic index, $\bar{m}$ is the mean molecular mass, k is the Boltzmann constant, g is the local gravitation acceleration, C_p is the specific heat at constant pressure, Γ_{ad} is the adiabatic lapse rate.

The stable condition for hydrostatic equilibrium means that if the temperature gradient is larger than the adiabatic lapse rate, the fluid parcel will return to its original position after a small displacement; the atmosphere is unstable if the temperature gradient is less than the adiabatic lapse rate: larger scale vertical motions will develop when a small perturbation is imposed.

The hydrostatic instability is not extensively studied in the solar corona. *Aschwanden* (2004) pointed out that plasma flows along magnetic field lines can wipe out small unstable temperature gradient so the coronal loop can be more stable that the static atmosphere.

1.4.3 Radiative-Driven Instability

Radiative-driven instability is an important topic in solar physics. The physics behind this instability is the dependence of the radiative function on plasma density

and temperature (the radiative loss function can be found in CHIANTI database (*Landi et al.*, 2012, 2013)). When the plasma starts to cool, it will reach higher density; the cooling then increases with higher density. The plasma develops the radiative-driven instability from this positive feedback. *Field* (1965) showed that the plasma under thermal equilibrium is unstable and can result in the formation of condensations of higher density and lower temperature than the surrounding medium under a wide range of conditions. We will discuss the radiative-driven instability in more detail in chapter III.

1.5 Differential Emission Measure Tomography

Differential Emission Measure Tomography (DEMT) is applied throughout the whole dissertation. We summarize the processes in this section. A detailed discussion can be found in *Frazin et al.* (2009).

In a first step, a time series of EUV images spanning a full solar synodic rotation is used to perform a *solar rotational tomography* (SRT) for each band of the EUV telescope separately[1]. The product of the tomographic inversion in each band is the 3D distribution of the *filter band emissivity* (FBE), defined as the wavelength integral of the coronal EUV spectral emissivity and the telescope's passband function of each band.

In a second step, the FBE values obtained for all bands in each tomographic cell (or voxel) are used to constrain the determination of a *local differential emission measure* (LDEM) distribution. [2] The LDEM distribution $\xi(T)$, a function of temperature, is similar to the standard DEM, but it describes exclusively the plasma contained in the

[1]SRT is cast as a global optimization problem. The objective function is a sum of the quadratic norm of the difference between real and synthesized images, and a *regularization* (smoothing) term controlled by a single *regularization parameter* p. The regularization level is determined through cross-validation of the resulting model with complementary images not used for the SRT *Frazin et al.* (2009); *Vásquez et al.* (2010)

[2]The emission physics was taken from CHIANTI Version 6.0.1 (*Dere et al.*, 1997, 2009).

respective tomographic voxel, greatly mitigating the LOS ambiguity that is intrinsic to standard DEM analysis. In exchange, the LDEM lacks the temporal resolution of the standard DEM, as it is based on time series of images spanning a full solar rotation. The LDEM analysis is then reliable for coronal regions that exhibit stability during their transit on the solar disk. For such regions, the LDEM is a measure of the thermal distribution of the plasma. Its 0th and 1st moments are the mean squared electron density ($\langle N_e^2 \rangle$) and electron mean temperature (T_m), where the average is taken over the LDEM distribution:

$$\left\langle N_e^2 \right\rangle \equiv \int dT\, \xi(T) \tag{1.6}$$

$$T_m \equiv \frac{1}{\left\langle N_e^2 \right\rangle} \int dT\, \xi(T)\, T \tag{1.7}$$

The tomographic grid covers the height range 1.00 to $1.25 R_\odot$, beyond which the signal is too weak to make the reconstruction, with a radial resolution of 0.01 $R_\odot$, and an angular one of $2^\circ \times 2^\circ$. Due to optical depth issues at the base of the tomographic grid, EUV signal-to-noise levels, and scattered light effects (*Shearer et al.*, 2012), the DEMT results are generally reliable in the height range from 1.03 to 1.20 $R_\odot$. *Vásquez et al.* (2010) and *Vásquez et al.* (2012) showed that DEMT results (electron density and temperature) are consistent with spectral line observations in quiescent coronal structures, which supports that the quiet Sun coronal can be described by DEMT very well.

1.6 Thesis Overview

In Chapter II, we will develop a novel technique called Michigan Loop Diagnostic Technique (MLDT) to investigate temperature profiles along QS coronal loops. MLDT combines Differential Emission Measure Tomography (DEMT) and a potential field source surface (PFSS) model, and consists of tracing PFSS field lines through the tomographic grid on which the Local Differential Emission Measure (LDEM) is determined. As a result, the electron temperature T_e and density N_e at each point along each individual field line can be obtained. The application of MLDT to Carrington Rotation (CR) 2077, which is at solar minimum, shows a new class of loops in the quiet Sun corona: the inverted temperature loops, in which the temperature decreases, so called "down" loops. We named the regular loop in which the temperature increases with height "up" loops. We will discuss the "up" and "down" loop spatial distribution and their implications in coronal heating.

Chapter III will discuss the thermal stability of "down" loops as the "down" loops have received arguments that they cannot exist in the solar corona due to thermal instability. We will use one of the most sophisticated solar corona models, the Alfvén Wave Solar Model (AWSoM), to explore the stability of "down" loops. AWSoM is a magnetogram-driven 3D, global model with an inner boundary in the upper chromosphere. The AWSoM's corona is heated by Alfvén waves via prescriptions for turbulent damping of both unidirectional and counter-propagating waves. We first generate "down" loops with AWSoM and then perturb the "down" loops by decreasing the temperature at the apex to test the stability of "down" loops.

Chapter IV studies the evolution of "down" loops in the last solar cycle. In chapter II, we only study one solar rotation, it will be very interesting to see whether "down" loops exist in other solar rotations and their evolution in a solar cycle. So in this chapter, we will extend the analysis to 11 CRs around the last solar minimum. We will discuss more properties of "down" loops in terms of sunspot number and plasma

beta. We will further discuss the implication of "down" loops in coronal heating.

Conclusions and possible future work are presented in Chapter V.

Chapter II and chapter IV are based upon published work *Huang et al.* (2012) and *Nuevo et al.* (2013) respectively. Chapter III is a manuscript which will be submitted to *the Astrophysical Journal*.

CHAPTER II

Newly Discovered Global Temperature Structures in the Quiet Sun at Solar Minimum

Magnetic loops are the building blocks of the magnetically closed solar corona. They host the plasma as well as the processes that heat it, and their interactions with open field lines may even generate the fast and slow solar wind (*Fisk et al.*, 1999; *Wang et al.*, 1998; *Feldman et al.*, 2005; *Antiochos et al.*, 2011). Despite their importance, they are not yet well understood; in particular, we do not know exactly which mechanisms heat the plasma, not even whether it is a steady heating (*Warren et al.*, 2010; *Winebarger et al.*, 2011; *Schrijver et al.*, 2004) or an impulsive, nanoflare heating (*Viall and Klimchuk*, 2011; *Patsourakos and Klimchuk*, 2005). Despite the fact the quiet Sun (QS) can cover the vast majority of the solar surface, especially near the cycle minimum, almost all of the work on coronal loops has only considered active region (AR) loops, and QS loops are a largely unexplored territory. We are not aware of any published studies of individual quiet Sun loops. This state of affairs is partially due to the fact that ARs are more likely to be hosts of dramatic events such as powerful flares and CMEs, and to the fact that it is very difficult if not impossible to observationally define a QS loop in an EUV [although one could argue that QS loops are seen in the processed white-light eclipse images of *Pasachoff et al.* (2011)], while they are readily identified in active regions [e.g., *Vaiana et al.* (1973); *Aschwanden*

and Boerner (2011)]. The difficulty in observing QS loops is perhaps related to the fact that loops become "fuzzy" when seen in high temperature lines (*Tripathi et al.*, 2009), which is explained by *Reale et al.* (2011) in terms of impulsively heated independent strands (which spend most of their time at coronal temperatures). The quiet Sun corona has mostly been studied by applying plasma diagnostic techniques to spatially averaged regions of the corona with no attempt to resolve individual loop structures. The quiet Sun analyses reviewed by *Feldman and Landi* (2008) (also see *Feldman et al.* (1999), *Warren* (1999) and *Landi et al.* (2002)) have shown a nearly isothermal solar corona with little time evolution, but this can be an artifact of time-averages of the observations. At larger heights (1.7 $R_\odot$), *Raymond et al.* (1997) used UVCS/SOHO (*Kohl et al.*, 1995) data for an abundance analysis of a solar minimum equatorial streamer and found that an isothermal plasma at 1.6 MK explains the observations, although the possibility of hotter and cooler plasma cannot be excluded. Most of the coronal loop models conclude that the temperature increases with height along a loop (*Rosner et al.*, 1978; *Porter and Klimchuk*, 1995; *Kano and Tsuneta*, 1995); though *Serio et al.* (1981) and *Aschwanden and Schrijver* (2002) showed that if the heating is enhanced near the footpoints of a loop, the temperature decreases with height in near the apex. Observations from *Parenti et al.* (2000) showed that the temperature in quiescent streamers increases with height below 1.2 $R_\odot$, which agree with coronal loop models; while no observations show that the temperature decreases with height.

In this chapter, we demonstrate a new method that allows identification of QS loops for the first time, and provide first results of some of their properties, including the first observational identification of loops in which the temperature decreases with height.

2.1 Data and MLDT Analysis

Here, we assume that QS loops are well described by potential fields between 1.03 and 1.20 $R_\odot$ and determine the 3D electron temperature T_e and density N_e in this height range using the Differential Emission Measure Tomography (DEMT) technique (*Frazin et al.*, 2005, 2009; *Barbey et al.*, 2011). In DEMT, solar rotation tomography (SRT) is applied to a time series of multi-band EUV images, such as those provided by EUVI (*Howard et al.*, 2008) or AIA (Lemen et al. 2012). If multiple spacecraft are used, this can be accomplished in less than a full synoptic rotation period. After the SRT has been performed, a standard differential emission measure (DEM) analysis technique is applied to produce the local differential emission measure (LDEM). The LDEM's (normalized) $0\underline{th}$ and $1\underline{st}$ moments are $< N_e^2 >$ and $T_m \equiv < T_e >$, where the brackets $< >$ denote the volume average over a cell in the tomographic grid. The Michigan Loop Diagnostic Technique (MLDT) takes a field line specified by a potential field source surface model (PFSSM) and follows it through the tomographic grid, assigning the DEMT values of $\sqrt{< N_e^2 >}$ and T_m to all of the points along the loop. We use the synoptic magnetogram provided by MDI/SOHO on the 3600×1080 longitude/latitude grid, binned to 360×180. As we only consider the field above 1.03 $R_\odot$, more resolution is not necessary. Our PFSSM model was developed by *Tóth et al.* (2011), and it uses a finite difference solver to calculate the magnetic field and provides a more accurate field in high latitude regions than are typically obtained with expansion methods. The MLDT was first applied to test the hypothesis of hydrostatic equilibrium in open and closed field structures for several regions in CR2068 (also near solar minimum) in *Vásquez et al.* (2011). There it was found that in open field regions, the ion temperature was higher than the electron temperature (T_m) or significant wave pressure gradients must exist, while the closed region data seemed to be much more consistent with isothermal (i.e., equal electron and ion temperatures) hydrostatic equilibrium.

Development of the MLDT makes us the first to identify individual quiet Sun loop bundles and measure their thermodynamic states, and it also allows statistical studies of their properties. The most important limitation of the MLDT is temporal resolution specified by the full solar rotation ($\sim$ 27.3 days) required to make the synoptic magnetogram for the PFSSM. DEMT has a similar limitation, but in this case the dual-spacecraft STEREO geometry allowed us to acquire the equivalent of a synoptic rotation in about 21 days. The QS is particularly well suited to using DEMT and the PSSFM because, while there are fluctuations on rapid time scales, QS regions show little secular evolution and they seem to be statistically stationary, so the time averages are meaningful approximation of their states. Furthermore, the results presented below are based on statistical analyses of hundreds of loops, and our conclusions are based on statistical trends, so that the particular dynamics of any single loop are not important. Also, it is likely that any sporadic currents in QS regions are on small spatial scales in the chromosphere or below and have a negligible influence on the large-scale field studied here, thus supporting the use of the PFSSM.

In this chapter, we apply the MLDT to CR2077, which corresponds to the period between UT 06:56 November 20 and UT 14:34 December 17, 2008, a time of extremely low solar activity as the sunspot minimum was achieved in the next Carrington rotation. CR2077 had only one short-lived active region (NOAA 11009, Dec. 11-13), so the Sun was very quiet and nearly ideal for our analysis. The region corresponding to the active region was excluded from this analysis.

During this period, the two STEREO spacecraft were separated by $84.5^\circ \pm 1.2^\circ$, which allowed for the reconstruction to be performed with data gathered in about 21 days (around 3/4 of a solar rotational time). The data consist of hour cadence EUVI images in the 171, 195 and 284 Å bands taken from UT 00:00 November 20 2008 to UT 06:00 December 11 2008, co-added to make one image every six hours that was processed by the SRT code. SRT is independently performed for the series

of images corresponding to each wavelength band resulting in the 3D distribution of the *filter band emissivity* (FBE) for each band. The FBE is an emissivity defined in Frazin et al. (2009), and it can be obtained by integrating the LDEM with the appropriate temperature weighting function. It plays a role that is analogous to the observed spectral line intensity in standard DEM analysis (*Craig and Brown*, 1976). While the DEM and intensity are line-of-sight integrated quantities, the LDEM and the FBE pertain only to the plasma located within a given voxel of the tomographic grid. The SRT technique does not account for the Suns temporal variations [although see *Butala et al.* (2010)], and rapid dynamics in the region of one voxel can cause artifacts in neighboring ones. Such artifacts include smearing and negative values of the reconstructed FBEs, or zero when the solution is constrained to positive values. These are called zero-density artifacts (ZDAs) and are similar to those described by *Frazin and Janzen* (2002) in white-light SRT. As is common, some of the ZDAs that appear in this reconstruction correspond to the location of the active region. For all voxels with no ZDAs, we use the inferred LDEM to forward-compute the three synthetic values of the FBE. We only use the voxels where the synthetic and measured values agree within 1%, which happens to be the vast majority of them.

The STEREO calibration has not been addressed in any publication since *Howard et al.* (2008), but (J.P. Wuelser, 2011, *private communication*):

1. The drift in instrumental sensitivity with time is negligible.

2. The relative calibration of the EUVI channels has an uncertainty of 15%. In Appendix A, we show that this uncertainty has little effect on our results.

3. The absolute calibration has an uncertainty of about 30%. This uncertainty has the potential to change the electron density estimates uniformly by $\sim 15\%$, and it does not affect the temperature determinations, so it is of little importance for this analysis.

Another limitation comes from the optical-depth issues in the EUV images, especially in the 171 Å band, close to the limb band (*Schrijver et al.*, 1994). To avoid optical depth issues, we don't utilize the EUVI image data between 0.98 and 1.025 $R_\odot$, as explained in Appendix D of *Frazin et al.* (2009). Due to the data rejection in this annulus and the consequent loss of information, we treat the tomographic reconstructions to be physically meaningful above heliocentric heights of 1.03 $R_\odot$.

The spherical computational grid covers the height range 1.00 to 1.26 $R_\odot$ with 26 radial, 90 latitudinal, and 180 longitudinal bins, each with a uniform radial size of 0.01 $R_\odot$ and a uniform angular size of 2° (in both latitude and longitude). It is not useful to constrain the tomographic problem with information taken from view angles separated by less than the grid angular resolution. Therefore, as the Sun rotates about 13.2° per 24 hour period, we time average the images in 6 hour bins, so that each time-averaged image is representative of views separated by about 3.3°. Also, due to their high spatial resolution (1.6″ per pixel), to reduce both memory load and computational time, we spatially rebin the images by a factor of 8, bringing the original 2048 × 2048 pixel EUVI images down to 256 × 256. Thus the final images pixel size is about the same as the radial voxel dimension. The statistical noise in the EUVI images is greatly reduced because of this spatial and temporal binning. Even so, the maximum height we consider is 1.20 $R_\odot$, as the reconstructions tend to be problematic above that height due to the weaker coronal signal.

The electron temperature of a given point on a magnetic field line from the PFSSM can be determined from the DEMT temperature (T_m) data. We trace individual field lines through the tomographic grid to obtain the temperature profile along the field line. This temperature profile is representative of the bundle of field lines that pass through the tomographic cells. The field line integration begins at the height of 1.075 $R_\odot$, in the center of the radial bin that begins at 1.07 and ends at 1.08 $R_\odot$, so that only field lines with apexes at 1.075 $R_\odot$ or higher are considered. (The field line

is traced in both the parallel and anti-parallel directions, so that the entire loop is determined.) This choice was made because we discard the tomographic data in the three cells between 1.0 and 1.03 $R_\odot$ due to optical depth effects, [1]. and we require each leg of the loop to pass through at least 5 tomographic cells above 1.03 $R_\odot$ in order to be included in this analysis[2] One effect of starting the field line integration at 1.075 $R_\odot$ is to avoid the low-lying small loops since any field lines closing below that height will not be seen. Open field lines are not considered in this analysis, although some previous results can be found in *Vásquez et al.* (2011).

For each field line i, we determine $T_m^{(i)}(r)$, where r is the heliocentric height, in each tomographic voxel along the loop. We then fit the $T_m^{(i)}(r)$ profile with a linear function

$$T = a\,r + b\,, \tag{2.1}$$

where the temperature gradient a and intercept b are the two free fitting parameters.

"Up" loops are those field lines for which $a > 0$, implying that the electron temperature increases with height and, and "down" loops are those for which $a < 0$, implying that the electron temperature decreases with height. Figure 2.1 shows a least-squares fits to a typical up loop and a typical down loop. The quality-of-fit metric we used is called R^2 and is commonly known as the coefficient of determination.[3] The maximum attainable value of R^2 is unity which can only be achieved when the fitted curve exactly agrees with all data points. We generated magnetic field lines every 2° in latitude and longitude from the PFSS model, for a total of 16,200 loop

[1]The most optically thick part of an image of the solar corona corresponds to a LOS that just grazes the limb. Lines of sight hitting disk terminate at 1.0 $R_\odot$, while those grazing the limb pass through more plasma. [We call this the "black ball" model in which the effect of the chromosphere is to terminate the LOS but not contribute to the optical depth.] Thus, the tomography algorithm makes use of LOSs that hit the center of the disk as well as those above 1.025 Rs, and it only ignores the image data between 0.98 and 1.025 $R_\odot$. The effect of ignoring this data makes part of the tomographic matrix ill-conditioned, resulting in unreliable emissivities in the radial range between about 1.0 and 1.03 $R_\odot$ (*Frazin et al.*, 2009).

[2]A "loop" is deemed to consist of two "legs," each ascending from a foot-point to the loop's apex.

[3]$R^2 \equiv 1 - S_{\rm res}/S_{\rm tot}$, where $S_{\rm res}$ is the sum of the squared residuals and $S_{\rm tot}$ is the sum of data's deviations from the mean.

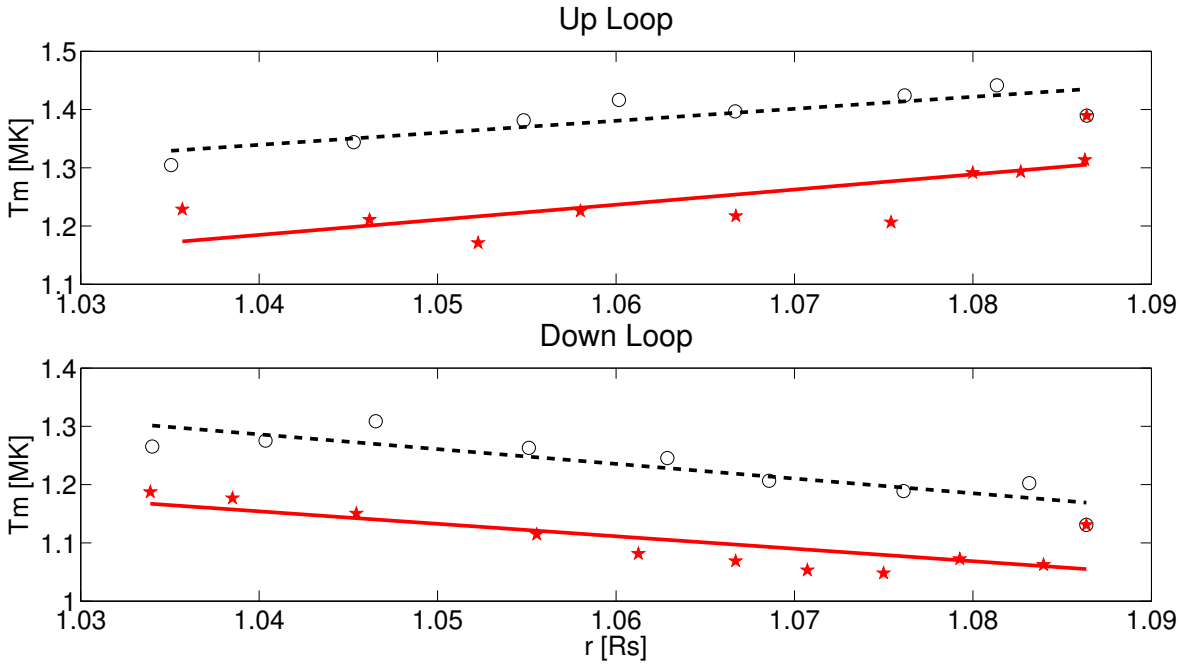

Figure 2.1: Linear least-squares fits of the form $T_m = a\,r + b$ to determine loop classification as "up" ($a > 0$), or "down" ($a < 0$). *Top:* Two legs of a up loop, with black circles representing the DEMT T_m values of one leg and red stars representing the other. The red solid line is the fit to the red stars and the black dashed line is the fit to the black circles. *Bottom:* Similar to the top panel, but for a down loop. The black dashed and red solid curves in the upper and lower panels have quality-of-fit values R^2 of 0.67, 0.51, 0.76 and 0.59, respectively. Since we only accept loops with $R^2 > .5$ (for this stage in the analysis), these fits are fairly typical.

foot-points. Of these, most were rejected for one or more of the following reasons:

- The field line is open according to the PFSSM.
- The field line is in, or too close to, the active region.
- The fitted temperature gradients a of the two loop legs do not have the same sign.
- The quality of the linear fit, $R^2 < .5$ for either leg of a loop.
- One of the two loop legs does not go through at least 5 tomographic grid cells with usable data.

Consequently, there are about 5500 loop legs left to examine the spatial distribution of up and down loops. We find that up loops are mostly located in high latitude regions and down loops in low latitude regions, as shown in Figure 2.2, which displays this spatial distribution at 1.075 $R_\odot$. Because the LDEM data are considered to be good up to about 1.2 $R_\odot$ for this data set, we separate both the up and down into large loops and small loops. A large loop is a field line with its apex beyond 1.2 $R_\odot$ and a small loop has its apex below 1.2 $R_\odot$, which means that the large loops do not have data for their portions above 1.2 $R_\odot$. The light blue areas in this figure are threaded by small down loops and the dark blue areas by large down loops. The orange areas are threaded by small up loops and red areas by large up loops. To better understand the foot-point distribution at the solar surface, we traced the loops to the solar surface to determine the latitude of the foot-point of each loop. We find that 96% of the down loops are located within $\pm 30^\circ$ latitude and 78% of up the loops are outside $\pm 30^\circ$ latitude, as shown in Table 2.1 [In this Table, only legs with $R^2 > .9$ in the hydrostatic fitting (see Section 2.2) are included.] A 3-D view of up and down loops is displayed in Figure 2.3. The white lines are open field lines, which are excluded in this study. The red lines are up loops and blue lines are down loops.

The field line integration code provides information about the loops, including their lengths. In this article the length of a loop L is defined as the foot-point-to-foot-point distance along the potential field line connecting them. Figure 2.4 shows histograms of the lengths of the up and down loops in Figure 2.2. While up loops are more likely to have lengths greater than about 0.5 $R_\odot$, both histograms have large populations below that length.

	# of loop legs	% of foot-points within $\pm 30°$ latitude	% of foot-points outside $\pm 30°$ latitude	average Loop Length [$R_\odot$]	average N_0 [10^8 cm^{-3}]	average P_0 [10^{-3} Pa]	average λ_N [$R_\odot$]	average λ_P [$R_\odot$]	average $\partial T_m/\partial r$ [MK/$R_\odot$]
Small Up Legs	4155	20	80	0.5	2.2	7.1	0.082	0.101	2.89
Large Up Legs	1255	42	58	1.46	1.9	6.2	0.095	0.114	1.73
Small Down Legs	2585	97	3	0.36	2.3	8.6	0.082	0.064	-3.7
Large Down Legs	57	86	14	1.27	2.2	8.2	0.082	0.071	-1.87

Table 2.1: Statistical Quantities of Small/Large up/Down Loops. N_0 and λ_N are the base density and density scale height, respectively, and P_0 and λ_P are the base pressure and pressure scale height, respectively [see Equations (2.2) and (2.4)].

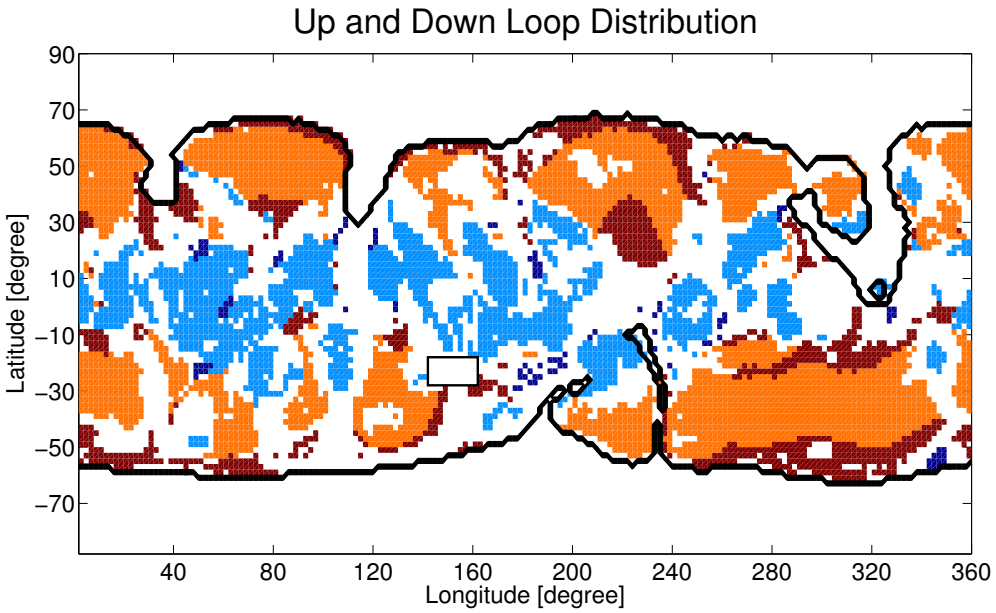

Figure 2.2: The spatial distribution of up and down loops at 1.075 $R_\odot$ with $R^2 > .5$ for the linear temperature fit [Equation (2.1), Figure 2.1]. The blue regions are threaded by down loops while the orange and dark red regions are threaded by up loops. Dark blue and dark red represent regions threaded by loops with apexes above 1.2 $R_\odot$, while light blue and orange represent loops with apexes below 1.2 $R_\odot$. The solid black line represents the boundary between open and closed field according to the PFSSM, and the white regions are excluded from our analysis for reasons listed in the text. The box near (-20,150) contains NOAA active region 11009.

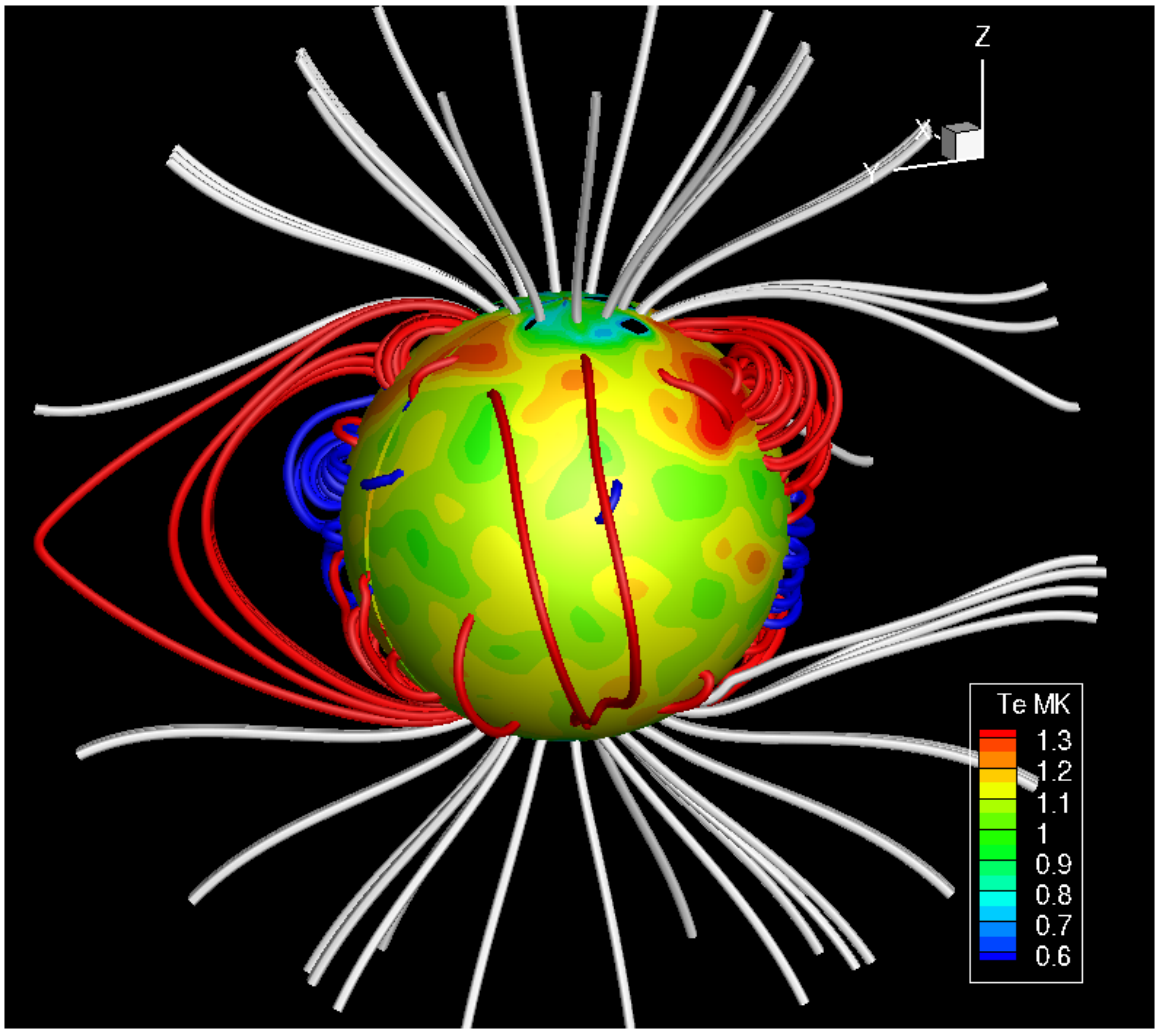

Figure 2.3: A 3D representation of the up and down loop geometry, with red and blue depicting up and down loops, respectively. The spherical surface has a radius at 1.035 $R_\odot$ and shows the LDEM electron temperature T_m according to the color scale.

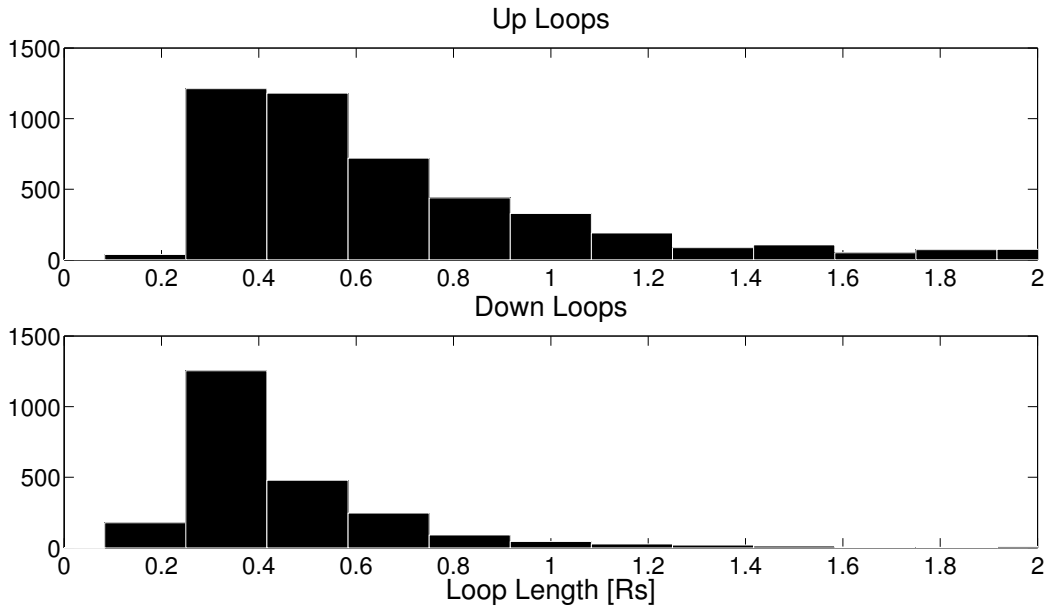

Figure 2.4: Histogram showing the distributions of loop lengths for the up (top panel) and down (bottom panel) loops, whose spatial distribution is displayed in Figure 2.2. While an up loop is more likely to longer than about $0.5R_{\odot}$, these distributions indicate that length cannot be the primary discriminating factor between up and down loops.

2.2 Scale Height Analysis

It is well known that an isothermal hydrostatic plasma has an exponentially decreasing pressure distribution. A plasma is considered to be effectively hydrostatic when it is in steady state and the inertial term is not important in the momentum equation. In the absence of temperature gradients, the hydrostatic solution to the 1D spherical momentum equation is given by:

$$P(r) = P_0 \exp\left[-\frac{\mathrm{R}_\odot}{r} \frac{(r - \mathrm{R}_\odot)}{\lambda_P} \right], \tag{2.2}$$

where r is the spherical radial coordinate, P is the pressure, P_0 is the pressure at 1.0 $\mathrm{R}_\odot$, and λ_P is the pressure scale height. The relationship between the pressure scale height and the total kinetic temperature is $\lambda_P = k_B T/(\mu m_H g_\odot)$, where $\mu = (1 + 4a)/(1 + 2a)$ is the mean atomic weight per electron, $a = N(\mathrm{He})/N(\mathrm{H})$ is the helium abundance, $g_\odot = GM_\odot/\mathrm{R}_\odot^2$, and G, m_H, $M_\odot$, and k_B are the gravitational, proton mass, solar mass and Boltzmann constants, respectively. The total kinetic temperature is given by:

$$T = T_e + T_\mathrm{H}/(1 + 2a) + aT_\mathrm{He}/(1 + 2a)\,, \tag{2.3}$$

where T_H is the proton temperature and T_He is the α particle temperature. If we take $a = 0.08$ and further assume $T_e = T_\mathrm{H} = T_\mathrm{He}$, we find that $T_e \approx 0.52\,T$. Similarly, the electron density profile is given by the equation:

$$N_e(r) = N_{e0} \exp\left[-\frac{\mathrm{R}_\odot}{r} \frac{(r - \mathrm{R}_\odot)}{\lambda_N} \right], \tag{2.4}$$

where N_{e0} is the electron density at 1 $\mathrm{R}_\odot$, and λ_N is the density scale height. Of course, under these assumptions $\lambda_N = \lambda_P$.

As DEMT provides us with empirical measures of both N_e and T_e, comparing

fitted values of λ_N to λ_P for a number of loops gives us the opportunity to test the assumptions under which Equations (2.2) and (2.4) are derived. In *Vásquez et al.* (2011), for many loops, we compared the loop-averaged value of T_e from DEMT ("T_m" in that paper) to the value of $0.52\,T$ ("T_{fit}"), which was derived from a fitted value of λ_N to the N_e values, also from DEMT. In that paper, we found that in the closed field regions the histogram $T_{fit} - T_m$ was clustered around 0, seemingly consistent with isothermal hydrostatic equilibrium. However, in the open field regions, the histogram $T_{fit} - T_m$ was clustered around a positive value, providing evidence for wave pressure gradients and/or having ions with higher temperatures than the electrons.

The loop study presented here is similar but attempts to provide an improved analysis, by taking advantage of our knowledge of the temperature variation along each loop. In *Vásquez et al.* (2011), T_m represented the average (measured) T_e along the loop, and did not take into account the measured temperature variations along the loop. As before, λ_N is fit to the N_e values for a given loop in this analysis. Figure 2.5 shows examples of these fits. New to this analysis, λ_P is fit to the measured pressures along each loop, with the pressure in the jth tomographic cell given by

$$P(r_j) = C\, N_e(r_j) T_e(r_j)\ , \tag{2.5}$$

where $C \equiv k_B[(2+3a)/(1+2a)]$, and $N_e(r_j)$, $T_e(r_j)$ are the DEMT values in cell j. Figure 2.6 shows two examples of fits to determine λ_P. We removed the legs that have bad hydrostatic fits ($R^2 < .9$ for either density or pressure fitting). Figure 2.7 shows a histogram of the differences between the two scale heights, λ_N and λ_P, where it can be seen that almost all of the up loops have $\lambda_P > \lambda_N$, while almost all of the down loops have $\lambda_P < \lambda_N$. It is not surprising that up loops have $\lambda_P > \lambda_N$, and vice-versa, as it follows from qualitative consideration of Equations (2.1) and (2.4): Given that the exponential model in Equation (2.4) fits the data well, a positive

temperature gradient will produce greater pressure at large heights than would be seen in an isothermal loop, thus making $\lambda_P > \lambda_N$. The opposite argument can be made for loops with negative temperature gradients.

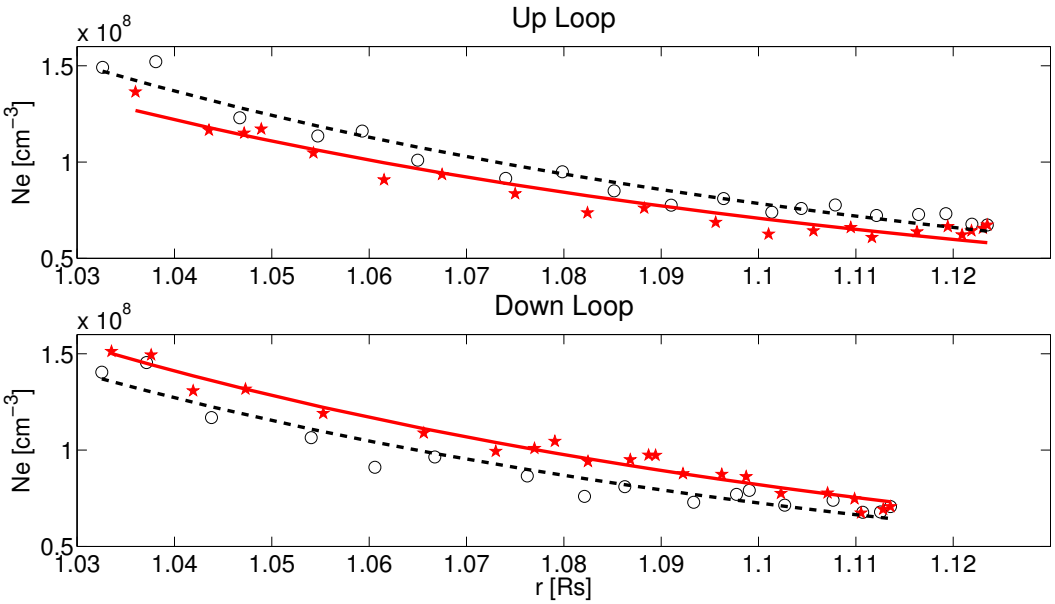

Figure 2.5: The upper and lower panels give examples of fits to determine the base density N_{e0} and density scale height λ_N, for an up and a down loop, respectively [Equation (2.4)]. The data points are the DEMT values of the electron density N_e. The symbols and line styles are as in Figure 2.1. The black dashed and red solid curves in the upper and lower panels have quality-of-fit values R^2 of 0.95, 0.94, 0.92 and 0.97, respectively. Since we only accept loops with $R^2 > .9$ for the scale-height analysis, these fits are fairly typical.

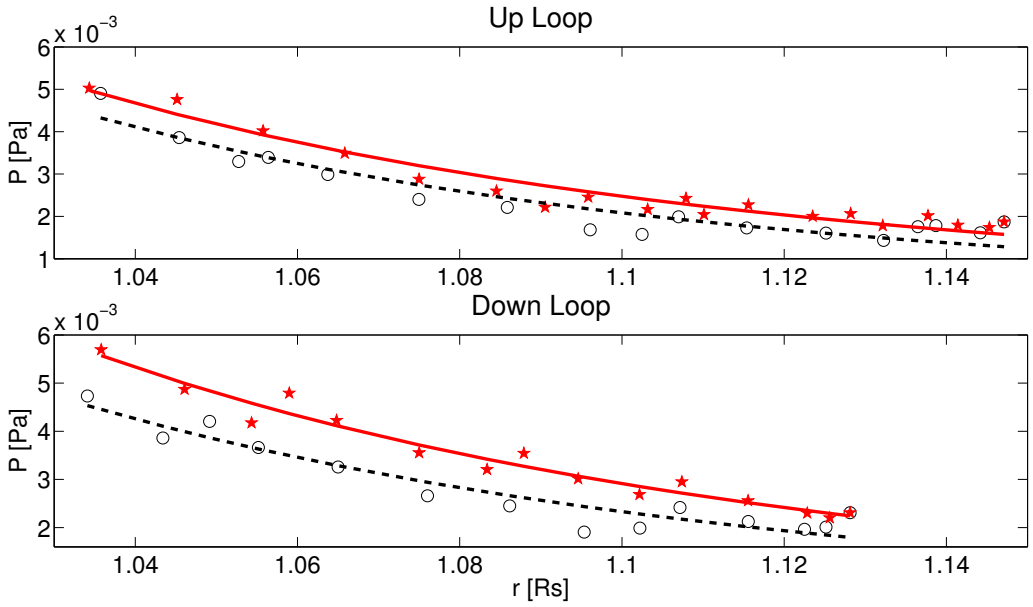

Figure 2.6: The upper and lower panels give examples of fits to determine the base pressure P_0 and pressure scale height λ_P, for an up and a down loop, respectively [Equation (2.2)]. The two loops shown here are the same two loops that are displayed in Figure 2.5. The data points are values of pressure determined from DEMT temperature and density using Equation (2.5). The black dashed and red solid curves in the upper and lower panels have quality-of-fit values R^2 of 0.89, 0.94, 0.91 and 0.96, respectively. Since we only accept loops with $R^2 > .9$ for the scale-height analysis, these fits are fairly typical.

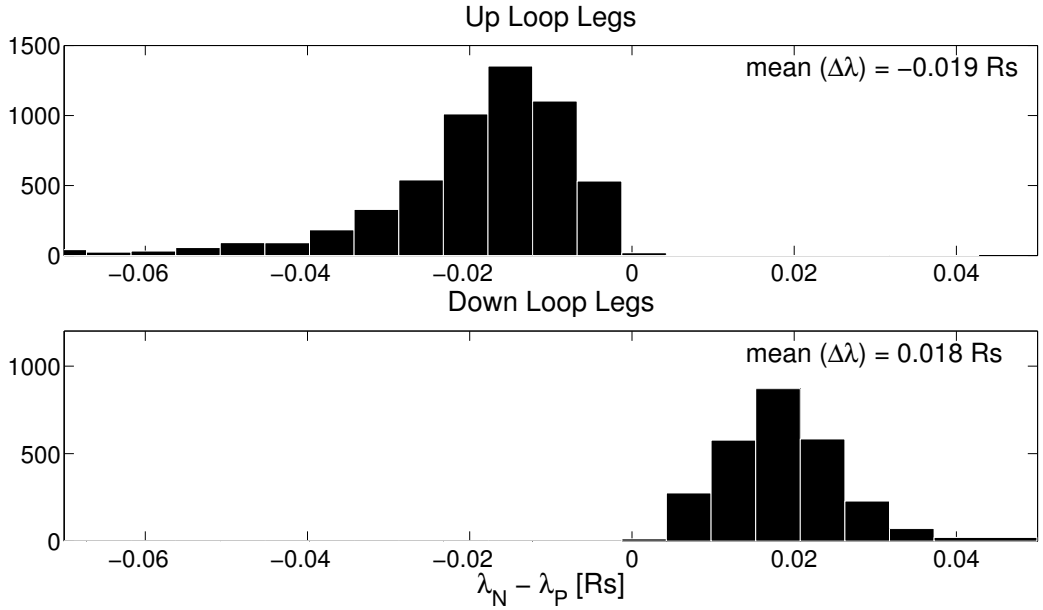

Figure 2.7: The top and bottom panels shows histograms of the scale height differences $\lambda_N - \lambda_P$ [see Equations (2.2) and (2.4)] for the legs of the up loop and down loops, respectively. The two histograms are plotted on the same horizontal scale. As expected, almost all of the up loops have $\lambda_P > \lambda_N$, while almost all of the down loops have $\lambda_P < \lambda_N$.

2.3 Discussion and Conclusions

We study quiet Sun (QS) loops at solar minimum with apexes at 1.075 $R_\odot$ or greater using the new Michigan Loop Diagnostic Technique (MLDT), which combines differential emission measure tomography (DEMT) and a PFSS model. This investigation has yielded three principal results:

1. Much of the QS is populated with "down" loops, in which the temperature decreases with height. "Up" loops, in which the temperature increases with height, are expected but down loops are a surprise.

2. The down loops are ubiquitous at low latitudes, while the up loops are dominant at higher latitudes, closer to the boundary between the open and closed magnetic field. (See Figure 2.2.)

3. The MLDT allows independent determination of the empirical pressure and density scale heights, λ_P and λ_N, respectively (see Figure 2.7).

One may question whether or not the down loops are simply an artifact of the MLDT and therefore do not exist on the Sun. We believe the Sun does exhibit down loops and that they are not an artifact of the MLDT, which is primarily limited by the similar temporal resolutions of the synoptic magnetogram and SRT, and the results presented are robust to the EUVI calibration uncertainties (see Appendix A). The various assumptions made in this analysis, while questionable for individual field lines, should be adequate to extract broad statistical trends, especially in QS plasma at solar minimum, and it is difficult to explain the trends shown here as non-physical.

To give our arguments more strength, we performed a non-tomographic DEM analysis, avoiding the temporal resolution issue (at the expense of loosing the 3D information from the tomography). This is shown in Figure 2.8, which is an image of the temperature derived from a traditional DEM analysis in two spatial dimensions.

We averaged 6 hourly images in the 171, 195 and 284 Å bands taken by EUVI-A between 6:00 and 12:00 on 2008 Dec. 9. [At 9:00 the central longitude of the solar disk was about 151°.] Similarly to the method used to calculate the LDEM, we assumed that the DEM has a Gaussian form with the free parameters being the height, centroid location and width [see also *Aschwanden et al.* (2011)]. Figure 2.8 is an image of the DEM mean temperature T_m, and the arrows indicate the 2D temperature gradient. Downward gradients can be seen near the equator on both the E and W limbs, supporting the existence of down loops. Upward temperature gradients, likely indicating up loops can be seen at larger latitudes.

With angular and radial spans of $2^\circ \times 2^\circ \times 0.01\,\mathrm{R}_\odot$, the tomographic grid cells are much larger than than the smallest observed widths of active region loops (< 1000 km), and one may wonder whether or not the down loops are an artifact of the spatial resolution and averaging over many elemental loops of different heights and temperatures. This seems unlikely since the loops we consider here have apexes above $1.075\,\mathrm{R}_\odot$, where the potential magnetic field does not have large gradients. Thus, all of the elemental field lines passing through a tomographic grid cell at this height must be roughly parallel and averaging over a the volume of a tomographic grid cell includes mostly loops of similar geometry.

Serio et al. (1981) arrived at a down loop solution, with a temperature minimum at the apex, but they concluded this solution would cause instabilities to destroy the loop when the loop half-length (the length of one leg), $L/2$, is greater than ~ 2 to 3 times the pressure scale height. If the loop length is small enough to keep the loop stable, then this solution is related to prominence formation. With average down loop lengths about 6 times the average scale heights (for the small loops) in Table 2.1, the data do not seem to support the loop destruction hypothesis, but this needs to be examined more closely. *Aschwanden and Schrijver* (2002) also found a down loop solution, but they did not discuss this solution in detail, as most loops were thought to be up loops.

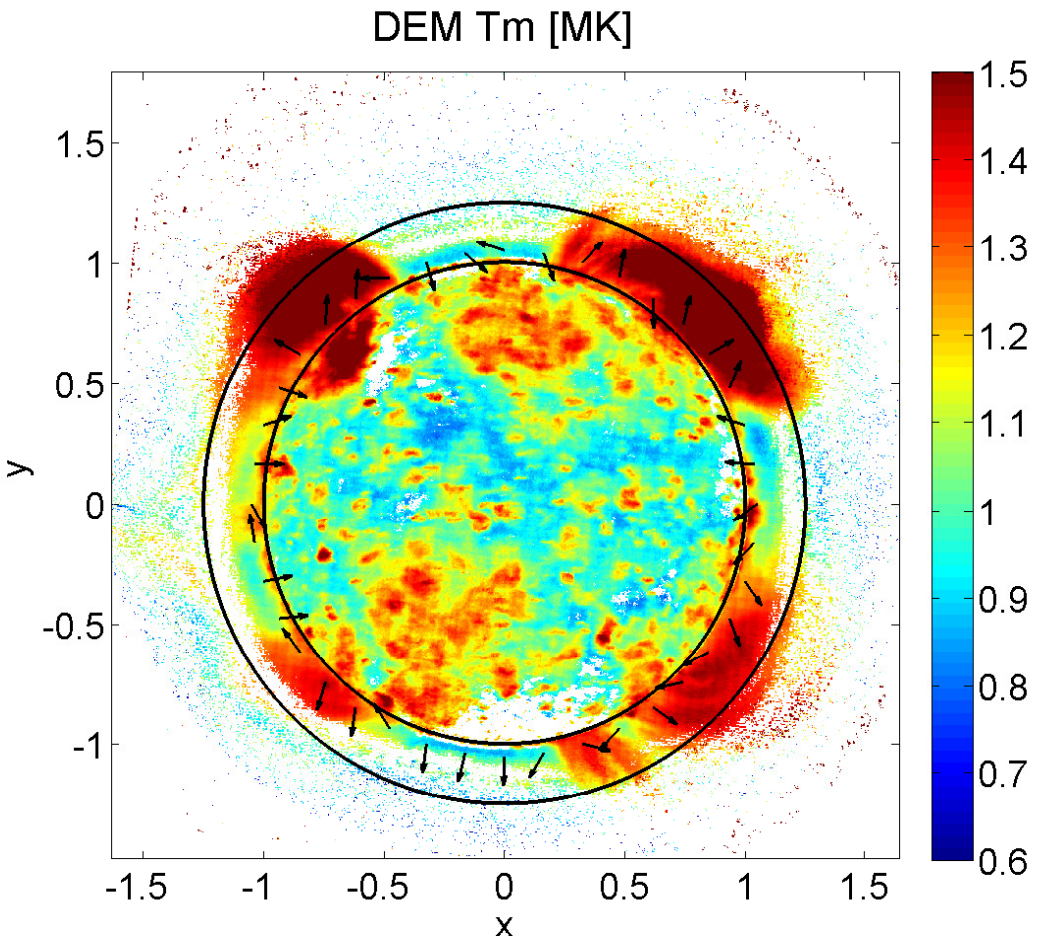

Figure 2.8: A determination of the DEM without tomography from 6 hourly images taken by EUVI-A between 6:00 and 12:00 UT on 2008 Dec. 9. The longitude of the central meridian was about 151°. Displayed is the mean of the DEM, T_m, which corresponds to the average electron temperature along the line-of-sight. The black arrows indicate the direction of the 2D gradient of T_m in the image plane. The arrows that point radially inwards near the and E and W limb are consistent with our finding of down loops. The inner and outer circles are at 1.0 and 1.2 $R_\odot$, respectively.

However, our results show that down loops are ubiquitous at low latitudes (see Table 2.1). Balancing electron heat conduction, radiative losses and ad-hoc heating, the hydrostatic loop model developed by *Aschwanden and Schrijver* (2002) shows that the height of the loop temperature maximum moves downward as s_H/L decreases, where s_H is the (exponential) heating scale length. Within this paradigm, down loops exist because s_H is much smaller than the loop length, meaning the heating is localized at the foot-point and the only process available to heat the apex is electron heat conduction. Up loops then are indicative of the heating scale length s_H being close to or larger than the loop length, implying roughly uniform heating along the loop. If the hydrostatic model developed by *Aschwanden and Schrijver* (2002) is descriptive of the real Sun, and if we assume that s_H is independent of latitude, then one would expect loop length to be an excellent discriminator of up and down loops. However, this does not seem to be the case, as Figure 2.4 shows that both up and down loops have large populations between 0.15 (the shortest length allowed in this analysis) and 0.5 $R_\odot$, and that any loop length less than about 1 $R_\odot$ is not a key variable in distinguishing the two populations. That said, the figure also shows that loops longer than about 1 $R_\odot$ are very likely to be up loops. Table 2.1 also indicates that the up loops tend to be longer than down loops, which is a direct contradiction of the hypothesis of hydrostatic loops with a scale height that is independent of foot-point location. The most reliable predictor of the up and down loop distribution is the foot-point latitude. Thus, if the quiet Sun plasma is mainly hydrostatic, these results indicate the heating scale length s_H varies with latitude, and that s_H is small in low latitude regions and large in high latitude regions. If the quiet Sun is not mainly hydrostatic, then dynamics must explain the fundamental differences between up and down loops.

As explained after Equation (2.5), elementary principles imply that up loops should be characterized by $\lambda_P > \lambda_N$, and down loops by $\lambda_N > \lambda_P$. However, at

this time, we lack a quantitive explanation of the distributions seen in Figure 2.7. Equation (2.5) is correct when $T_e = T_{\rm H} = T_{\rm He}$ and the wave pressure is negligible, and violation of this assumption is one possible avenue toward explaining discrepancies between observed values of λ_N and λ_P. We hope that the new observational properties of QS loops presented here will spur interest in studying the corona heating problem in these structures.

CHAPTER III

Stability of Inverted Temperature Loops in the Quiet Sun Corona

The Michigan Loop Diagnostic Technique (MLDT) is an empirical technique developed to study the global corona. This technique combines Differential Emission Measure Tomography (DEMT) with magnetic models to determine the electron density and electron temperature along individual magnetic field lines. DEMT is a reliable description of the stable regions of the corona (*Frazin et al.* (2009); *Vásquez et al.* (2010, 2011)), especially for the quiet corona in which individual loops can not be individually distinguished in the extreme ultraviolet (EUV) images. To the best of our knowledge, MLDT is the only way to study individual QS loops from observations. In Chapter II we used MLDT to study global temperature structure of the QS corona during Carrington rotation (CR)-2077, near the last solar minimum (CR-2081 was the solar minimum of solar cycle 23 and 24). By tracing the temperature profiles along each magnetic loop, two types of quiet Sun loops were identified: "up" loops in which the temperature increases with height, and "down" (inverted temperature) loops in which the temperature decreases with height. Furthermore, the "up" loop population were found to be dominant in high latitude regions while the "down" loops most often appear in low latitude regions. Figure 3.1 shows a typical example of a "up" loop and a "down" loop when considering the error bar of the temperature in

the DEMT results.

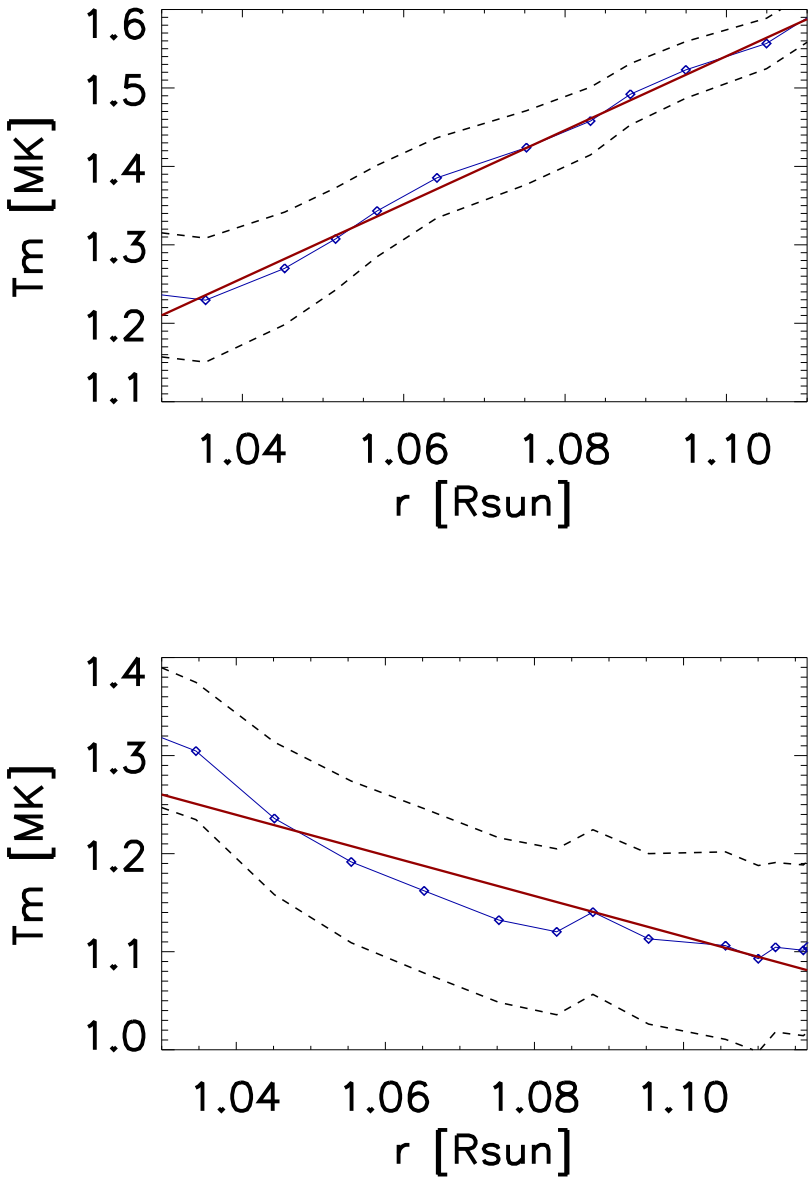

Figure 3.1: A typical example of a "up" ($a > 0$, *Top*) loop and a "down" ($a < 0$, *Bottom*) loop. Each panel shows one leg of a loop. The blue diamonds are the tomographically determined temperature (mean of the LDEM) as a function of heliocentric height. The black dashed lines are 1σ error curves that account for radiometric uncertainty, photon statistics, and uncertainty in tomographic regularization. The solid red line is a linear fit to the data points.

"Up" loops are expected while "down" loops are a surprise. The physics behind "down" loops and their spatial distribution is a mystery. There are only a few discussions of "down" loops. In hydrostatic coronal loop models, *Serio et al.* (1981) and *Aschwanden and Schrijver* (2002) pointed out if the heating scale height s_H is much smaller than the loop half-length L, a loop will reach its maximum temperature between its footpoint and its apex. If the maximum temperature is located below $1.03 R_{\odot}$, which is above the transition region and is the minimum radius of the DEMT data, then it is seen as a "down" loop in MLDT. In this case, "down" loops indicate the heating process is strongly localized near the footpoints. This newly discovered features of the solar corona will advance our understanding of the coronal heating problem in the closed magnetic field regions, which can provide constrain to 1-D loop models and 3-D global solar corona models. The physical origin of "down" loops is beyond the scope of this dissertation and is a possible future work, which will be discussed in Chapter V.

It is quite surprising that stable down-loops can exist on the Sun because there are no direct supporting observations for "down" loops. On the other hand, the "up" loops are well observed in active regions. We argue that "down" loops do exist in the quiet corona, even though they cannot be seen in EUV images because the quiet corona looks "diffuse" and "fuzzy". Quiet Sun analyses from *Feldman and Landi* (2008); *Warren* (1999) and *Landi et al.* (2002) have shown a nearly isothermal solar corona. But as the temperature difference in the range of LDEM (between 1.03 and 1.20 $R_{\odot}$) is small in both "up" and "down" loops, those results can be an artifact of line-of-sight effects. Figure 2.8 shows inward temperature in the off-limb Differential Emission Measure (DEM) T_e, which is an indirect support of the existence of "down" loops in the quiet Sun corona.

"Down" loops have received lots of arguments that they do not exist in the quiet Sun, because they are thermal dynamically unstable. *Field* (1965) studied the stabil-

ity of a dilute gas in mechanical and thermal equilibrium with a view to application to non-gravitational condensation phenomena in astronomy and showed that thermal equilibrium is unstable and can result in the formation of condensations of higher density and lower temperature than the surrounding medium under a wide range of conditions. But he did not discuss the specific heating which takes place in "down" loops. *Serio et al.* (1981) pointed out that if the heating scale height is less than $\frac{1}{3}$ of the loop half-lenght, then the loop will become a prominence and it is unstable against Rayleigh-Taylor instability. However, they also pointed out that if "... maximum and minimum temperatures differ by only a small amount", which is the case in "down" loops, and then the loop is stable. We argue that their model does not consider the support from the magnetic field and they concluded that the loop will be unstable due to Rayleigh-Taylor instability whenever they found a density inversion. As the magnetic field plays an important role in the solar corona, we can not ignore the magnetic field in dynamic processes. *Winebarger et al.* (2003) studied the static solutions of the hydrodynamic equations to investigate active region loop properties and they found that footpoint heating can result in density condensations in the apex, which means the density profile is inverted near the apex. In that case, small perturbations in the heating rate can cause the inverted temperature and density solutions to collapse to chromospheric values so the loop will eventually cool catastrophically.

In this chapter, we use the newly developed Alfvén Wave Solar Model (AWSoM) (*Sokolov et al.*, 2013; *Oran et al.*, 2013). AWSoM is driven by a synoptic magnetogram and with an upper chromospheric inner boundary. The solar corona is heated by Alfvén wave dissipation: along open field lines, the wave dissipation is due to Alfvén wave reflections, which result in imbalanced turbulence; while along closed field lines, there is additional wave heating from the counter-propagating waves coming from the two footpoints of a loop, which results in balanced turbulence at the apex of the loop. We use this model to investigate the stability of "down" loops to a given class

of perturbations.

3.1 Obtaining "Down" Loops with AWSoM

The newly developed Alfvén Wave Solar Model (AWSoM) (detailed discussions can be found in *Sokolov et al.* (2013) and *Oran et al.* (2013)) is implemented in the BATS-R-US (Block Adaptive Tree Solar Wind Roe-type Upwind Scheme) code (*Groth et al.*, 2000; *Powell et al.*, 1999) within SWMF (*Tóth et al.*, 2005, 2012). The new model starts from the top of the chromosphere, and includes the transition region. The distinctive feature of the new model is the incorporation of MHD Alfvén wave turbulence. We assume this turbulence and its nonlinear dissipation to be the only momentum and energy source for heating the coronal plasma and driving the solar wind.

The governing equations of the model include the two temperature MHD equations with Alfvén waves:

$$\frac{\partial \rho}{\partial t} + \nabla \cdot (\rho \mathbf{u}) = 0 \tag{3.1}$$

$$\frac{\partial (\rho \mathbf{u})}{\partial t} + \nabla \cdot (\rho \mathbf{u}\mathbf{u} - \frac{\mathbf{B}\mathbf{B}}{\mu_0}) + \nabla (P_i + P_e + \frac{B^2}{2\mu_0} + \frac{w_- + w_+}{2}) = -\rho \frac{GM_\odot}{r^3}\mathbf{r} \tag{3.2}$$

$$\frac{\partial \mathbf{B}}{\partial t} + \nabla \cdot (\mathbf{u}\mathbf{B} - \mathbf{B}\mathbf{u}) = 0 \tag{3.3}$$

$$\begin{aligned} &\frac{\partial (\frac{P_i}{\gamma - 1} + \frac{\rho u^2}{2} + \frac{B^2}{2\mu_0})}{\partial t} + \nabla \cdot [(\frac{\rho u^2}{2} + \frac{\gamma P_i}{\gamma - 1} + \frac{B^2}{\mu_0})\mathbf{u} - \frac{\mathbf{B}(\mathbf{u} \cdot \mathbf{B})}{\mu_0}] \\ &= -(\mathbf{u} \cdot \nabla)(P_e + \frac{w_+ + w_-}{2}) + \frac{N_i k_B}{\tau_{ei}}(T_e - T_i) + \Gamma_- w_- + \Gamma_+ w_+ - \rho \frac{GM_\odot}{r^3}\mathbf{r} \cdot \mathbf{u} \end{aligned} \tag{3.4}$$

$$\frac{\partial(\frac{P_e}{\gamma-1})}{\partial t}+\nabla\cdot(\frac{P_e}{\gamma-1}\mathbf{u})+P_e\nabla\cdot\mathbf{u}=-\nabla\cdot\mathbf{q_e}+\frac{N_ik_B}{\tau_{ei}}(T_i-T_e)-Q_{rad} \tag{3.5}$$

where $\mathbf{q_e}=-\kappa T_e^{5/2}\frac{\mathbf{BB}}{B^2}\cdot\nabla T_e$ is the field aligned thermal conduction with $\kappa=9.2\times 10^{-12}\mathrm{Wm^{-1}K^{-7/2}}$. $Q_{rad}=N_eN_i\Lambda(T_e)$ is the optically thin radiative energy loss term.

Equation (3.1) is the continuity equation, where ρ is the mass density, $\mathbf{u}$ is the velocity. Equation (3.2) is the momentum equation. In this equation, we already account the Alfvén wave pressure by introducing the Alfvén wave intensity terms w_+ (Alfvén waves propagating parallel to the mean magnetic field vector) and w_- (Alfvén waves propagating antiparallel to the mean magnetic field vector). Equation (3.3) is the induction equation for the magnetic field. Equation (3.4) and (3.5) are the energy equations applied to ions and electrons, respectively. The Coulomb collisional coupling between ion temperature and electron temperature are included in the equation by the term $\frac{N_ik_B}{\tau_{ei}}(T_i-T_e)$. The Alfvén wave dissipation energy is given by $\Gamma_-w_-+\Gamma_+w_+$ in the ion energy equation, where $\Gamma_\pm$ is the Alfvén wave dissipation rate. $\Gamma_\pm$ is given by

$$\Gamma_\pm=\frac{\sqrt{|B|}}{L_\perp\cdot\sqrt{|B|}}\sqrt{max(w_\mp,C_{refl}^2w_\pm)} \tag{3.6}$$

where $L_\perp$ denotes the transverse correlation length of turbulence, which corresponds as to the absorption length; and C_{refl} mimics the local Alfvén wave reflections due to inhomogeneities in the magnetic field and plasma. It is essential to point out that we do not calculate the reflections explicitly in this model; while in *van der Holst et al.* (2014), the reflections are explicitly calculated from the turbulence theory. The Alfvén wave energy density, $w_\pm$, is governed by the following equation within the WKB approximation:

$$\frac{\partial w_{\pm}}{\partial t} + \nabla \cdot (\mathbf{u} w_{\pm} \pm \mathbf{b} V_A w_{\pm}) + \frac{1}{2} w_{\pm} \nabla \cdot \mathbf{u} = -\Gamma_{\pm} w_{\pm} \tag{3.7}$$

in which the third term is the energy reduction in an expanding flow and the right hand side is the wave dissipitation

The beauty of the new model is that it only has three free parameters: the turbulent velocity pulsation, $\delta v_{\perp}$, which represents the Alfvén wave energy; the transverse correlation length of turbulence, $L_{\perp}$, which plays a similar role as the heating scale height s_H in other loop models (*Serio et al.* (1981); *Aschwanden and Schrijver* (2002)) and the reflection coefficient $C_{\rm refl}$, which describes the small ratio of the reflected wave amplitude to the bulk wave amplitude. *Sokolov et al.* (2013) and *Oran et al.* (2013) showed that AWSoM can capture solar corona features well with careful chosen parameters.

In order to study the stability of "down" loops, we simulate the solar corona with AWSoM for CR-2077, which is the same Carrington rotation as *Huang et al.* (2012). We apply the SOHO/MDI polar-interpolated synoptic magnetogram (*Sun et al.*, 2011) as the inner boundary condition. We first run the Finite Difference Iterative Potential-field Solver (FDIPS) developed by *Tóth et al.* (2011) to obtain the potential field as the initial magnetic field for the model. A spherical grid is used in the simulation. The inner boundary of the simulation domain is at $R = 1\mathrm{R}_{\odot}$; while the outer boundary is at $R = 24\mathrm{R}_{\odot}$. There are 3.2×10^5 blocks with 3.1×10^7 cells (each block has $6 \times 4 \times 4$ cells). AMR is performed to resolve the heliosphere current sheet (HCS) and the lower corona. In the LDEM range (between 1.03 and 1.20 $\mathrm{R}_{\odot}$), the cell size is around $0.01\mathrm{R}_{\odot} \times 1.5^{\circ} \times 1.5^{\circ}$, which is similar to the tomographic grid size.

With the suggested parameters in *Sokolov et al.* (2013), no "down" loops are found in the simulation. So we need to specify another set of parameters in AWSoM in order to obtain "down" loops. As discussed in the introduction, "down" loops

indicate that heating is localized near the footpoints of the loops. So we increase the Alfvén wave reflection coefficient $C_{\rm refl}$ and decrease the $L_\perp$ in the model, which increases the heating rate near the footpoints. With several experiments, we find that setting $C_{\rm refl} = 0.7$ and $L_\perp \cdot \sqrt{|\mathbf{B}|} = 45$ kmT$^{1/2}$ can produce "down" loops in the solar corona. Even though $C_{\rm refl}$ is almost an order larger than the suggested value by *Sokolov et al.* (2013), we believe this indicates that some non-linear effects are not described very well within a global model, especially small-scale heating (i.e., phase mixing, turbulent cascade, and resonate abortion), which might take place in the real corona. It is difficult to include those small-scale heating into global simulations due to the cost in computational time.

3.2 Stability of "Down" Loops

Many methods can be applied to study the stability of "down" loops. We only discuss three most common methods here. The first one is the analytical solution to the linearized equations, which describe the time evolution of the small perturbations in the system. The stability condition can be obtained from the dispersion relation by considering all the small perturbations should be damped in the time evolution. *Antiochos* (1979) derived the stability condition of a quasi-static coronal loop and found that the loop with vanishing heat flux at the loop base are unstable. However, one has to make many assumptions (i.e., the heating function of a loop as well as the boundary conditions and the loop configurations) to make this method solvable. *Antiochos* (1979)'s solution only holds with specific heating and cooling functions as well as a uniform pressure loop, which generally is not the case in the solar corona. There is one major difficulty to apply this method in the stability study of "down" loops: the availability of the analytical heating function of a "down" loop. As the heating functions must be prescribed in the derivations, which is not available in "down" loop study yet, this method is not applicable in the current study.

The other two methods are related to numerical simulations. The first one is doing eigenmode analysis of the system matrix. The 3-D global numerical simulation can be solved in a discretized generalized eigenvalue problem ($Ax = \lambda Bx$, in which A and B are matrices, x is a solution vector and λ is the eigenvalue) (*Strang*, 1988). If none of the eigenvalues of the system is related to unstable solution, then the system is stable against linear perturbations. However, this method does not detect nonlinear instabilities. matrix in a global simulation is huge and it is extremely expensive the find the eigen mode of such a huge matrix. The second one is performing a time-accurate numerical simulation by imposing perturbations near the apex of a "down" loops. If the "down" loop is unstable, it will exhibit unstable process which will finally destroy the loop. If the "down" loop is stable, it will return to its original solution. This is the currently available in the AWSoM model, so we apply the this method to study the stability of "down" loops in this section.

We first simulate the steady-state solar corona with AWSoM using the parameters described in the previous section which can successfully produce "down" loops in the solar corona. We then extract a "down" loop in the 3-D simulation and impose perturbations near the apex of the "down" loop by decreasing 10% the pressure. We do not disturb the electron density, so the pressure perturbation is the same as the temperature perturbation in this study. After that, we simulate the "down" loop evolution with time-accurate solver. The results are discussed in the following paragraphs.

Figure 3.2 shows the evolution of T_e in several time steps. The upper left panel shows the steady-state result while the middle panel shows the T_e just when we impose the perturbations. The upper right panel shows T_e after 2 minutes of simulations and the lower three panels shows the simulations 4 minutes later, 6 minutes later, and 2 hours later, respectively. This figure shows that 2 hours after imposing perturbations, the "down" loop returns to its steady-state solution. The physical explanation is that

after we decrease the electron temperature near the apex, which decreases the pressure near the apex, the loop is no longer in steady-state. Under the force unbalance condition, there are flows from the footpoints to the apex; and the Alfvén wave and heat conduction will bring more heat to the apex and finally the temperature in the apex will return to its steady-state solution as indicated in the lower right panel. The plasma flow process can be seen more clearly in the the evolution of N_e, which is shown in Figure 3.3. As just explained, after imposing the perturbations, the pressure in the apex is lower than its steady-state; thus there are flows from the footpoints to the apex which leads to the density increase in the upper right panel and the lower left and lower middle panel. When the pressure in the apex is large enough, there will be flows from the apex to the footpoints so the density will decrease again (which does not show here). This flow patten will continue until the "down" loop reaches its steady state solution again, which is showed in the lower right panel. Both Figure 3.2 and 3.3 support the fact that "down" loops are stable against Rayleigh-Taylor instability.

The next step to prove that "down" loops are stable in numerical simulation is to carry out grid convergence study to see whether the stability comes from the numerical scheme in the model; because there are numerical diffusions in all MHD codes and numerical diffusions can stabilize simulations. And we cannot remove numerical diffusions in our MHD simulation which are inherent in all numerical codes. We can reduce the numerical diffusion by decreasing the grid size, as the numerical diffusion is proportional to the grid size. If "down" loops are stable, they should remain stabile as the resolution is increased. In this study, we run the simulation in two different resolutions, one with the resolution used in Section 3.2 (cell size is $0.01\mathrm{R}_\odot \times 1.5^\circ \times 1.5^\circ$) and the other doubling the resolution, which means the new cell size is $0.005\mathrm{R}_\odot \times 0.75^\circ \times 0.75^\circ$. Figure 3.4 shows the grid convergence results. The y-axis shows the temperature difference between the simulated temperature after the

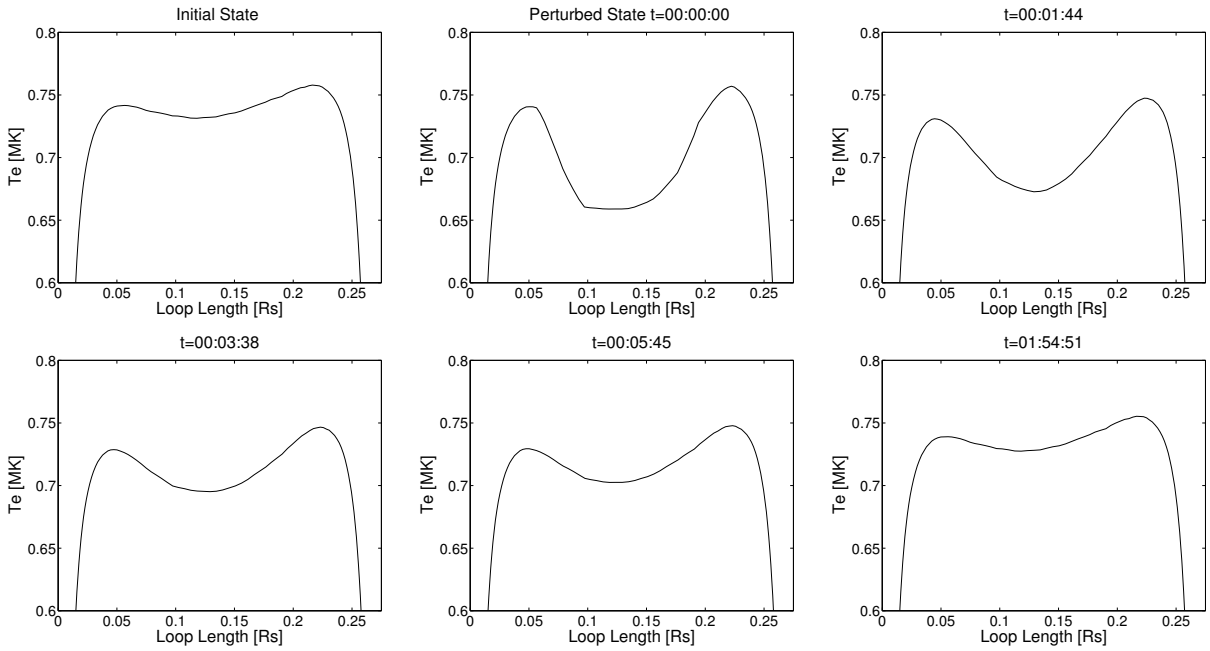

Figure 3.2: The evolution of T_e in different time step. The x axis is the loop length in the unit of $R_\odot$ while y axis is the T_e. The title in each panel shows the time of the time step.

perturbations and the steady-state apex temperature in logarithmic scale and the x-axis shows the simulation time. As the figure shows, the apex temperature returns to its steady-state value in both numerical simulations, supporting the fact that "down" loops are stable. From this figure, if we consider that steady-state is restored when the perturbed temperature is at 99% of the steady-state value, then the "down" loop return to its steady-state solution with three hours.

3.3 Discussion and Conclusions

In Chapter II we discovered a new class of loops, "down" loops in which the temperature decreases with height, in quiet Sun corona during solar minimum. "Down" loops have received arguments that they can not exist in the solar corona due to thermal instability. We address the stability issue of "down" loops in this chapter, by performing numerical simulations using the newly developed AWSoM. We find

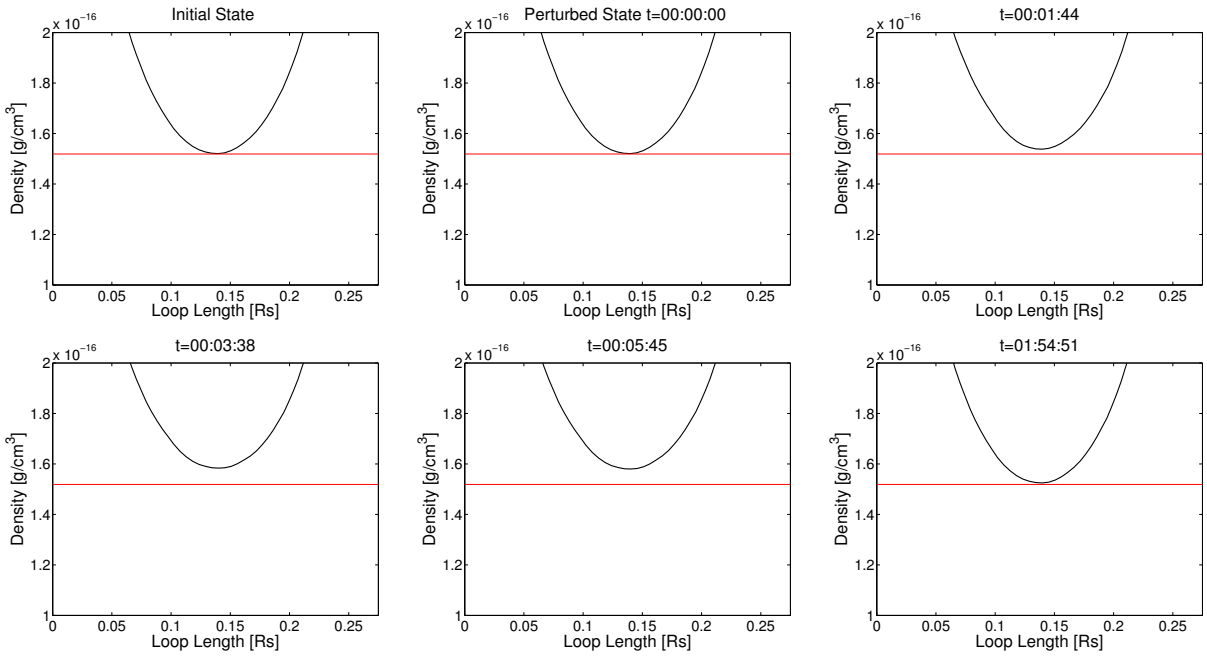

Figure 3.3: The evolution of N_e in different time step. The x axis is the loop length in the unit of $R_\odot$ while y axis is the N_e. The title in each panel shows the time of the time step. The horizontal red line shows the minimum N_e in the steady-state solution.

that the perturbed "down" loop returns to its steady state solution within three hours of simulation time, showing "down" loops are stable against small temperature perturbations near the apex.

Serio et al. (1981) simply concluded that their class II loop, which has the maximum temperature in a intermediate position between the footpoint and the apex, is unstable whenever there is density inversion (the density increases with height), due to Rayleigh-Taylor instabilities. This picture is too simple because magnetic field plays an important role in dynamic processes in the solar corona and may provide extra support of the heavier plasma near the apex. But if we compare our simulation results with the stability criteria in *Serio et al.* (1981), we find that "down" loops do not suffer the instability proposed by *Serio et al.* (1981), because during the simulation, the density profile keeps monotonically decreased as seen in Figure 3.3.

Nearly all discussions of stability in coronal loops are based on perfectly symmetric

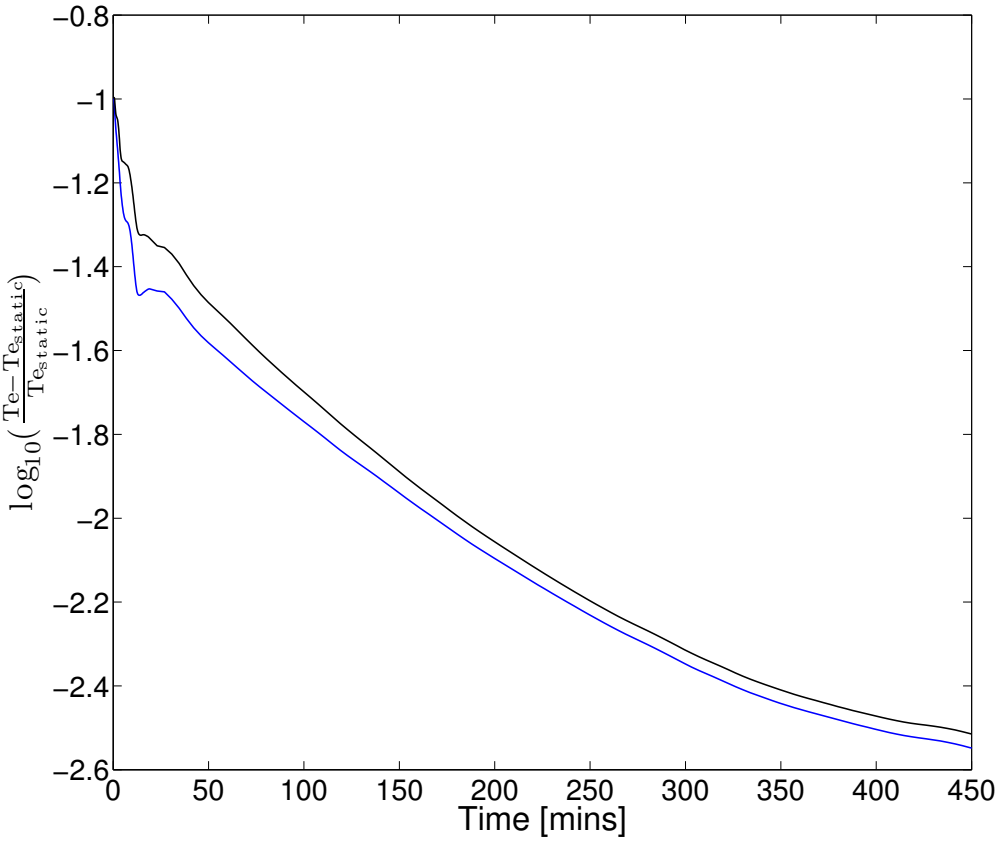

Figure 3.4: The grid convergence results. The y-axis shows the temperature ratio between the simulated temperature (after the perturbations) and the steady-state apex temperature, in logarithm scale. The x-axis shows the simulation time. The black curve is in the low resolution while the blue curve is in the high resolution.

loop models (*Serio et al.*, 1981; *Winebarger et al.*, 2003), which are a rare case in the real Sun corona. A better approach would be corona loop models with siphon flow (*Cargill and Priest*, 1980; *Orlando et al.*, 1995b). But those models again are based on symmetric loop configuration, they only specify different boundary conditions in two footpoints to include siphon flows in the simulations. There are no detailed discussion about the stability in siphon flow models; but *Aschwanden* (2004) pointed out that the flows along the loop can wipe out small perturbations in the loop and thus make the loop more stable. We also argue that active region loop models can not be applied in quiet Sun study, because all active region loop models assume that plasma beta β is much smaller than unity, in which case the magnetic field can be 'neglected' in dynamic processes. However, as we will see in Chapter IV, plasma beta in "down" loops is generally larger than unity, indicating that the magnetic field is important in "down" loop dynamics. The model we use, AWSoM, is a 3-D MHD model, which solves the MHD equations and incorporate sophisticated Alfvén wave heating source, is a more realistic approach in "down" loop study.

Radiative-driven instability is important in the solar corona. Various methods have been applied to study the radiative-driven instability (*Field*, 1965; *Antiochos*, 1979; *Habbal and Rosner*, 1979; *Oran et al.*, 1982; *Peres et al.*, 1982; *Klimchuk et al.*, 1987). *Klimchuk et al.* (1987) performed numerical simulations and found that low-lying compact hot loops are thermally unstable while large hot loops are stable. *Schrijver* (2001) analyzed observations over active regions from Transition Region and Coronal Explorer (TRACE) and found evidences of loop evacuation in the corona when the loop apex temperature has cooled to transition-region or even chromospheric temperatures. They performed numerical simulations and showed that if the loop heating drops by 1.5 orders of magnitude or more, the catastrophic cooling will develop as the heating is insufficient near the apex. We argue that their conclusions are based on active regions, where there are much more dynamic processes than quiet

Sun regions. There are no observations showing catastrophic cooling in quiet Sun corona. From Fiugre 3.2, we do not see the apex temperature reaches transition-region or even chromospheric temperatures in our simulations, which explains that there are no catastrophic cooling phase in our simulations. Recent study by *Cargill and Bradshaw* (2013) showed that the critical temperature for catastrophic cooling of a coronal loop is ¿ 1MK in flares, 0.5-1MK in active regions, and 0.1MK in long tenuous loops. As we study quiet Sun loops, we speculate the critical temperature is between 0.1MK and 0.5MK. Again, throughout the simulations, the apex temperature never reaches the critical temperature, which supports our conclusion that "down" loops are stable against small pressure perturbations.

CHAPTER IV

Evolution of the Global Temperature Structure of the Solar Corona During the Minimum between Solar Cycles 23 and 24

Observational evidence of coronal heating, in the form of temperature diagnostics of the Sun's corona, is needed to improve our understanding of the solar atmosphere. The combination of *differential emission measure tomography* (DEMT, based on time series of EUV images) with magnetic field models of the solar corona can provide global temperature constraints for the lower corona (below 1.25 $R_\odot$). This approach, named the *Michigan Loop Diagnostic Technique* (MLDT), is based on tomographic reconstructions and hence it is a reliable description of the stable regions of the corona, in particular of the quiet (diffuse) corona for which individual loops can not be individually distinguished in the EUV or x-ray images. MLDT was first used to study Carrington rotation (CR)-2077, during the minimum between solar cycles (SC)-23 and 24 in Chapter II. By tracing the tomographic temperature variation along many QS loops, it was found that, for large number of them, the temperature decreases with height. These loops were called "down" loops. Furthermore, it was found that down loops were characteristic of the equatorial region, being mainly located in the range of latitudes $\pm 30^\circ$, while outside that range most loops showed an increase of temperature

with height, the so-called "up" loops. Independent observational evidence for down loops in the same range of heights of our analysis (1.0 to 1.2 $R_{\odot}$), has been recently found by *Krishna Prasad et al.* (2013), who analyzed several temperature sensitive line ratios in off-limb UV spectra and found decreasing temperatures with height.

From a theoretical perspective, hydrostatic down loops can be expected if the heating is strongly localized in the footpoint and the apex is mostly heated by electron heat conduction (*Aschwanden and Schrijver*, 2002; *Serio et al.*, 1981). If the heating is assumed to have an exponential dependence with height, down loops can be expected if the heating scale height s_H is much smaller than the loop length L (*Aschwanden and Schrijver*, 2002). The latitudinal distribution of down loops and up loops found in Chapter II indicates that the heating scale length s_H varies with latitude, being smaller in the low latitude regions. Similar mechanisms to those causing wave damping at low heights in coronal holes (*Hahn et al.*, 2012) could be operating in the low latitude region within the streamer belt, where the down loop population is observed. The down loop population seen in CR-2077 may be related to the relatively simpler configuration of the magnetic field (mainly dipolar and quadrupolar), as well as to the possibly weaker magnetic strengths, that characterized that specific rotation, and how Alfvén waves are dissipated in inhomogeneous fields. A natural question follows: is the down loop population strongly dependent on the level of activity and complexity of the solar corona? This query motivated the study in this Chapter, in which we apply the MLDT analysis to eleven rotations that sample the last minimum and the surrounding descending and ascending phases, belonging to SCs 23 and 24, respectively. As we will show, down loops are characteristic of the deep minimum, being much less present away from this time, supporting the idea of heating mechanisms being modulated by the evolving coronal magnetic field.

4.1 MLDT Analysis and EUV Data

To analyze the evolution of the up/down distributions around solar minimum, in this work we extended the study in Chapter II to eleven rotations between CRs 2055 and 2106. New to the analysis for each rotation, we compared the up/down populations to sunspot numbers. Figure 4.1 shows the monthly sunspot number (black dots) for SC-23 and 24, provided by the National Oceanic and Atmospheric Administration (NOAA) Space Weather Prediction Center. The blue solid curve is the smoothed monthly sunspot number, as provided by the International Space Environment Service (ISES). The smoothed monthly sunspot value is obtained averaging all monthly values from 6 months before to 6 months after the current month (month 0), then using a total of 13 months of data. The weights all have value unity, except for the outer months (months -6 and $+6$) which have a value of $1/2$. This algorithm provides the monthly number using the yearly-scale trend, which is useful to evaluate the monthly data in the context of a longer time scale tendency.

With these sunspot counts as a contextual reference, we analyzed the following eleven CRs: 2055, 2065, 2068, 2071, 2074, 2077, 2078, 2081, 2084, 2099 and 2106. The first one corresponds to April 2007, while the last one corresponds to January-February 2011. There was a one-year long period that showed a near-zero count (less than 3) in the smoothed monthly sunspot number, from July 2008 to June 2009 (see Figure 4.1). Hereafter, we will refer to this period as the "deep-minimum". Five of the rotations we analyzed were chosen to be within and around that period, they are: CRs 2071 (June-July 2008), 2077-2078 (November 2008 - January 2009), CR-2081 (March-April 2009), and CR-2084 (June 2009). Rotations 2077, 2078 and 2081 sample the center of the deep-minimum period. Rotations 2071 and 2084 sample the end of the descending phase, and the beginning of the subsequent ascending phase, respectively.

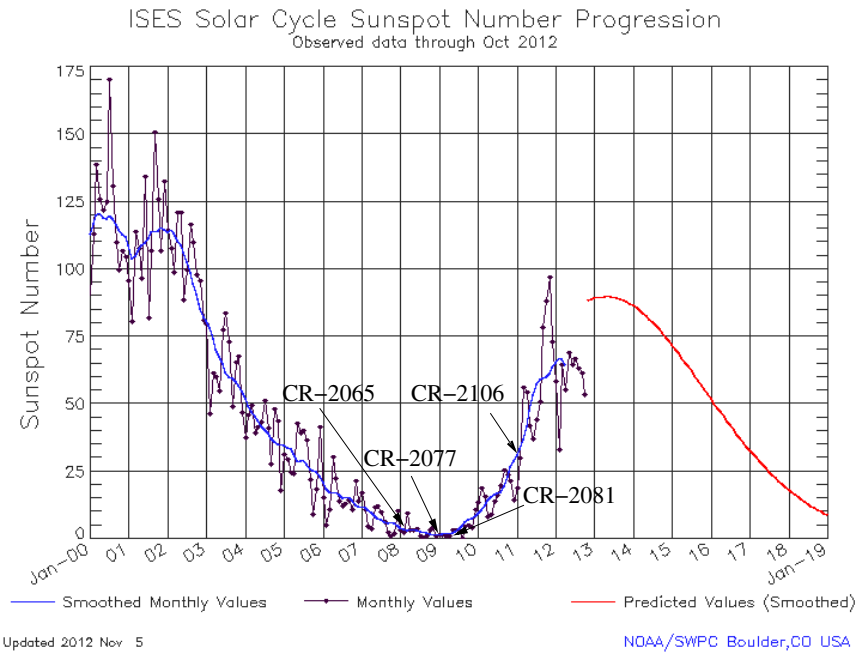

Figure 4.1: Monthly sunspot number for SC-23 and 24, provided by the National Oceanic and Atmospheric Administration (NOAA) Space Weather Prediction Center (reproduced from `http://www.swpc.noaa.gov/SolarCycle/`). The blue curve is the smoothed monthly sunspot number (see description in text), as provided by the International Space Environment Service (ISES). We indicate the data points that correspond to four rotations for which we performed the MLDT analysis.

4.1.1 MLDT

The detail of MLDT is discussed in Chapter II. In summary, the MLDT combines tomographic reconstructions (DEMT) of the 3D distribution of the DEM, which provides the electron density and temperature in the corona, with a magnetic model of the global corona. So far, only potential field source surface (PFSS) models have been used. The combination of the DEMT products with the PFSS models allows determination of the electron density and electron temperature along individual magnetic field lines for the global corona. This is achieved by *tracing* individual field lines of the PFSS model and evaluating the DEMT products along them.

Each closed magnetic loop of the PFSS model is divided in two *legs*, defined as the two segments that connect the loop apex with the photosphere. The DEMT temperature $T_m(r)$ is traced along each leg through the tomographic grid, where r is the heliocentric height, and the the data is fited with a linear function $T_m(r) = a\,r + b$. The slope of the linear fit a and the intercept b are the two free fitting parameters evaluated for each leg. The parameter a is then the fitted temperature gradient dT_m/dr along each leg of a loop in the height range covered by the tomography. It is the sign of a of any given loop what is used to classify it into the up or down kind, as anticipated in the introduction, and only loops having the same sign of a in both legs are counted. For each leg, the DEMT electron density is also traced and a hydrostatic (HS) fit is applied to the data. Thus, the base electron density N_0 and the density scale height λ_N are also determined for each leg of all loops. These procedures are explained in Chapter II.

To trace the field lines from the PFSS model through the tomographic solution of each rotation, we generated one starting point at the center of each tomographic cell at the height 1.075 $R_\odot$, that is every 2° in latitude and longitude, for a total of 16200 points. The magnetic field line of the PFSS model passing through each of these points was traced both outwards and inwards, until the coronal base (1.0 $R_\odot$)

and/or the source surface (2.5 $R_\odot$). Only one point per tomographic cell was then kept. This point of the magnetic field line was assigned the values of the DEMT products T_m and N_e corresponding to the tomographic cell where it is located. The DEMT products along each closed field line were then separately grouped into the two legs. The linear fit was then applied to the $T_m(r)$ values of each leg separately, and the quality of each fit is measured by computing its coefficient of determination R^2.[1] As in Chapter II, we based our analysis only on those field lines for which all following conditions hold:

- The field line is closed according to the PFSSM.
- The temperature gradient of the linear fit to the temperature of both legs of the loop has the same sign.[2]
- The quality of the linear fit is $R^2 > 0.5$ for both legs of the loop.
- Both legs of the loop go through at least 5 tomographic grid cells with usable data.

As an example, a 3D view of both up (red) and down (blue) loops for CR-2081 is displayed in Figure 4.2. For the same rotation, Figure 4.3 is an image of the mean temperature T_m for CR-2081, corresponding to the same view-angle as Figure 4.2. A DEM inversion is performed at each pixel, using the same technique applied to invert for the LDEM (*Vásquez et al.*, 2010), but determinated from the simultaneous images taken in the three coronal bands of EUVI-B. The mean temperature T_m of each pixel is then computed as in Equation 1.7, but using the DEM instead of the LDEM. Overplotted in the image, the arrows indicate the 2D temperature gradient

[1] $R^2 \equiv 1 - S_{\rm res}/S_{\rm tot}$, where $S_{\rm res}$ is the sum of the squared residuals and $S_{\rm tot}$ is the sum of datas deviations from the mean.

[2] For the different rotations we analyze in this chapter, the fraction of closed loops that are excluded from the analysis by this second requirement ranges between 8 and 17 %. The different sign maybe due to real physical differences or unresolved dynamics.

at different locations. Downward gradients can be seen near the sector on both the E and W limbs, consistent with the up and down loop distributions. As in Chapter II, this image shows that the presence of up and down loops is not an artifact of tomography.

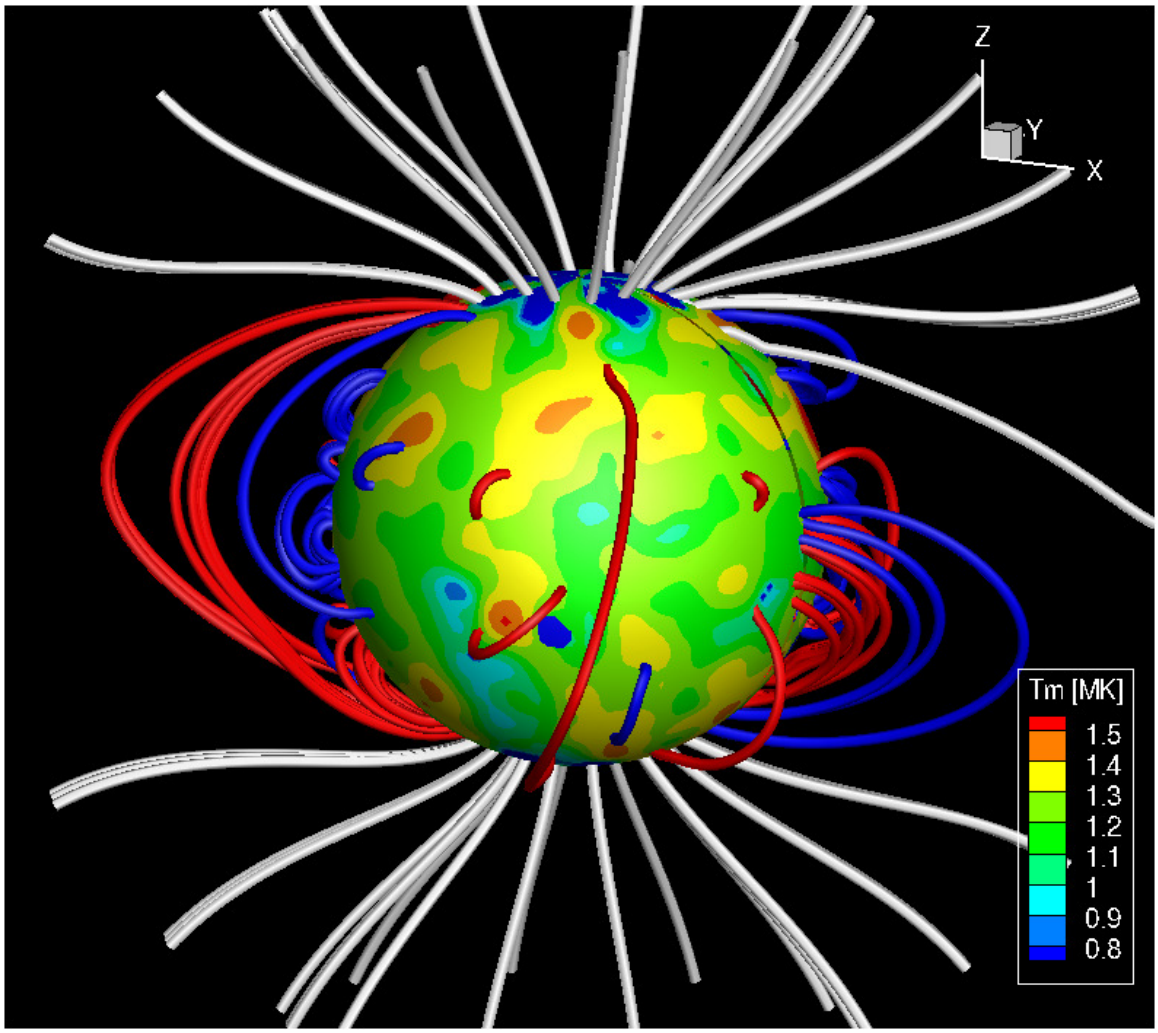

Figure 4.2: Three-dimensional representation of the up and down loop geometry for CR 2081, with red and blue depicting up and down loops, respectively. The central Carrington longitude was 118°. The spherical surface has a radius at 1.035 $R_{\odot}$ and shows the LDEM electron temperature T_m according to the colour scale.

As an example, Figure 4.4 shows the DEMT temperature profile along four loops, and the corresponding least-squares fits to the data along the two legs of each loop.

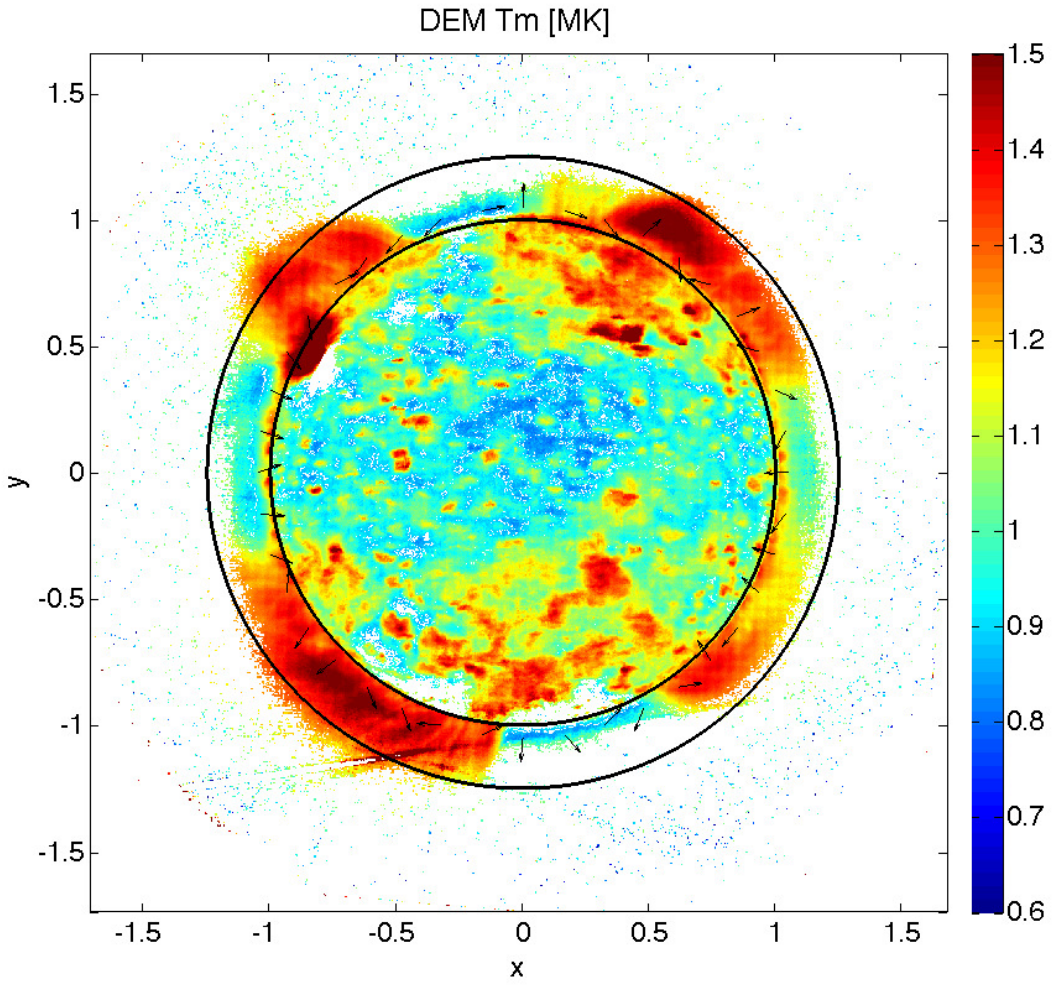

Figure 4.3: A determination of the DEM without tomography from 6 hourly images taken by EUVI-B between 6:00 and 12:00 UT on 2009 March 24. (CR 2081) corresponding to the same angle of vision that the Figure 4.2. Displayed is the mean of the DEM T_m, which corresponds to the average electron Temperature along the line of sight. The black arrows indicate the direction of the 2D gradient of T_m in the image plane.

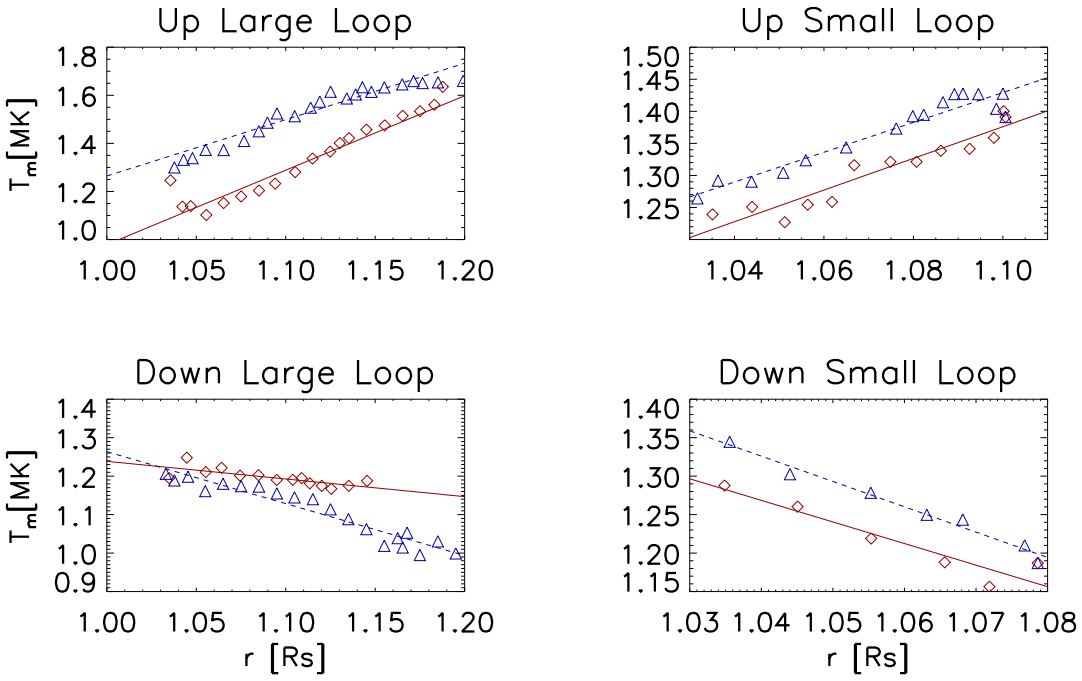

Figure 4.4: Least-Squares fits of the form $T_m = a\,r + b$, used to classify loops as "up" ($a > 0$), or "down"($a < 0$). Each panel shows the fits to each of the two legs of a selected loop, with red diamonds representing the DEMT T_m values of one leg and blue triangles representing the values along the other one. The top panels show two examples of up loops, with the left panel showing a large case (with apex above 1.2 $R_\odot$), and the right one a small case (with apex below 1.2 $R_\odot$). The bottom panels show two examples of down loops, a large one (left panel) and a small one (right panel).

The examples include up and down loops, and for each case one example has apex above 1.2 $R_\odot$ ("large" loop, hereafter), and another one below 1.2 $R_\odot$ ("small" loop, hereafter). We highlight this difference as we used the DEMT data up to 1.2 $R_\odot$. Hence, small loops are fully contained in the DEMT grid, while large loops extend beyond the spatial range of the DEMT data[3]. For the same loops shown in Figure 4.4, Figure 4.5 shows the corresponding HS fits to the DEMT electron density.

The pressure is also computed along each field line as $P = C\,N_e\,T_m$, where $C =$

[3]More than 70 % of the loops that are rejected from the analysis due to having different sign of the temperature gradient in both legs are of the large kind.

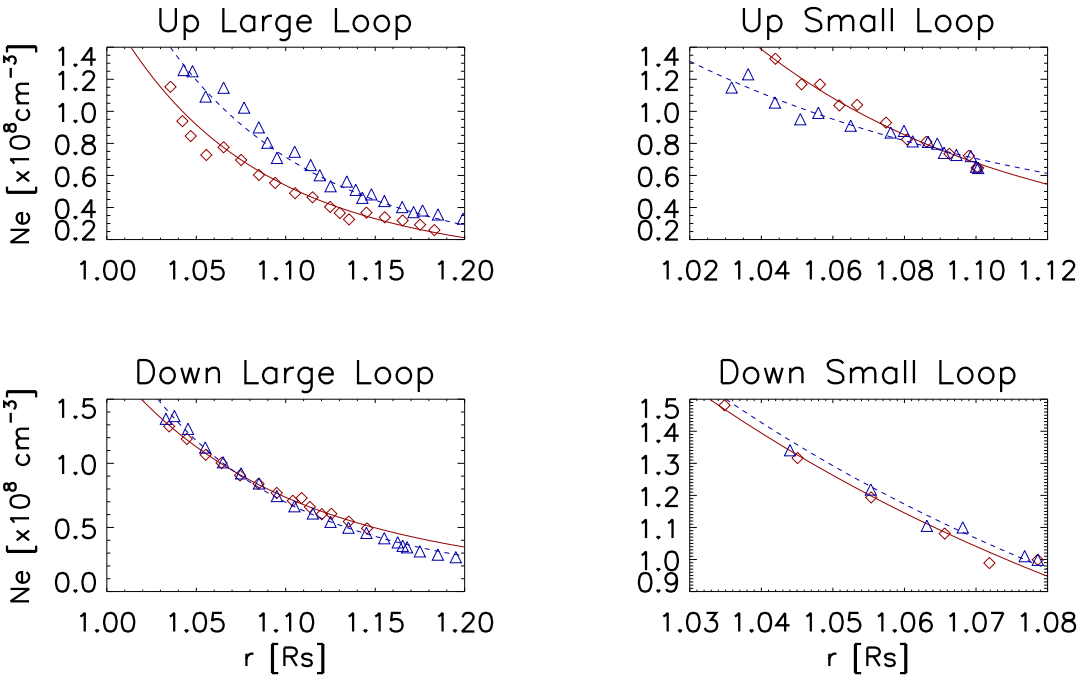

Figure 4.5: For the same four loops selected in Figure 4.4, these panels show the respective HS fits to the DEMT electron density along the two legs of each loop. The HS fits allow determination of the base density N_0 and scale height λ_N for each loop.

$k_B[(2+3A)/(1+2A)]$, $A = N(He)/N(H) \approx 0.08$ is the assumed ratio of helium and hydrogen abundances, and N_e and T_m are the local values from DEMT. We then apply a HS fit to the pressure data, so that the base pressure P_0 and scale height λ_P are determined for each leg of all loops. Using the pressure P and the PFSS magnetic field, we computed the plasma parameter $\beta = P/P_{mag}$, where $P_{mag} = B^2/8\pi$, along each field line.

4.1.2 Data Sources

For each rotation, the DEMT analysis was performed with images taken by the Extreme UltraViolet Imager (EUVI) instrument aboard the B spacecraft of the *Solar Terrestrial Relations Observatory* (STEREO), and the PFSS model was computed using as boundary condition the corresponding synoptic magnetogram from the *SOlar*

and Heliospheric Observatory (SoHO) Michelson Doppler Imager (MDI). Since the final MDI synoptic data corresponds to CR-2104, we used the synoptic magnetogram provided by the National Solar Observatory (NSO) Global Oscillation Network Group (GONG) for CR-2106. We compared the MLDT results using alternative PFSS models based on one magnetogram source or the other for rotations for which both sources were available, specifically for CR-2065 of the declining phase of SC-23 and for CR-2078 of the deep minimum. In tracing the DEMT results along the field lines, we found no significant differences in the statistics of the results, clearly indicating very similar geometries for the magnetic field in both models. There is a systematic shift of the GONG magnetic field strength to lower values when compared to the MDI magnetograms. This implies a shift to larger values of the plasma β for the GONG based MLDT results, not changing the relative results for the up and down populations. Once corrected for the shift in magnetic field strength, the GONG based MLDT results are in agreement with those based in MDI magnetograms. We defer to a future effort details on the corrections required when changing between the different magnetogram sources, including also results based on the Helioseismic and Magnetic Imager (HMI) on board SDO. For the purposes of this work we do not apply such corrections, and it suffices to say that our results are statistically robust to the choice of magnetogram source.

4.1.3 Regularization Level of the Tomography

For all tomographic reconstructions we set the tomographic regularization parameter at $p = 1.0$, a typical value for the size of the images and the tomographic grid we used (*Frazin et al.*, 2009). Before detailing our main results in the next section, we anticipate that in the case of CR-2077 they are very similar to those previously published in Chapter II. The cause for slight differences is twofold: a) a different value for the regularization parameter of the tomographic reconstruction was used,

b) a different polar correction for the magnetic field of the PFSS model was used. The differences are not statistically significant and thus the MLDT results are robust to both effects.

In this work we took the chance to further investigater the effect of the regularization level on the MLDT results. For CRs 2065, 2081, 2084, 2106, which sample the deep minimum and the ascending and descending phases, we computed the uncertainty in the fraction of up and down loops due to the regularization level of the tomographic reconstructions. For each of these rotations we varied the regularization parameter value in a range of appropriate values $p = 1.0 \pm 0.5$ (*Frazin et al.*, 2009; *Vásquez et al.*, 2010, 2011). For each rotation we computed the fraction of down and up loops for the different regularization levels, and used these values to compute their uncertainty, that we found to be of order 8%. In addition, Chapter II showed that the statistical results of the MLDT technique are robust to the uncertainty of the radiometric calibration of the EUVI channels.

4.2 Results

In this section we show detailed results for two rotations of the deep-minimum period, specifically CRs 2077 and 2081, and also for two rotations that sample the descending and ascending phases, namely CRs 2065 and 2106, respectively. We also show a summary of the main results for all eleven rotations we analyzed.

Figure 4.6 shows results of the DEMT and MLDT concerning the temperature structure of the global corona for two rotations of the deep minimum, namely CR-2077 (left panels) and CR-2081 (right panels). The top panels show Carrington maps of the DEMT T_m at the tomographic grid height 1.075 $R_\odot$. We overplot PFSSM magnetic strength B contour levels (solid-thin black and white curves), as well as the magnetically open/closed region boundaries (solid-thick black curves). The black regions correspond to locations undetermined by the tomographic reconstruction due

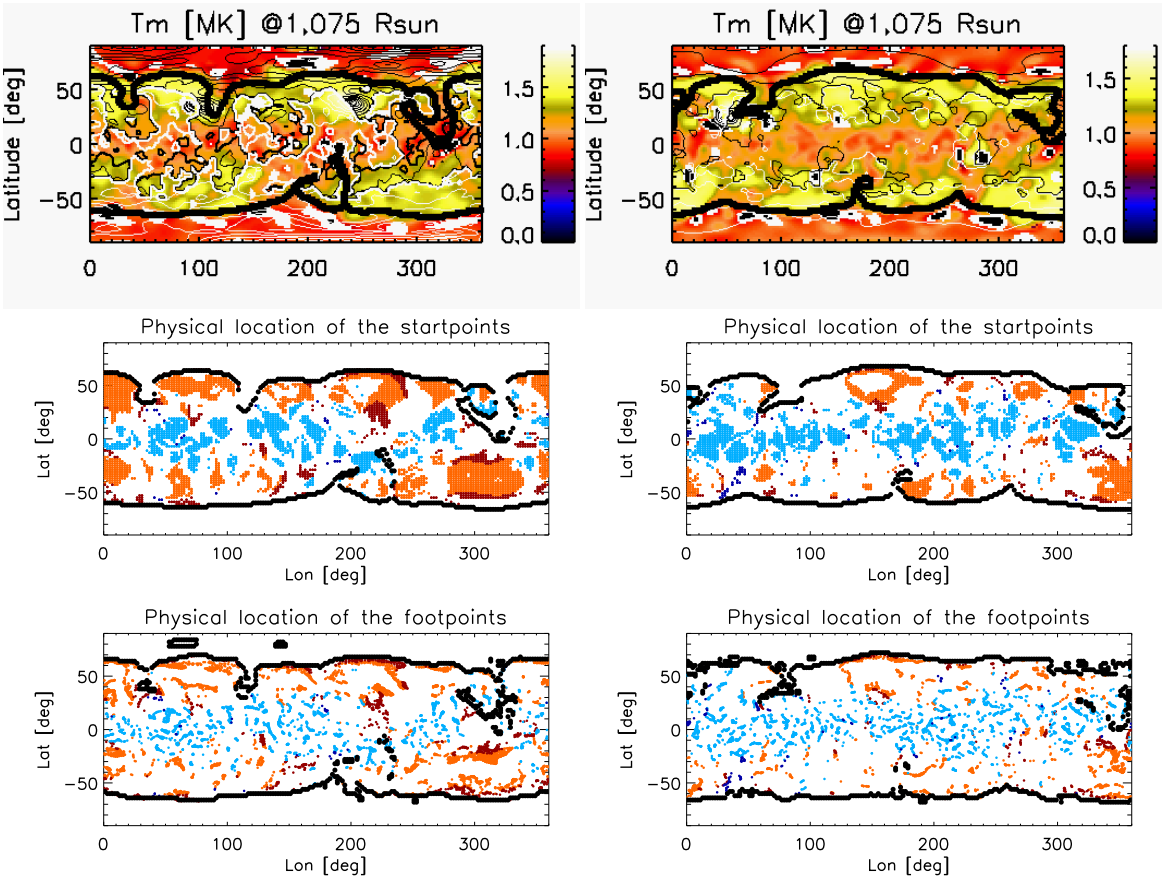

Figure 4.6: Temperature structure of CR-2077 (left) and CR-2081 (right), as revealed by the MLDT study. Top panels: Carrington maps of the DEMT T_m at 1.075 $R_\odot$. Middle panels: spatial distribution of the up (orange and dark red) and down (light and dark blue) loops at 1.075 $R_\odot$. Bottom panels: spatial distribution of the up and down loops at 1.0 $R_\odot$. In the top and middle panels, the thick black curves represent the boundary between open and closed field according to the PFSSM at 1.075 $R_\odot$, in the bottom panels the thick black curves represent the boundary open/closed field at 1.0 $R_\odot$. In the top panels, the thin black/white curves are contour levels of the magnetic strength B with negative/positive polarity. In the middle and bottom panels, dark blue and dark red represent regions threaded by loops with apexes above 1.2 $R_\odot$, while light blue and orange represent loops with apexes below 1.2 $R_\odot$. The white regions are excluded from our analysis as they are threaded by loops that do not meet all conditions itemized in Section 2.

to dynamics (called *zero density artifacts*, see *Frazin et al.* (2009)), and the white regions represent voxels for which the LDEM model does not successfully reproduce the tomographically reconstructed emissivities (see *Nuevo et al.* (2012); *Vásquez et al.* (2012)). The middle panels show the spatial distribution of the up (orange and dark red) and down (light and dark blue) loops at 1.075 $R_\odot$, and the bottom panels show the same at 1.0 $R_\odot$. In the middle and bottom panels, dark blue and dark red represent regions threaded by large loops, while light blue and orange represent small loops. In the top and middle panels the thick black curves indicate the open/closed boundary at 1.075 $R_\odot$, in the bottom panels the thick curves indicate the open/closed boundary at 1.0 $R_\odot$.

Figure 4.6 shows that, at deep-minimum, down loops are ubiquitous at low latitudes, while the up loops are located at intermediate latitudes, nearer to the open/closed boundary. The location and number of up and down loops are quantified in Figure 4.7. For CR-2077 (left) and 2081 (right), the top panels show frequency histograms of the fitted temperature gradient of the loops of Figure 4.6, measuring the relative fractions of the up and down loop populations. In the same figure, the middle and bottom panels show the frequency histograms of the latitudinal distribution of the up and down loops, respectively. The mean latitude of the down and up loops is located in all cases within 3 degrees of the equator. The distribution of down loops is uni-modal and its small mean latitude is consistent with how they are distributed at low latitudes near the equator. The distribution of up loops is bi-modal, with one peak at a mid latitude in each hemisphere, so that its small mean latitude summarizes how they are symmetrically distributed around the equator.

Figure 4.8 is similar to Figure 4.6 but for rotations CR-2065 (left panels) and CR-2106 (right panels), farther from deep minimum, during the declining phase of SC-23 and the ascending phase of SC-24, respectively. It is readily seen that the down loop population is diminished when compared to the deep minimum rotations, while the

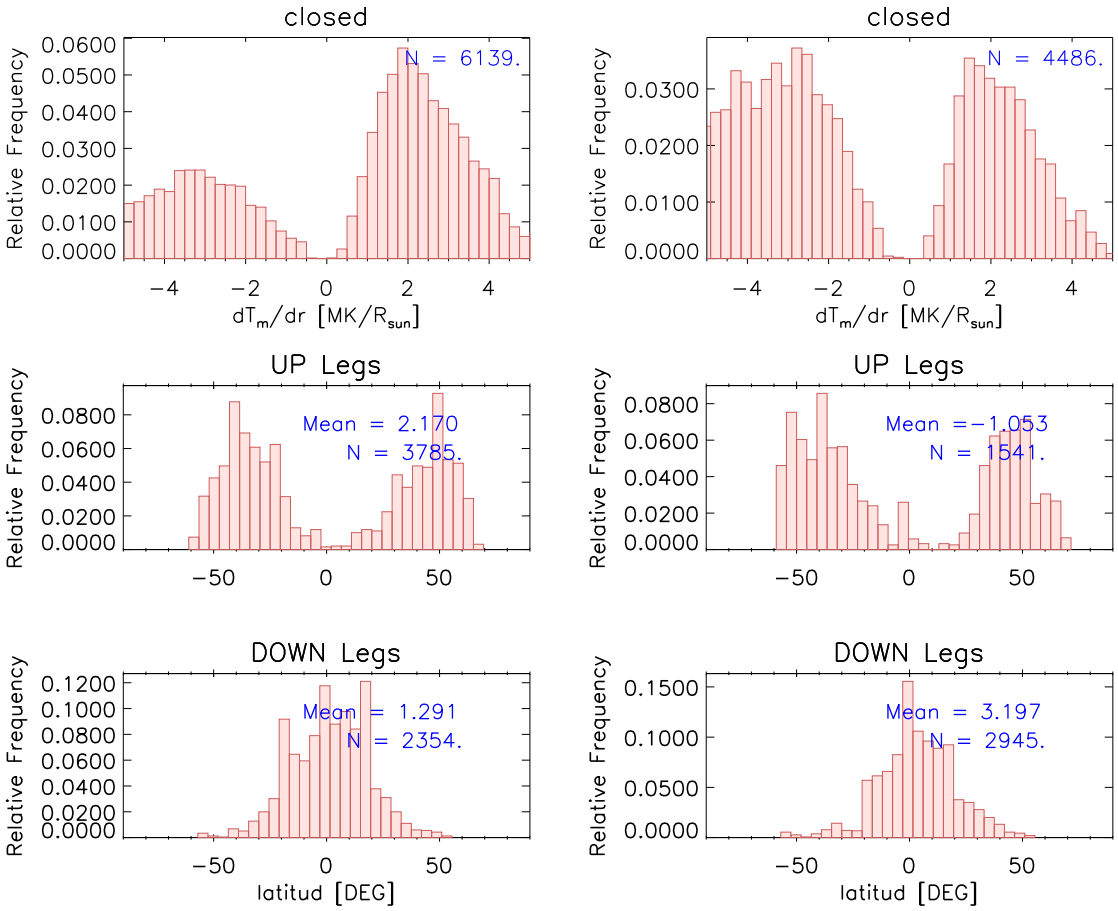

Figure 4.7: For CR-2077 (left) and CR-2081 (right), the top panel shows the frequency histogram of the fitted temperature gradient along the legs of the up and down loops in the closed region. The middle and bottom panels show the frequency histogram of the latitudinal distribution at 1.075 $R_\odot$ for the legs of the up loops and down loops, respectively.

up loop population is enhanced. The latitudinal distributions of up and down loops are similar to those during deep minimum. This is shown in the histograms of Figure 4.9. The mean latitude is within 6 degrees of the equator for down loops, and within 15 degrees for up loops. These larger departures from the equator, when compared to the deep minimum rotations, are consistent with the progressive loss of symmetry in the coronal structure during these more active rotations (specially for CR-2106 that shows the largest departure from the equator).

Comparing the three panels of Figures 4.6 and 4.8, we note that the up loops

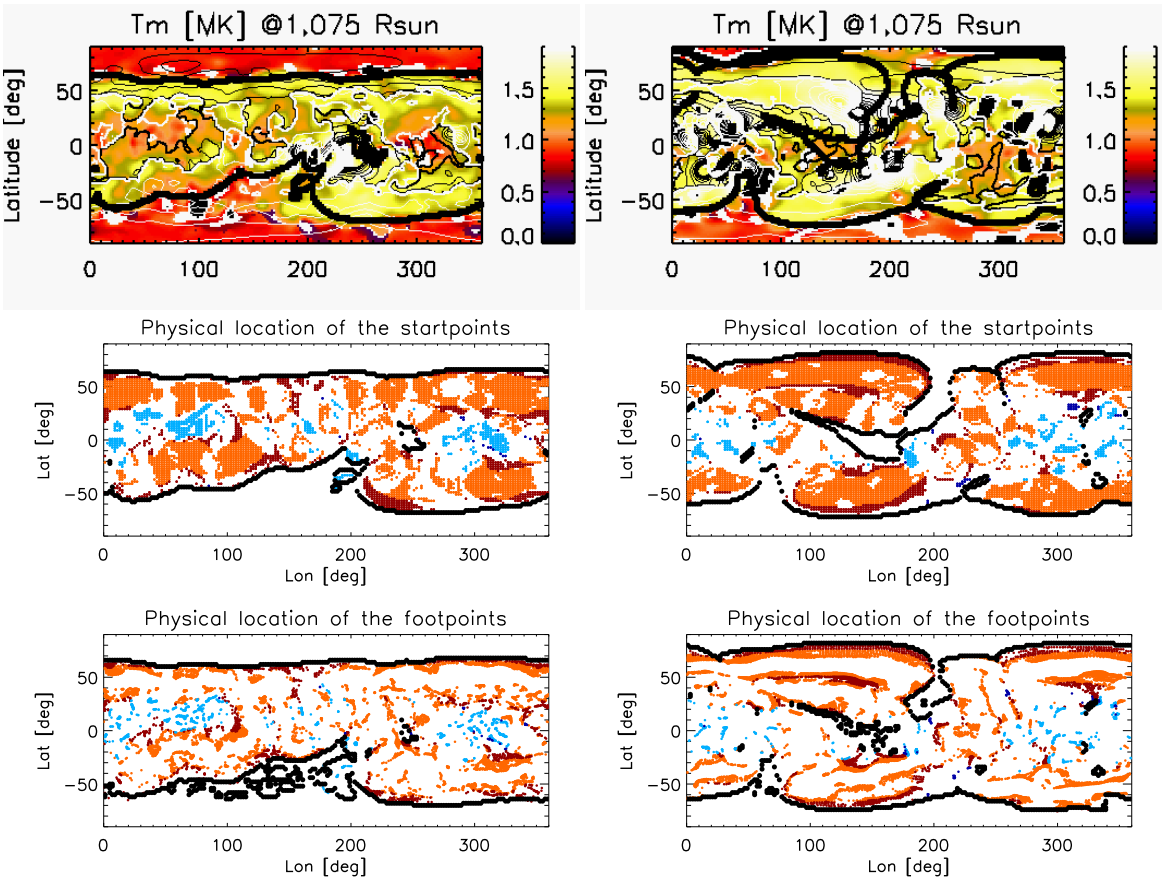

Figure 4.8: Same as Figure 4.6 but for rotation CR-2065 (left) and CR-2106 (right).

tend to be somewhat hotter than the down loops. Quantitative information for these trends is shown in Figure 4.10, displaying for each rotation the scatter plot of the fitted temperature gradient dT_m/dr versus the average temperature T_m along each leg ($\langle T_m \rangle$). For the deep minimum rotations CR-2077 and CR-2081, the mean ratio of the average temperature of the up loops over that of the down loops is 1.26 and 1.23, respectively. Noting that the most active regions of the corona exhibit the higher temperatures, a comparison of the top and middle panels of these Figures also indicates that down loops are mostly located in the quiet sun regions. Up loops are located in both active and quiet sun regions.

Table 4.1 summarizes statistical information of the four rotations shown in Figures 4.6 through 4.9. All quantities are calculated separately for up and down loops, as

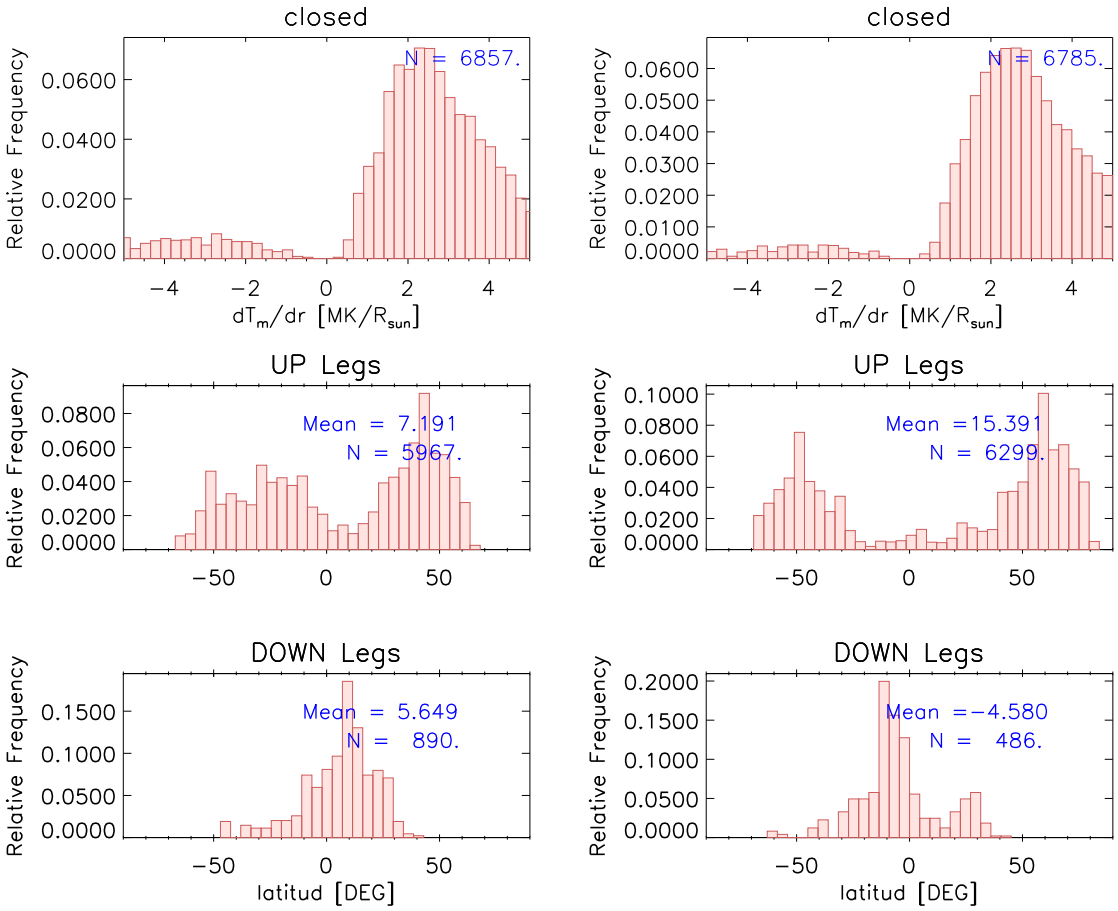

Figure 4.9: Same as Figure 4.7 but for rotation CR-2065 (left) and CR-2106 (right).

well as for large and small ones. We tabulate the total number of legs, indicating the fraction of them that are localized in low latitudes (within the ±30° band) and middle latitudes (outside that band), as well as the total loop length. We also tabulate the average value for all legs of the parameters of the HS fits, namely the base values and scale height of the density (N_0, λ_N) and the pressure (P_0, λ_P). Finally, we tabulate the average value of the fitted temperature gradient $a = dT_m/dr$.

We can quantify now the global distribution of both up and down loops. For all rotations most up and down loops are small. The vast majority of the small down loops (more than 91%) are located within the ±30° latitude range. Also, the percentage of small up loops located outside that latitudes range is greater than 75%

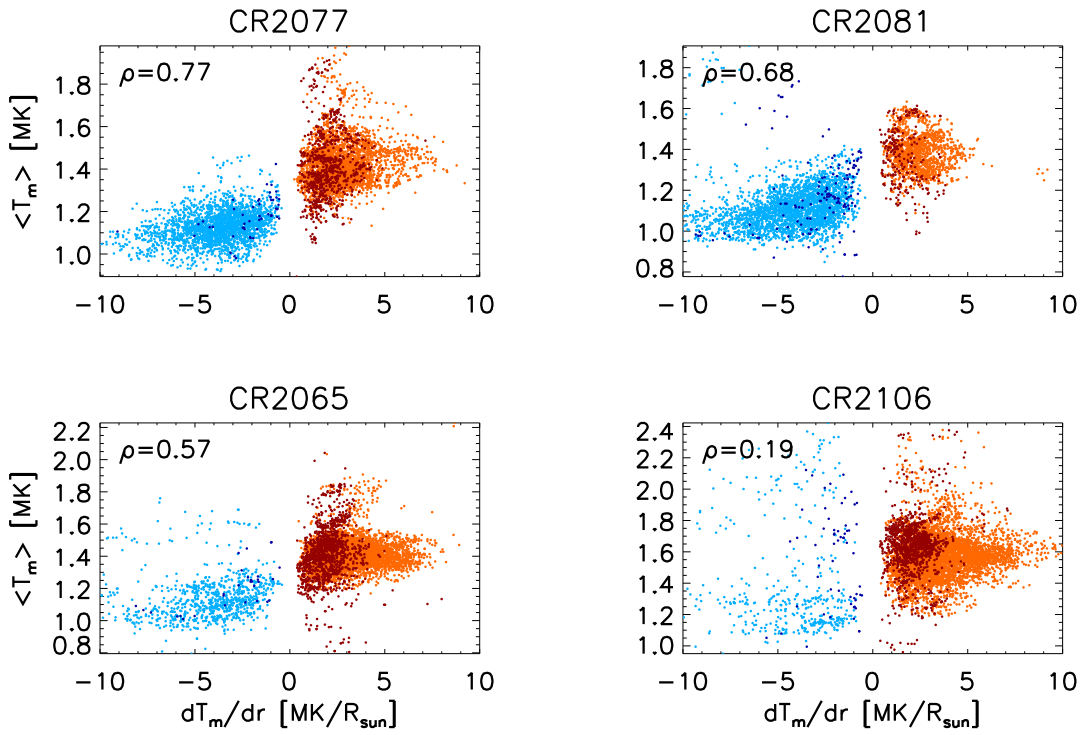

Figure 4.10: Scatter plots of the fitted temperature gradient dT_m/dr versus the average temperature along each leg $\langle T_m \rangle$, for the rotations shown in the Figure 4.6 (top panels), and for the rotations shown in the Figure 4.8 (bottom panels). In each scatter plot the corresponding linear Pearson correlation coefficient of the whole population is indicated. The color code differentiates the four kinds of loops: up small (orange), up large (dark-red), down small (light-blue) and down large (dark-blue).

in three rotations, and than 61% in one case. As for large loops, in general, more than half of their up population lies outside the $\pm 30°$ latitude range, and the vast majority of their down population is within that range (except for CR-2106, for which the number of loops is very low).

We can highlight some differences between the different kind of loops. As the pressure is the product of the density and the temperature, up loops are characterized by $\lambda_P > \lambda_N$, while the opposite happens for down loops, as explained in Chapter II. While the average density scale height of up loops is somewhat larger than that of down ones for all rotations, the difference in the average pressure scale height of the

CR	Leg Type	# of Legs	% of footpoints within $\pm 30^\circ$ latitude	% of footpoints outside $\pm 30^\circ$ latitude	average Loop Length [$R_\odot$]	Average N_0 [10^8 cm^{-3}]	Average P_0 [10^{-3} Pa]	Average λ_N [$R_\odot$]	Average λ_P [$R_\odot$]	Average dT_m/dr [MK/$R_\odot$]
2065	small up	4691	39	61	0.55	2.3	7.1	0.079	0.099	3.21
	small down	858	95	5	0.33	2.6	10.4	0.076	0.059	-4.32
	large up	1276	53	47	1.51	2.2	7.2	0.095	0.114	1.98
	large down	32	91	9	1.23	2.4	9.5	0.076	0.063	-3.26
2077	small up	2990	25	75	0.52	2.2	7.0	0.083	0.103	2.81
	small down	49	76	24	1.55	2.3	8.5	0.077	0.068	-2.04
	large up	795	44	56	1.52	1.9	5.9	0.097	0.119	1.99
	large down	2305	91	9	0.35	2.3	8.7	0.079	0.061	-3.86
2081	small up	1296	22	78	0.53	2.1	6.8	0.081	0.098	2.44
	small down	2802	93	7	0.37	2.4	9.5	0.078	0.059	-4.39
	large up	245	42	58	1.6	1.9	6.0	0.093	0.108	1.64
	large down	143	60	40	1.79	2.4	10.2	0.083	0.069	-2.93
2106	small up	5017	12	88	0.5	2.3	8.2	0.084	0.108	3.65
	small down	426	99	1	0.44	2.5	11.1	0.073	0.058	-4.68
	large up	1282	22	78	1.21	2.2	8.3	0.109	0.136	2.15
	large down	60	35	65	2.02	2.0	4.3	0.094	0.082	-2.1

Table 4.1: Statistics of the number of magnetic loop legs analyzed, their latitudinal distribution, and loop length, discriminating the different types of legs: up, down, small, and large. We also tabulate the average value of several quantities measured along the legs of the magnetic loops: the parameters N_0 and λ_N are the base density and density scale height, respectively; P_0 and λ_P are the base pressure and pressure scale height, respectively; and dT_m/dr is the fitted temperature gradient.

up and down loops is noticeably larger (see Table 4.1). This is a consequence of $P \propto NT$ and the opposite behavior of $T(r)$ for up and down loops. The ratio of the mean pressure scale height of up loops to that of down loops for all rotations ranges between 1.6 and 1.9, for small and large loops, respectively. Figure 4.11 shows scatter plots of the fitted temperature gradient dT_m/dr versus the pressure scale height λ_P, for the same four rotations shown in Figure 4.10. Up loops tend to be characterized by larger pressure scale heights than down loops, as expected due to the increasing temperature with height. For down loops the relationship between the fitted temperature gradient and the pressure scale height is strongly linear, with correlation coefficients of larger than 0.7 for all rotations. This is expected as a larger (but negative) temperature gradient yields a more quickly decreasing pressure and hence a smaller pressure scale height.

The average scale height of large loops is somewhat larger than that of small loops (see Table 4.1). For up loops, the ratio of the mean density scale height λ_N of large loops to that of small ones is 1.20, while the ratio of the respective mean pressure

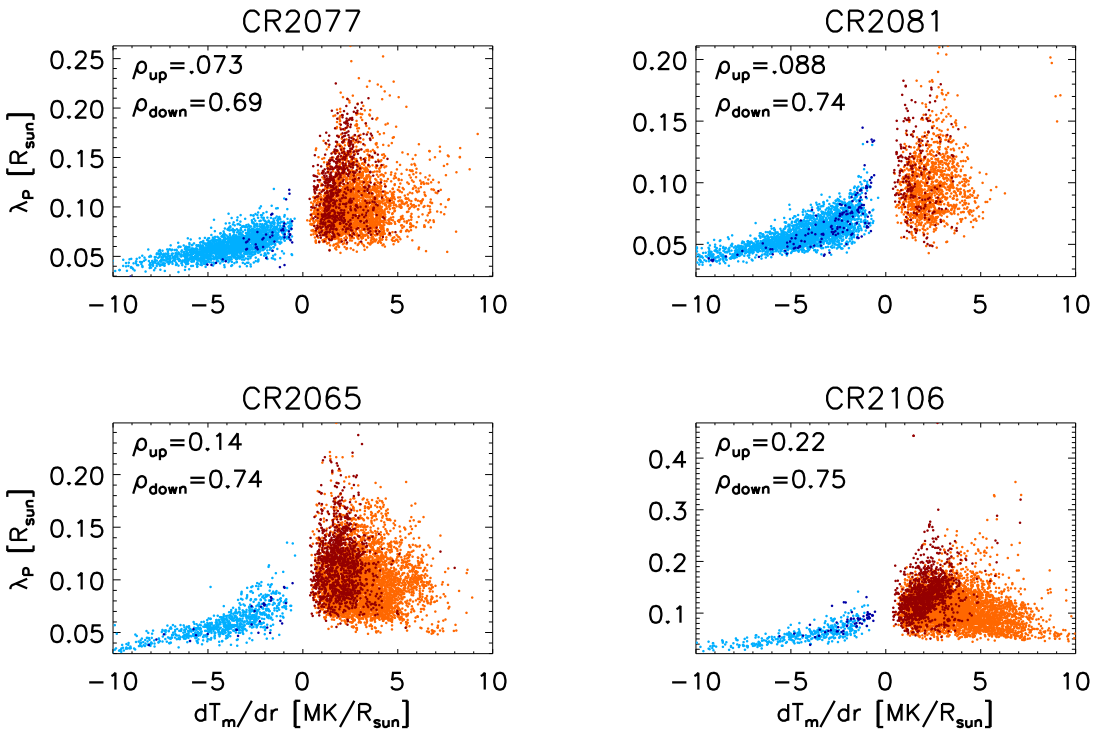

Figure 4.11: Scatter plots of the fitted temperature gradient dT_m/dr versus the pressure scale height λ_P, for the same rotations shown in Figure 4.10, using the same color code to distinguish the different populations of loops. The Pearson correlation coefficient of the up and down population is indicated for each rotation.

scale heights λ_P is 1.17. For down loops, the ratio of the mean density scale height λ_N of large loops to that of small ones is 1.08, while the ratio of the respective mean pressure scale heights λ_P is 1.18. More noticeable differences between large and small loops are to be found in the fitted temperature gradient dT_m/dr, with small loops showing stronger gradients (see Table 4.1). For up loops, the ratio of the mean fitted temperature gradient of small loops to that of large ones is 1.55. For down loops, the ratio of the average fitted temperature gradient of small loops over that of large ones is 1.73. Finally, for the different rotations we analyzed around the solar minimum we did not find a strong variability of the average value of the different fitting parameters.

Figure 4.12 shows scatter plots of the fitted temperature gradient dT_m/dr versus

the average value of the plasma parameter β along each leg ($\langle\beta\rangle$). There is a clear tendency for down loops to have $\beta \gtrsim 1$, while up loops tend to be characterized by $\beta < 1$ values. Similar plots, made at the lowest reliable height of the tomographic grid, 1.035 $R_\odot$, as well as at the apex of the loops, show the same trends. Scatter plots of dT_m/dr versus the average magnetic field strength along each leg $\langle B\rangle$, and versus the average pressure along each leg $\langle P\rangle$ indicate that, while there are no significant differences in the average pressure between up and down loops, the magnetic strength is somewhat bigger for up loops. As $\beta \propto 1/B^2$, the differences of β are mainly due to differences in the magnetic strength, being smaller in down loops.

For the same rotations shown in the Figure 4.10, Table 4.2 summarizes the median and standard deviation of the distribution of the mean plasma parameter $\langle\beta\rangle$, averaged between heights 1.035 and 1.20 $R_\odot$ along each leg. The table also displays the statistics of the distribution of the β value of each leg at 1.035 $R_\odot$. The table discriminates the different type of loops: up, down, small, and large. We focus now on the small loops, which constitute the vast majority of the statistics. For all rotations, the small down loops are characterized by median $\langle\beta\rangle \gtrsim 1$, while up loops show median $\langle\beta\rangle < 1$. The scatter plots in Figure 4.12 and the standard deviations show that the small down and up populations are well differentiated, with virtually all down loops characterized by $\langle\beta\rangle > 1$ and a majority of up loops by $\langle\beta\rangle < 1$. The ratio of the median $\langle\beta\rangle$ of small down loops to that of small up loops ranges between 3 and 5. The β at the lowest height available in our analysis (1.035 $R_\odot$) shows again the trend of larger values for the small down loops, being their median β about twice that of the small up loops. Turning now to large loops, differences are somewhat smaller, but the same trends hold. The ratio of the median $\langle\beta\rangle$ of large down loops to that of large up loops ranges between 1.2 and 2.3, except for CR-2081 which shows similar values of the median $\langle\beta\rangle$.

Figure 4.13 shows Carrington maps of the plasma β at the height 1.075 $R_\odot$, similar

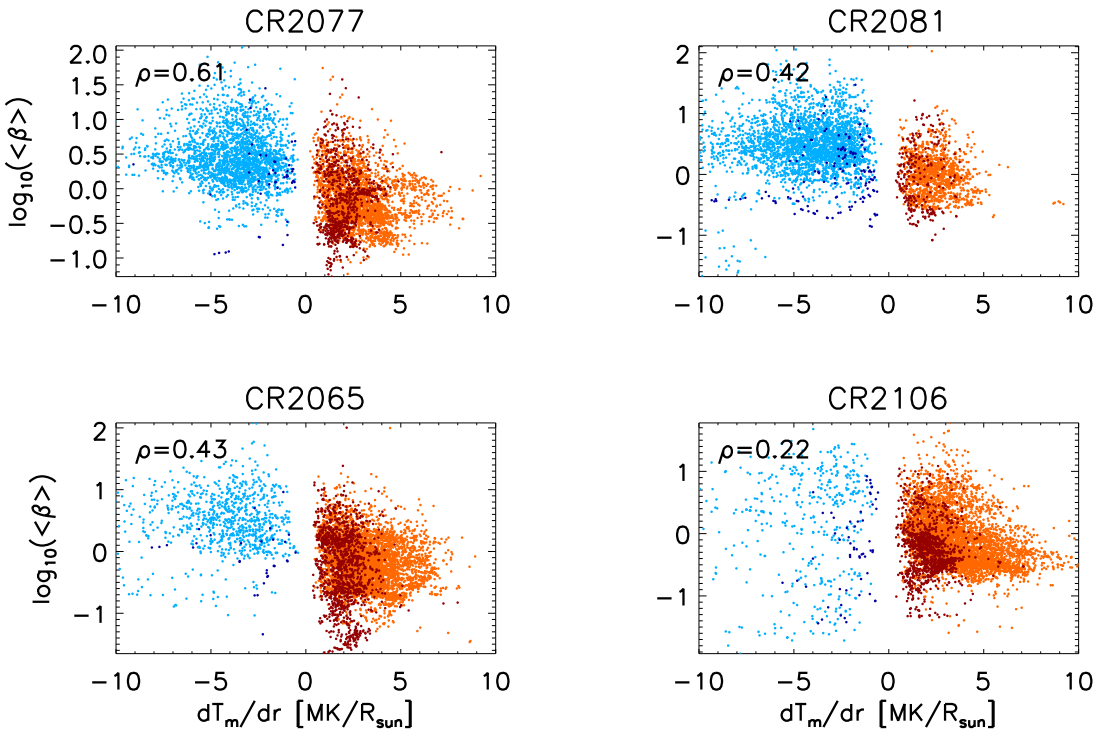

Figure 4.12: Scatter plots of the fitted temperature gradient dT_m/dr versus the mean value $\langle\beta\rangle$ (logarithmic scale), averaged over heights 1.035 thorugh 1.20 $R_\odot$ along each leg, for the same rotations shown in Figure 4.10, using the same colour code to distinguish the different populations of loops.

to those shown for CR-2068 in Figure 7 of *Vásquez et al.* (2011). The color scale and saturation at $\beta = 5$ have been chosen so the $\beta = 1$ level is clearly demarcated by the green/red division. These maps can be visually compared to the up/down location maps in Figures 4.6 and 4.8, showing that the evolution of the high beta region is morphologically consistent with the up/down distribution. The vast majority of down loops is located in the evolving $\beta > 1$ region (red-violet-white), while the up loops are mostly located in the $\beta < 1$ region (green-black).

The total number of up and down loops was computed for each of all eleven CRs. As the latitudinal distribution of up/down loops is similar in all cases, the most noticeable change from one rotation to another one is the relative fraction of up and down loops. Figure 4.14 shows the evolution of the relative fractions of the

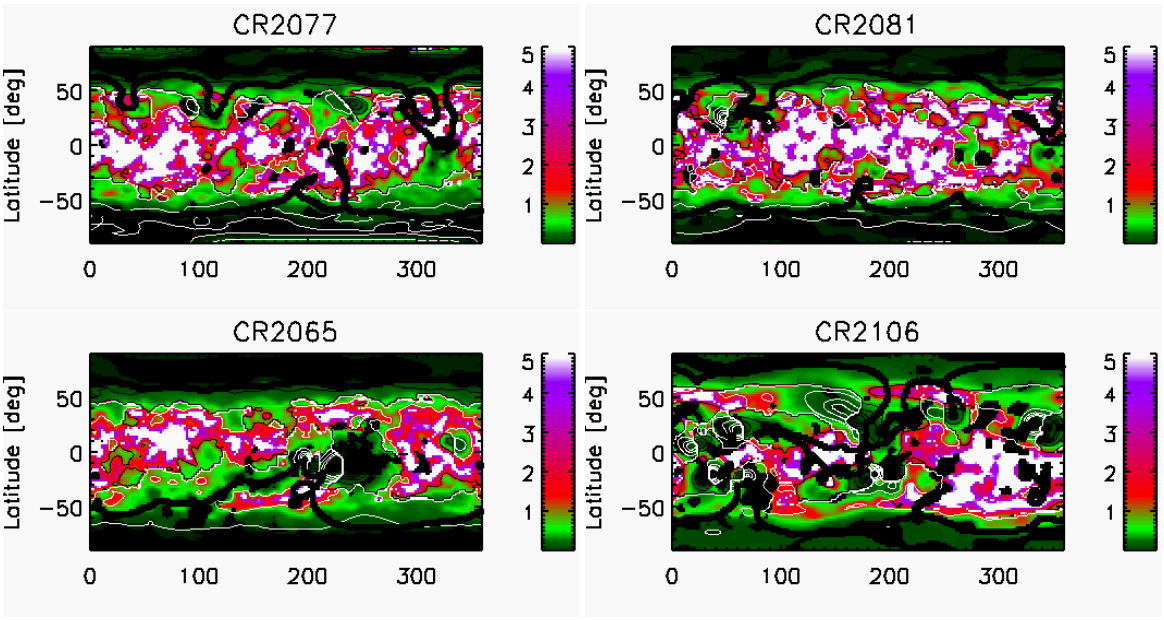

Figure 4.13: Carrington maps of the plasma β at 1.075 $R_\odot$, for the same four rotations selected in Figure 4.12.

CR	Leg Type	Median $\langle\beta\rangle$	Standard Dev. $\langle\beta\rangle$	Median β at 1.035 $R_\odot$	Standard Dev. β at 1.035 $R_\odot$
2065	small up	0.64	1.89	0.41	1.23
	small down	3.18	8.06	0.92	2.93
	large up	0.61	3.26	0.28	1.58
	large down	1.16	1.78	0.71	0.88
2077	small up	0.54	1.90	0.38	1.76
	small down	2.63	6.98	1.06	4.44
	large up	0.67	2.58	0.22	1.78
	large down	1.56	5.24	0.46	0.81
2081	small up	0.94	4.76	0.51	1.18
	small down	2.98	7.06	1.10	3.57
	large up	0.90	2.22	0.29	1.43
	large down	0.90	3.60	0.57	0.89
2106	small up	0.68	2.58	0.41	1.79
	small down	2.34	6.07	0.88	3.37
	large up	0.48	1.31	0.22	0.60
	large down	0.56	2.13	0.07	1.76

Table 4.2: Median and standard deviation of the distribution of the mean plasma parameter $\langle\beta\rangle$, averaged between heights 1.035 and 1.20 $R_\odot$ along each leg, and the β value of each leg at 1.035 $R_\odot$, discriminating their different types: up, down, small, and large, for the same rotations shown in the Figure 4.10.

total number of up loops (orange diamonds) and down loops (light blue diamonds) as a function of Carrington rotation. As an indicator of the global solar activity level, we also overplot the Brussels International Sunspot Number. The blue squares represent the monthly raw data and the red squares represent the monthly smoothed data. Figure 4.14 reveals the most important single result of this chapter: the down loop population maximized at solar minimum and diminished away from it, while the

opposite behaviour is observed for up loops. Most noticeably, the peak of the down loop population occurred during the rotation that exhibited the absolute minimum in the Brussels sunspot number progression, namely CR-2081, which was less than one sunspot during that rotation. This tendency has been quantified by computing linear Pearson correlation coefficient between the down loop fraction and the monthly raw (smoothed) sunspot number, which results in $\rho_1 = -0.55$ (-0.56).

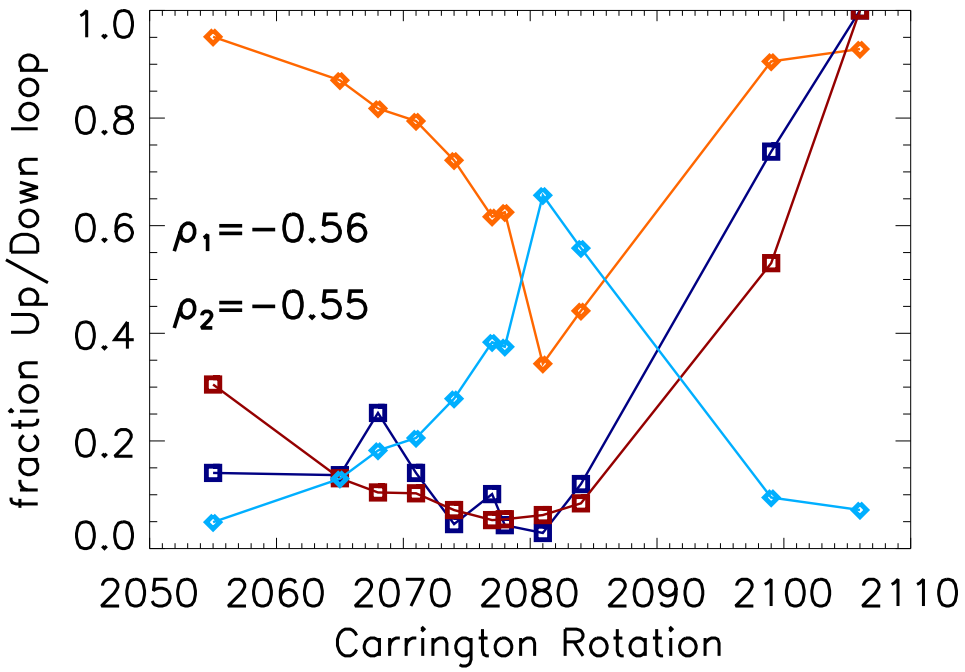

Figure 4.14: Progression of the up and down loop fractions, indicated as orange and light-blue diamonds, respectively. Overplotted, the Brussels International Sunspot Number, both its monthly raw data (dark-blue squares) and its monthly smoothed value (red squares). The sunspot number values have been divided by its maximum value over the analyzed period, so that the peak value "1" corresponds to 33.5 sunspots for the smoothed number and 32.1 sunspots from the raw data. The population of down loops maximizes at CR 2081. The linear Pearson correlation coefficient between the down loop fraction and the smoothed (raw) sunspot number is $\rho_1 = -0.56$ (-0.55).

4.3 Discussion and Conclusions

We performed a statistical study of the temperature structure of the closed field region of the global corona for eleven Carrington rotations around the last minimum of solar activity. We carried on this study using MLDT, which traces the 3D tomographic reconstructions of the coronal electron density and temperature along magnetic field lines of global PFSS models. We selected five rotations during the activity declining phase of the SC-23 before the last solar minimum, three rotations during the deep minimum period, and three rotations during the rising phase of the SC-24. For each rotation we analyzed the thermodynamic properties of the coronal loops by means of the MLDT approach.

We found that down loops are characteristic of the quiet sun during solar minimum. Our major finding is that the down loop fraction is maximized during deep minimum, specifically in CR 2081, coincident with the absolute minimum of the monthly sunspot number. The up loop fraction is minimal at deep minimum and its population increased away from minimum. Down loops are ubiquitous at low latitudes during deep minimum, with more than 91% of their population being located within the latitude range $\pm 30^{\circ}$. Up loops are located at middle latitudes, with more than 75% of their population being outside the latitude range $\pm 30^{\circ}$ for most rotations. The majority of down loops are located in quiet regions, while up loops are located in both quiet as well as in the few active regions that existed during the time period farther from minimum. Complementary, we performed a DEM analysis based on images simultaneously taken by the three EUVI-B bands, verifying the presence of inward temperature gradients at low latitudes and outward ones at mid latitudes, independently of the tomographic results. In this context, the fact that down loops are a characteristic of deep minimum at low latitudes, while they are much less present away from minimum, supports the idea of heating mechanisms being modulated by the evolving coronal magnetic field.

In active regions of the corona the PFSS models used in this work may of course not be accurate, however the conclusions here drawn are robust. In the case of down loops, the vast majority of them are located in quiet sun regions for all the rotations analyzed. Concerning up loops, for the rotations analyzed active regions were very few and compact, having a negligible impact on the results. Rotations CR-2055 and 2065 showed only two significantly large ARs each[4], and those had no impact on the results as virtually no up loops where selected from those regions due to the rejection criteria (Section 4.1.1). Rotation CR-2068 (see *Vásquez et al.* (2011)) showed a more extended complex of three ARs, but very few up loops ended up being selected from those regions, so their impact in results is very minor. For the deep minimum period, rotations CR-2071, 2074, 2077, 2078, 2081 and 2084 showed no or one significantly large AR each, and again virtually no up loops where selected from those. The two last rotations analyzed in this work showed a greater number of significantly large ARs, five in the case of CR-2099, and ten in the case of CR-2106. In both cases the great majority of the loops selected for analysis do not belong to the ARs.

Down loops are likely to be indicative of heating strongly concentrated in their footpoints, at the coronal base. At 1.035 $R_\odot$ (our lowest observed height), we found that the median value of β in the small (apex below 1.2 $R_\odot$) down loops was ≈ 1, while in small up loops it was significantly less than unity (cf. Table 4.2). At larger heights, this difference in β between down and up loops is even greater, as indicated by the value $\langle\beta\rangle$ (averaged along each leg between heights 1.035 and 1.20 $R_\odot$), which is 2 to 3 for small down loops, and significantly below unity for small up loops. For the CRs we analyzed the median value of $\langle\beta\rangle$ for small down loops is 3 to 5 times larger than for small up loops. Differences between large (apex above 1.2 $R_\odot$) down loops and large up loops are less significant, but the statistics of large loops is very poor. Values of $\beta \gtrsim 1$ in the core region of the quiescent streamer belt have been already

[4] `www.solarmonitor.org`

found in previous observational works (*Li et al.*, 1998a; *Kohl et al.*, 1995; *Vásquez et al.*, 2011), as well as modeling efforts (*Suess et al.*, 1996; *Wang et al.*, 1998; *Vásquez et al.*, 2003). The condition $\beta \sim 1$ is optimal for mode conversion between Alfvenic and compressive modes (e.g. slow and fast modes), that can then be damped. In a recent 2.5-dimensional MHD simulations, covering from the photosphere to the interplanetary medium, (*Matsumoto and Suzuki*, 2012) found that shock heating by the dissipation of the slow mode wave plays a fundamental role in the heating of the corona. We speculate then that down loops with $\beta \gtrsim 1$ allow for efficient conversion to compressive modes, so that the damping is enhanced at low heights. In up loops, where β is low, this heat source is not available, and the Alfvén waves propagate to larger heights, where wave reflection and turbulent cascades lead to a more uniform heating.

In a recent observational work based on EIS data, (*Hahn et al.*, 2012) measured the variation of spectral UV line widths in the range of heights from 1.05 to $1.4R_\odot$ over a polar coronal hole. They separated the non-thermal component of the line width, which is expected to be proportional to the Alfvén wave amplitude (*Hassler et al.*, 1990; *Banerjee et al.*, 1998). They found that, starting at heights as low as $1.1R_\odot$, the non-thermal component decreases with height in a way that deviates from the predicted dependence for undamped waves (*Moran*, 2001). Their observations indicate then that Alfvén waves are being damped at surprisingly low heights in the polar coronal hole. The mechanism responsible for those observations may also be operating at low latitudes in the closed magnetic fields. In view of our results, future work will include the exploration of the presence of such evidence in EIS data scans of low latitude regions during the last minimum.

There is extensive evidence of the ubiquitous presence of Alfvén waves in the Sun, starting at chromospheric levels (*Jess et al.*, 2009) and the transition region (*McIntosh et al.*, 2011), up to coronal heights (*Tomczyk et al.*, 2007; *Tomczyk and McIntosh*,

2009; *Jess et al.*, 2012), and the heliosphere (*Belcher and Davis*, 1971). A primary dissipation mechanism of Alfvén waves is that of collisions, with typical damping scale lengths $\gtrsim 1\mathrm{R}_\odot$ (*Cranmer*, 2002). Alternative wave damping mechanisms can operate at much smaller scales, such as phase mixing, turbulent cascade, and resonant abortion in inhomogeneous plasmas (*Heyvaerts and Priest*, 1983; *Matthaeus et al.*, 1999; *Goossens et al.*, 2011; *Dong and Paty*, 2011). Observational evidence for wave damping at low heights has been recently found by *Hahn et al.* (2012). They studied optically thin spectral lines observed by the Extreme Ultraviolet Imaging Spectrometer (EIS) on board *Hinode* in coronal holes. They measured the amplitude of the non-thermal line broadening of the lines, thought to be proportional to that of the Alfvén waves (*Banerjee et al.*, 1998; *Doyle et al.*, 1998; *Moran*, 2001; *Banerjee et al.*, 2009). They found that amplitude to exhibit downward gradients in height, between 1.1 and 1.3 $\mathrm{R}_\odot$, providing strong evidence of Alfvén wave damping occurring in that range of heights. Recent observational results based on Hinode (*De Pontieu et al.*, 2007) indicate that the power carried by chromospheric Alfvén waves is even larger than previously thought, and that only a fraction of them would suffice to provide the energy requirements for the coronal heating and the acceleration of the solar wind.

Wave-driven global coronal models contain two key parameters that govern the behavior of the heating term, namely the Alfvén wave dissipation length and its reflection coefficient. The dissipation length can be inferred from observations, such as those by *Hahn et al.* (2012). The Alfvén wave reflection coefficient is rather uncertain. In the context of a global coronal model, Huang et al. (2013) treat the reflection coefficient as a free parameter. They show that for large enough reflection coefficients near the Sun, a fully 3D solar corona model can reproduce the up and down loops observed in the solar corona.

In view of our finding of down loops and their characteristic $\beta \gtrsim 1$ values, we propose the following physical picture for the quiet Sun heating. In the $\beta >> 1$

photosphere, Alfvén waves are created from 3-5 minute oscillations and chromospheric shocks (*Matsumoto and Suzuki*, 2012). Along loops for which $\beta < 1$, which we found to be up loops, Alfvén waves are damped by reflection and turbulent cascade, thus heating is not isolated to the bottoms of the loops. Along loops for which $\beta \gtrsim 1$, which we found to be down loops, the Alfvén waves can be efficiently converted to compressive modes, which are quickly damped at the transition region due to the high sound speed gradient and thermal conduction. This puts the majority of the heating at the coronal base. In this scenario, the heating of both up and down loops finds their energy source in exactly the same Alfvén waves with origins in the photosphere. Depending on the value of β in the low corona, these waves are then dissipated through different mechanisms, but the total amount of Alfvén wave energy available is about the same, leading to similar temperatures in both types of loops, as observed in the MLDT results. This picture naturally explains why the quiet Sun plasma appears as diffuse emission, not allowing individual loops to be seen, as the proposed processes occurs in a fairly homogeneous fashion. This speculative scenario will be further investigated through extended MLDT analysis and MHD modeling (Huang et al., 2013).

CHAPTER V

Conclusions and Future Work

The coronal heating problem is one of the greatest challenges in solar physics. Traditionally, the study of the coronal heating problem has moved into two different directions: the solar wind (open magnetic field lines) and coronal loops (closed magnetic field lines) in active regions. Quiet Sun loops have not been rigorously studied before. This dissertation has attempted to fill this gap by studying quiet Sun loops, and our investigations show important results that advance our understanding of the coronal heating problem.

5.1 Conclusions

In Chapter II, we develop a new technique called Michigan Loop Diagnostic Technique (MLDT) to study quiet Sun loops. The essence of MLDT is to combine Differential Emission Measure Tomography (DEMT) with a potential field source surface (PFSS) model of the solar coronal magnetic field. The application of MLDT in Carrington Rotation (CR) 2077, which is at the last solar minimum, discovered a new class of loop, "down" loops (the temperature decreases with height along a loop) as well as the regular "up" loops (the temperature increases with height along a loop). "Up" loops are expected, as they are a solution of all coronal loop models, while "down" loops are a surprise. "Down" loops have not been observed before and are

considered to be unstable. We followed the discussions in *Aschwanden and Schrijver* (2002) and inferred that "down" loops are due to footpoint heating, where the loop is mostly heated near the footpoints. Furthermore, "down" loops are found to be localized in low latitude regions ($< \pm 30°$ latitude). The spatial distribution of "down" loops implies the spatial distribution of the coronal heating: footpoint heating occurs in low latitudes and more uniform heating in high latitudes.

"Down" loops receive arguments that they are unstable due to thermal instabilities. We perform magnetohydrodynamic (MHD) simulations to investigate the thermal stability in Chapter III. The model we use is one of the most sophisticated solar corona models, the Alfvén Wave Solar Model (AWSoM), which is a magnetogram-driven 3D, global model with an inner boundary in the upper chromosphere. We first generate "down" loops in the simulation, then impose pressure perturbations near the apex. If "down" loops are unstable, thermal instabilities will develop and destroy the loop. Our simulation results show that the perturbed "down" loop returns to its initial state within three hours, which supported the thermodynamic stability of "down" loops against small pressure perturbations.

Chapter IV discusses more "down" loop properties. We extend the "down" loop study to 11 solar rotations, from CR 2055 to CR 2106, covering the descending phase of the solar cycle 23 and the ascending phase of the solar cycle 24. We find two more important properties of "down" loops:

1. "Down" loops are anti-correlated with sunspot number. The sunspot number is an indicator of the activity level of the Sun: a large sunspot number means the Sun is active. This property suggests that it will be difficult to find "down" loops in active regions or on an active Sun.

2. "Down" loops are associated with plasma beta (β) larger than unity. The plasma beta property of "down" loops is closely related to the coronal heating problem. We argue that "down" loops with $\beta > 1$ favor footpoint heating. As

discussed in Chapter IV, Alfvén waves are a candidate to explain the coronal heating. In a loop with $\beta > 1$, we speculate that Alfvén waves efficiently convert to compressive modes in low altitudes, where the damping (energy dissipation) is enhanced; with $\beta < 1$, Alfvén waves cannot efficiently convert to compressive modes, so they propagate to larger height; they are damped by wave reflections and turbulent cascades along the loop, leading to a more uniform heating.

Overall, this dissertation reveals a new feature of the quiet Sun corona during solar minimum: "down" loops and their spatial distribution. By addressing the thermal stability of "down" loops, we believe that "down" loops exist in the quiet Sun corona even though they have not been directly observed before. We propose that "down" loops indicate footpoint heating (heating is enhanced near the footpoints). The spatial distribution of "down" loops indicate that loops in low latitudes prefer footpoint heating while loops in high latitudes are heated more uniformly. We have not discussed any details about the physical mechanisms which lead to footpoint heating in this dissertation. Further investigates of the physical mechanisms underlying how "down" loops are heated at low heights will shed light on the coronal heating problem.

5.2 Future Work

Some possible future work related to "down" loops is listed as follows:

1. Use Differential Emission Measure (DEM) to carry out time-dependent study of the inward temperature gradient shown in Figure 2.8 and Figure 4.3. This sort of study would reveal the "down" loops evolution within a solar rotation and may provide new properties of "down" loops.

2. Study "down" loops in some small regions, like streamer or pseudo streamer regions. This study would show whether "down" loops have preferential distri-

bution between streamers and pseudostreamers. This study would advance the understanding of differences between streamer and pseudo streamer.

3. The connection of "down" loops to high plasma beta, as found in Chapter IV, suggested a coronal loop study by means of compressible MHD turbulence. One can perform simulations of closed loop in a similar fashion to *Matsumoto and Suzuki* (2012), who studied the coronal heating on open field lines. For closed loop, we can straighten the loop in a 2-D Cartesian simulation. The imposed boundary conditions on both footpoints are the Alfvén fluctuations. Such simulations will naturally include the mode conversion from Alfvén waves to slow magneto-acoustic as well as turbulence cascades of Alfvén waves. The proposed study could reveal how various loop geometries affect the Alfvén wave dissipation via turbulence cascades in closed magnetic loops. This kind of study have never been investigated before. If the proposed study can generate "down" loops, the small-scale heating mechanism behind "down" loops will be more clear.

APPENDICES

APPENDIX A

Robustness to Calibration Uncertainty

The EUVI channels have common, absolute radiometric uncertainty of about 30%. This uncertainty corresponds to a common scale factor in all of the EUVI channels' effective areas. In addition, there is a relative uncertainty in each channel's effective area of about 15%. This latter uncertainty corresponds to a different unknown number for each channel. The effect of the former uncertainty is not consequential for this analysis, as the estimated density is only sensitive to the square-root of the estimated intensity. However, the $\sim 15\%$ relative error is not easily dismissed, since the DEM diagnostics are sensitive to the ratios of the channel intensities.

In order to test the robustness of our results to the independent errors, we performed an "error box" analysis. The error box is defined as the range of calibration constants for the 3 EUVI channels.[1] We take the sides of this error box to be the $\pm 15\%$ uncertainty of the various channels. Thus, one face of the error box is obtained by multiplying the 171 channel effective area by 1.15 and the opposite face of the box is obtained by multiplying the 171 channel effective area by 0.85. The other four faces of the box are similarly obtained for the 195 and 284 channels. One corner of the box is obtained by multiplying all three band effective areas by 1.15, and the opposite

[1] The early mission data allows the STEREO-A/171 and STEREO-B/171 to be scaled so that they have effectively the same radiometric calibration. The same applies to the other wavelengths.

corner is obtained by dividing all of the effective areas by 1.15. We will call these two configurations "HHH" and "LLL," which stands for "high, high, high" and "low, low, low." For the reasons described above, the HHH and LLL are not interesting because they correspond to a uniform rescaling of all effective areas. However, these six configurations have consequences for the derived temperatures: HHL, HLH, LHH, LLH, LHL and HLL. In this section, we show results for these configurations and demonstrate that our main results do not change. Table A.1 is similar to Table 2.1 except that is has the values for the six configurations as well as the "base" configuration (which corresponds to center of the error box), whose values are also shown in Table 2.1. The mean, μ, and standard deviation divided by the mean, σ/μ for all 7 cases is shown in each box of the table. The variations within the boxes of the table are small, and do not alter the conclusions of this article.

Figure A.1 is similar to Figure 2.2, except that it shows how the spatial distribution of the up and down loops differs according to the location in the error box. While some differences can be noted, none of these changes exhibit obvious systematic trends, so the overall pattern does not change. Figure A.2 is similar to Figure 2.8, but instead it shows the results from the corners of the error boxes. While the derived temperature change, the gradient directions do not, so all corners of the error box show consistency with the up/down loop interpretation.

	levels	# of loop legs	% of footpoints within $\pm 30^\circ$ latitude	% of footpoints outside $\pm 30^\circ$ latitude	average Loop Length [$R_\odot$]	average N_0 [10^8 cm^{-3}]	average P_0 [10^{-3} Pa]	average λ_N [$R_\odot$]	average λ_P [$R_\odot$]	average $\partial T_m/\partial r$ [MK/$R_\odot$]
Small Up Legs	base	4155	20	80	0.5	2.2	7.1	0.082	0.101	2.89
	LLH	3896	19	81	0.5	2.1	6.9	0.081	0.103	3.29
	LHL	4004	19	81	0.5	2.1	7.5	0.084	0.097	2.07
	LHH	4038	19	81	0.5	2.2	7.8	0.084	0.099	2.33
	HLL	4318	22	78	0.5	2.2	6.5	0.079	0.101	3.28
	HLH	3875	21	79	0.5	2.3	6.6	0.078	0.106	4.00
	HHL	4295	20	80	0.5	2.3	7.5	0.082	0.098	2.43
	μ	4083.0	20.0	80.0	0.5	2.2	7.1	0.081	0.101	2.90
	$\sigma/\lvert\mu\rvert$ (%)	4.4	5.8	1.4	0.0	3.7	6.9	2.823	3.072	23.32
Large Up Legs	base	1255	42	58	1.5	1.9	6.2	0.095	0.114	1.73
	LLH	1146	42	58	1.4	1.8	6.0	0.097	0.118	1.98
	LHL	1156	40	60	1.4	1.8	6.5	0.099	0.112	1.28
	LHH	1149	41	59	1.4	1.9	6.8	0.099	0.114	1.42
	HLL	1519	44	56	1.6	1.9	5.6	0.092	0.112	1.90
	HLH	1312	43	57	1.5	2.0	5.8	0.091	0.118	2.37
	HHL	1275	41	59	1.5	2.0	6.5	0.096	0.111	1.45
	μ	1258.9	41.9	58.1	1.5	1.9	6.2	0.096	0.114	1.73
	$\sigma/\lvert\mu\rvert$ (%)	10.6	3.2	2.3	3.9	4.3	6.9	3.301	2.500	22.07
Small Down Legs	base	2585	97	3	0.4	2.3	8.6	0.082	0.064	-3.70
	LLH	2658	96	4	0.4	2.2	8.7	0.083	0.062	-4.46
	LHL	2663	96	4	0.4	2.2	8.8	0.079	0.066	-2.96
	LHH	2734	96	4	0.4	2.3	9.4	0.080	0.064	-3.57
	HLL	1864	97	3	0.3	2.3	7.5	0.083	0.068	-2.37
	HLH	2411	97	3	0.4	2.3	8.1	0.085	0.062	-3.85
	HHL	2334	97	3	0.4	2.4	8.7	0.080	0.067	-2.58
	μ	2464.1	96.6	3.4	0.4	2.3	8.5	0.082	0.065	-3.36
	$\sigma/\lvert\mu\rvert$ (%)	12.2	0.6	15.6	2.2	3.0	7.0	2.617	3.647	22.29
Large Down Legs	base	57	86	14	1.3	2.2	8.2	0.082	0.071	-1.87
	LLH	104	83	17	1.5	2.1	8.2	0.083	0.069	-2.52
	LHL	118	85	15	1.3	2.1	8.4	0.080	0.072	-1.67
	LHH	119	81	19	1.5	2.2	9.1	0.081	0.071	-2.08
	HLL	8	75	25	1.4	2.0	6.3	0.083	0.076	-0.92
	HLH	31	81	19	1.4	2.1	7.1	0.085	0.072	-1.89
	HHL	87	82	18	1.3	2.3	8.4	0.081	0.073	-1.37
	μ	74.9	81.9	18.1	1.4	2.1	8.0	0.082	0.072	-1.76
	$\sigma/\lvert\mu\rvert$ (%)	58.5	4.4	19.7	7.3	4.6	11.8	2.041	3.000	29.11

Table A.1: Statistical Quantities of Small/Large up/Down Loops. N_0 and λ_N are the base density and density scale height, respectively, and P_0 and λ_P are the base pressure and pressure scale height, respectively [see Equations (2.2) and (2.4)]. In each box the average over the seven levels listed above is given by μ.

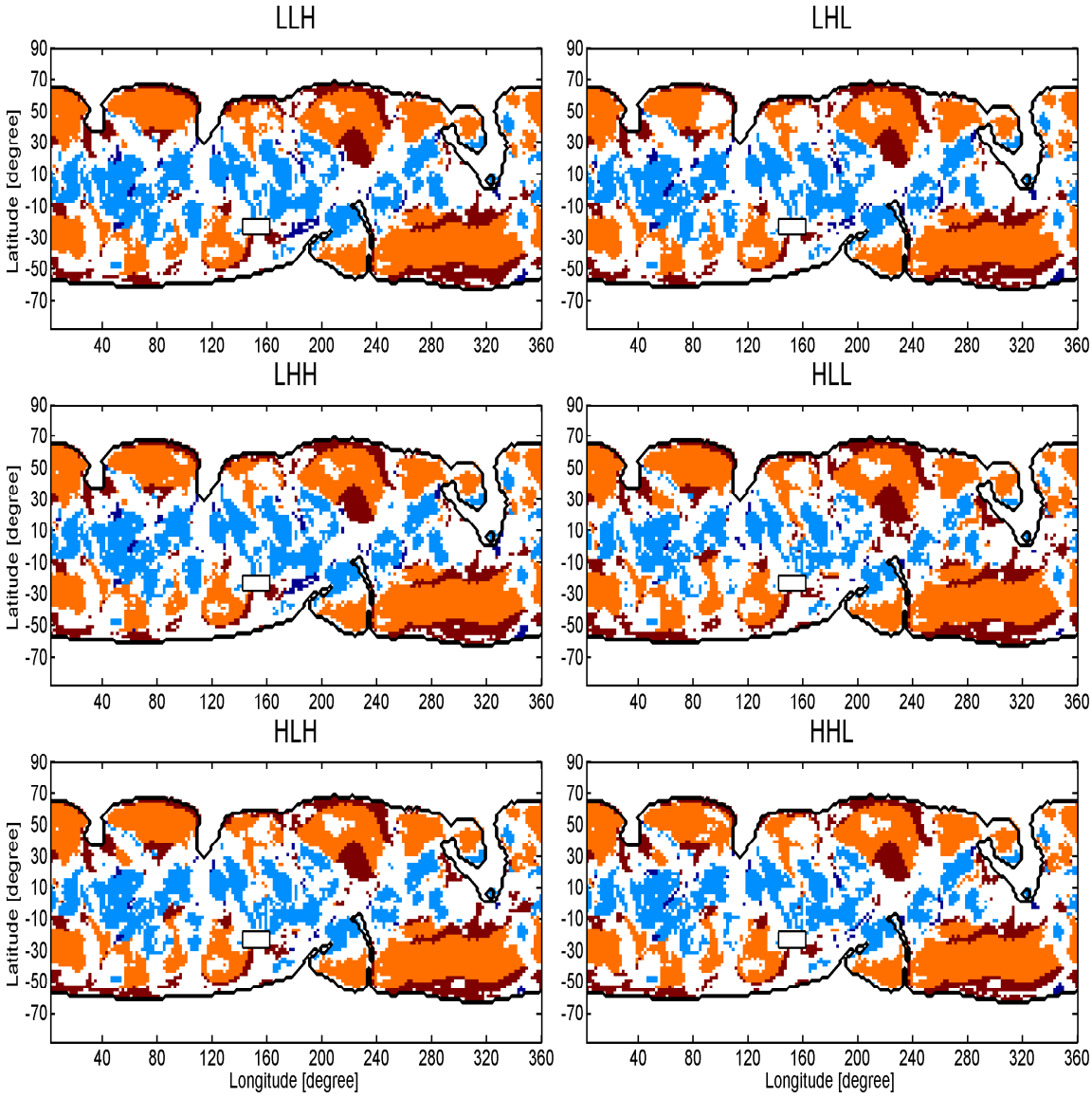

Figure A.1: Similar to Figure 2.2, except each image represents one corner of the error box, as indicated. Notice that the spatial distribution of the up and down loops changes very little.

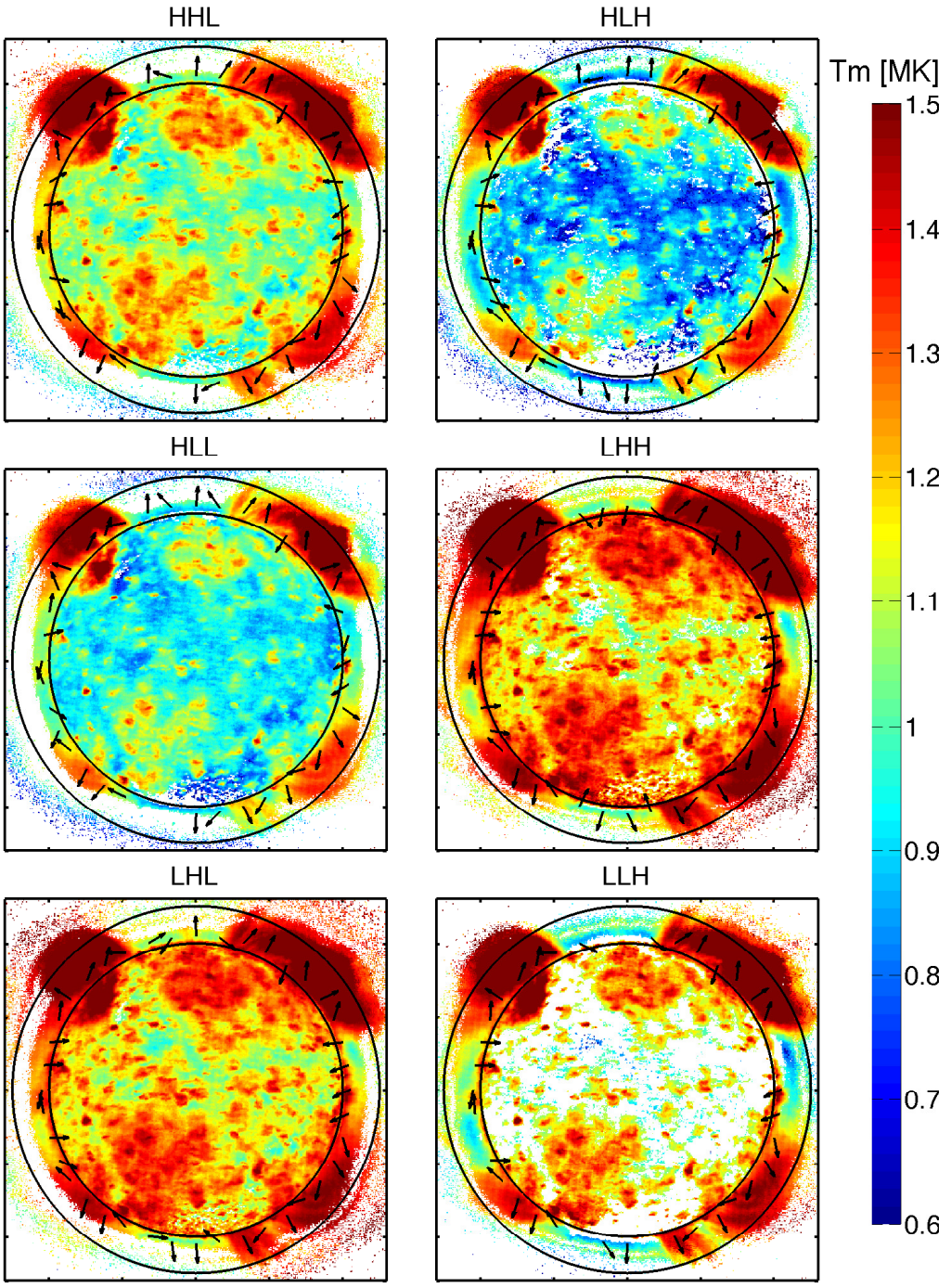

Figure A.2: Similar to Figure 2.8, except each image represents one corner of the error box, as indicated. Notice that the spatial distribution of the gradient arrows changes very little.

BIBLIOGRAPHY

BIBLIOGRAPHY

Akinari, N. (2007), Morphological Study of Quiescent Streamers during Solar Minimum by Ultraviolet Emission Lines, *ApJ*, *668*, 1196–1209, doi:10.1086/521386.

Alexander, C. E., et al. (2013), Anti-parallel EUV Flows Observed along Active Region Filament Threads with Hi-C, *ApJ*, *775*, L32, doi:10.1088/2041-8205/775/1/L32.

Antiochos, S. K. (1979), The stability of solar coronal loops, *ApJ*, *232*, L125–L129, doi:10.1086/183049.

Antiochos, S. K., Z. Mikić, V. S. Titov, R. Lionello, and J. A. Linker (2011), A Model for the Sources of the Slow Solar Wind, *ApJ*, *731*, 112, doi:10.1088/0004-637X/731/2/112.

Aschwanden, M. J. (2004), *Physics of the Solar Corona. An Introduction*, Praxis Publishing Ltd.

Aschwanden, M. J., and P. Boerner (2011), Solar Corona Loop Studies with the Atmospheric Imaging Assembly. I. Cross-sectional Temperature Structure, *ApJ*, *732*, 81, doi:10.1088/0004-637X/732/2/81.

Aschwanden, M. J., and C. J. Schrijver (2002), Analytical Approximations to Hydrostatic Solutions and Scaling Laws of Coronal Loops, *ApJS*, *142*, 269–283, doi:10.1086/341945.

Aschwanden, M. J., and D. Tsiklauri (2009), The Hydrodynamic Evolution of Impulsively Heated Coronal Loops: Explicit Analytical Approximations, *ApJS*, *185*, 171–185, doi:10.1088/0067-0049/185/1/171.

Aschwanden, M. J., N. V. Nitta, J.-P. Wuelser, and J. R. Lemen (2008), First 3D Reconstructions of Coronal Loops with the STEREO A+B Spacecraft. II. Electron Density and Temperature Measurements, *ApJ*, *680*, 1477–1495, doi:10.1086/588014.

Aschwanden, M. J., P. Boerner, C. J. Schrijver, and A. Malanushenko (2011), Automated Temperature and Emission Measure Analysis of Coronal Loops and Active Regions Observed with the Atmospheric Imaging Assembly on the Solar Dynamics Observatory (SDO/AIA), *Sol. Phys.*, p. 384, doi:10.1007/s11207-011-9876-5.

Banerjee, D., L. Teriaca, J. G. Doyle, and K. Wilhelm (1998), Broadening of SI VIII lines observed in the solar polar coronal holes, *A&A*, *339*, 208–214.

Banerjee, D., D. Pérez-Suárez, and J. G. Doyle (2009), Signatures of Alfvén waves in the polar coronal holes as seen by EIS/Hinode, *A&A*, *501*, L15–L18, doi:10.1051/0004-6361/200912242.

Barbey, N., C. Guennou, and F. Auchère (2011), TomograPy: A Fast, Instrument-Independent, Solar Tomography Software, *Sol. Phys.*, p. 181, doi:10.1007/s11207-011-9792-8.

Bastian, T. S., M. W. Ewell, Jr., and H. Zirin (1993), A Study of Solar Prominences near lambda = 1 Millimeter, *ApJ*, *418*, 510, doi:10.1086/173413.

Belcher, J. W., and L. Davis, Jr. (1971), Large-amplitude Alfvén waves in the interplanetary medium, 2, *J. Geophys. Res.*, *76*, 3534, doi:10.1029/JA076i016p03534.

Bernasconi, P. N., D. M. Rust, and D. Hakim (2005), Advanced Automated Solar Filament Detection And Characterization Code: Description, Performance, And Results, *Sol. Phys.*, *228*, 97–117, doi:10.1007/s11207-005-2766-y.

Bommier, V., J. L. Leroy, and S. Sahal-Brechot (1986), The Linear Polarization of Hydrogen H-Beta Radiation and the Joint Diagnostic of Magnetic Field Vector and Electron Density in Quiescent Prominences - Part Two - the Electron Density, *A&A*, *156*, 90.

Bommier, V., E. Landi Degl'Innocenti, J.-L. Leroy, and S. Sahal-Brechot (1994), Complete determination of the magnetic field vector and of the electron density in 14 prominences from linear polarization measurements in the HeI D3 and H-alpha lines, *Sol. Phys.*, *154*, 231–260, doi:10.1007/BF00681098.

Borrini, G., J. M. Wilcox, J. T. Gosling, S. J. Bame, and W. C. Feldman (1981), Solar wind helium and hydrogen structure near the heliospheric current sheet - A signal of coronal streamers at 1 AU, *J. Geophys. Res.*, *86*, 4565–4573, doi:10.1029/JA086iA06p04565.

Burlaga, L. F., N. F. Ness, M. H. Acuña, R. P. Lepping, J. E. P. Connerney, E. C. Stone, and F. B. McDonald (2005), Crossing the Termination Shock into the Heliosheath: Magnetic Fields, *Science*, *309*, 2027–2029, doi:10.1126/science.1117542.

Butala, M. D., R. J. Hewett, R. A. Frazin, and F. Kamalabadi (2010), Dynamic Three-Dimensional Tomography of the Solar Corona, *Sol. Phys.*, *262*, 495–509, doi:10.1007/s11207-010-9536-1.

Cargill, P. J. (1994), Some implications of the nanoflare concept, *ApJ*, *422*, 381–393, doi:10.1086/173733.

Cargill, P. J., and S. J. Bradshaw (2013), The Cooling of Coronal Plasmas. IV. Catastrophic Cooling of Loops, *ApJ*, *772*, 40, doi:10.1088/0004-637X/772/1/40.

Cargill, P. J., and E. R. Priest (1980), Siphon flows in coronal loops. I - Adiabatic flow, *Sol. Phys.*, *65*, 251–269, doi:10.1007/BF00152793.

Cargill, P. J., S. J. Bradshaw, and J. A. Klimchuk (2012), Enthalpy-based Thermal Evolution of Loops. II. Improvements to the Model, *ApJ*, *752*, 161, doi:10.1088/0004-637X/752/2/161.

Carlsson, M., and R. F. Stein (1997), Formation of Solar Calcium H and K Bright Grains, *ApJ*, *481*, 500–514.

Chae, J. (2003), The Formation of a Prominence in NOAA Active Region 8668. II. Trace Observations of Jets and Eruptions Associated with Canceling Magnetic Features, *ApJ*, *584*, 1084–1094, doi:10.1086/345739.

Chae, J. (2007), Measurements of magnetic helicity injected through the solar photosphere, *Advances in Space Research*, *39*, 1700–1705, doi:10.1016/j.asr.2007.01.035.

Chae, J. (2010), Dynamics of Vertical Threads and Descending Knots in a Hedgerow Prominence, *ApJ*, *714*, 618–629, doi:10.1088/0004-637X/714/1/618.

Chandran, B. D. G., E. Quataert, G. G. Howes, J. V. Hollweg, and W. Dorland (2009), The Turbulent Heating Rate in Strong Magnetohydrodynamic Turbulence with Nonzero Cross Helicity, *ApJ*, *701*, 652–657, doi:10.1088/0004-637X/701/1/652.

Chandran, B. D. G., T. J. Dennis, E. Quataert, and S. D. Bale (2011), Incorporating Kinetic Physics into a Two-fluid Solar-wind Model with Temperature Anisotropy and Low-frequency Alfvén-wave Turbulence, *ApJ*, *743*, 197, doi:10.1088/0004-637X/743/2/197.

Chandrasekhar, S. (1961), *Hydrodynamic and hydromagnetic stability*.

Cheng, C.-C., E. S. Oran, G. A. Doschek, J. P. Boris, and J. T. Mariska (1983), Numerical simulations of loops heated to solar flare temperatures. I, *ApJ*, *265*, 1090–1119, doi:10.1086/160751.

Cirtain, J. W., et al. (2013), Energy release in the solar corona from spatially resolved magnetic braids, *Nature*, *493*, 501–503, doi:10.1038/nature11772.

Coleman, P. J., Jr. (1968), Turbulence, Viscosity, and Dissipation in the Solar-Wind Plasma, *ApJ*, *153*, 371, doi:10.1086/149674.

Craig, I. J. D., and J. C. Brown (1976), Fundamental limitations of X-ray spectra as diagnostics of plasma temperature structure, *A&A*, *49*, 239–250.

Craig, I. J. D., and A. N. McClymont (1976), Mass motions in a heated flare filament, *Sol. Phys.*, *50*, 133–151, doi:10.1007/BF00206198.

Craig, I. J. D., A. N. McClymont, and J. H. Underwood (1978), The Temperature and Density Structure of Active Region Coronal Loops, *A&A*, *70*, 1.

Cranmer, S. R. (2002), Coronal Holes and the High-Speed Solar Wind, *Space Sci. Rev.*, *101*, 229–294.

Cranmer, S. R. (2009), Coronal Holes, *Living Reviews in Solar Physics*, *6*, 3.

Cranmer, S. R., A. A. van Ballegooijen, and R. J. Edgar (2007), Self-consistent Coronal Heating and Solar Wind Acceleration from Anisotropic Magnetohydrodynamic Turbulence, *ApJS*, *171*, 520–551, doi:10.1086/518001.

De Pontieu, B., et al. (2007), Chromospheric Alfvénic Waves Strong Enough to Power the Solar Wind, *Science*, *318*, 1574–, doi:10.1126/science.1151747.

Del Zanna, G., F. Chiuderi Drago, and S. Parenti (2004), Soho cds and sumer observations of quiescent filaments and their interpretation, *Astron. Astrophys.*, *420*, 307–317, doi:10.1051/0004-6361:20034267.

Dere, K. P., E. Landi, H. E. Mason, B. C. Monsignori Fossi, and P. R. Young (1997), CHIANTI - an atomic database for emission lines, *A&AS*, *125*, 149–173, doi:10.1051/aas:1997368.

Dere, K. P., E. Landi, P. R. Young, G. Del Zanna, M. Landini, and H. E. Mason (2009), CHIANTI - an atomic database for emission lines. IX. Ionization rates, recombination rates, ionization equilibria for the elements hydrogen through zinc and updated atomic data, *A&A*, *498*, 915–929, doi:10.1051/0004-6361/200911712.

Dmitruk, P., L. J. Milano, and W. H. Matthaeus (2001), Wave-driven Turbulent Coronal Heating in Open Field Line Regions: Nonlinear Phenomenological Model, *ApJ*, *548*, 482–491, doi:10.1086/318685.

Dong, C., and C. S. Paty (2011), Heating of ions by low-frequency Alfvén waves in partially ionized plasmas, *Physics of Plasmas*, *18*(3), 030,702, doi:10.1063/1.3555532.

Doyle, J. G., D. Banerjee, and M. E. Perez (1998), Coronal line-width variations, *Sol. Phys.*, *181*, 91–101, doi:10.1023/A:1005019931323.

Engvold, O. (1976), The fine structure of prominences. I - Observations - H-alpha filtergrams, *Sol. Phys.*, *49*, 283–295, doi:10.1007/BF00162453.

Engvold, O., T. Hirayama, J. L. Leroy, E. R. Priest, and E. Tandberg-Hanssen (1990), Hvar Reference Atmosphere of Quiescent Prominences, in *IAU Colloq. 117: Dynamics of Quiescent Prominences*, *Lecture Notes in Physics, Berlin Springer Verlag*, vol. 363, edited by V. Ruzdjak and E. Tandberg-Hanssen, p. 294, doi:10.1007/BFb0025709.

Feldman, U., and E. Landi (2008), The temperature structure of solar coronal plasmas, *Physics of Plasmas*, *15*(5), 056,501, doi:10.1063/1.2837044.

Feldman, U., U. Schühle, K. G. Widing, and J. M. Laming (1998), Coronal Composition above the Solar Equator and the North Pole as Determined from Spectra Acquired by the SUMER Instrument on SOHO, *ApJ*, *505*, 999–1006, doi:10.1086/306195.

Feldman, U., G. A. Doschek, U. Schühle, and K. Wilhelm (1999), Properties of Quiet-Sun Coronal Plasmas at Distances of $1.03 \leq R_{\odot} \leq 1.50$ along the Solar Equatorial Plane, *ApJ*, *518*, 500–507, doi:10.1086/307252.

Feldman, U., E. Landi, and N. A. Schwadron (2005), On the sources of fast and slow solar wind, *Journal of Geophysical Research (Space Physics)*, *110*, A07109, doi:10.1029/2004JA010918.

Field, G. B. (1965), Thermal Instability., *ApJ*, *142*, 531, doi:10.1086/148317.

Fisher, G. H., R. C. Canfield, and A. N. McClymont (1985a), Flare Loop Radiative Hydrodynamics - Part Seven - Dynamics of the Thick Target Heated Chromosphere, *ApJ*, *289*, 434, doi:10.1086/162903.

Fisher, G. H., R. C. Canfield, and A. N. McClymont (1985b), Flare Loop Radiative Hydrodynamics - Part Six - Chromospheric Evaporation due to Heating by Nonthermal Electrons, *ApJ*, *289*, 425, doi:10.1086/162902.

Fisher, G. H., R. C. Canfield, and A. N. McClymont (1985c), Flare loop radiative hydrodynamics. V - Response to thick-target heating. VI - Chromospheric evaporation due to heating by nonthermal electrons. VII - Dynamics of the thick-target heated chromosphere, *ApJ*, *289*, 414–441, doi:10.1086/162901.

Fisk, L. A. (2003), Acceleration of the solar wind as a result of the reconnection of open magnetic flux with coronal loops, *Journal of Geophysical Research (Space Physics)*, *108*, 1157, doi:10.1029/2002JA009284.

Fisk, L. A., and L. Zhao (2009), The heliospheric magnetic field and the solar wind during the solar cycle, in *IAU Symposium*, *IAU Symposium*, vol. 257, edited by N. Gopalswamy and D. F. Webb, pp. 109–120, doi:10.1017/S1743921309029160.

Fisk, L. A., T. H. Zurbuchen, and N. A. Schwadron (1999), Coronal Hole Boundaries and their Interactions with Adjacent Regions, *Space Sci. Rev.*, *87*, 43–54, doi:10.1023/A:1005153730158.

Frazin, R. A., and P. Janzen (2002), Tomography of the Solar Corona. II. Robust, Regularized, Positive Estimation of the Three-dimensional Electron Density Distribution from LASCO-C2 Polarized White-Light Images, *ApJ*, *570*, 408–422, doi:10.1086/339572.

Frazin, R. A., F. Kamalabadi, and M. A. Weber (2005), On the Combination of Differential Emission Measure Analysis and Rotational Tomography for Three-dimensional Solar EUV Imaging, *ApJ*, *628*, 1070–1080, doi:10.1086/431295.

Frazin, R. A., A. M. Vásquez, and F. Kamalabadi (2009), Quantitative, Three-dimensional Analysis of the Global Corona with Multi-spacecraft Differential Emission Measure Tomography, *ApJ*, *701*, 547–560, doi:10.1088/0004-637X/701/1/547.

Fuller, J., and S. E. Gibson (2009), A survey of coronal cavity density profiles, *Astrophys. J.*, *700*, 1205–1215, doi:10.1088/0004-637X/700/2/1205.

Fuller, J., S. E. Gibson, G. de Toma, and Y. Fan (2008), Observing the Unobservable? Modeling Coronal Cavity Densities, *ApJ*, *678*, 515–530, doi:10.1086/533527.

Gary, G. A., E. A. West, D. Rees, J. A. McKay, M. Zukic, and P. Herman (2007), Solar CIV vacuum-ultraviolet Fabry-Perot interferometers, *A&A*, *461*, 707–722, doi:10.1051/0004-6361:20066035.

Gibson, S. E., A. Fludra, F. Bagenal, D. Biesecker, G. del Zanna, and B. Bromage (1999), Solar minimum streamer densities and temperatures using Whole Sun Month coordinated data sets, *J. Geophys. Res.*, *104*, 9691–9700, doi:10.1029/98JA02681.

Gibson, S. E., D. Foster, J. Burkepile, G. de Toma, and A. Stanger (2006), The Calm before the Storm: The Link between Quiescent Cavities and Coronal Mass Ejections, *ApJ*, *641*, 590–605, doi:10.1086/500446.

Gibson, S. E., et al. (2010), Three-dimensional Morphology of a Coronal Prominence Cavity, *ApJ*, *724*, 1133–1146, doi:10.1088/0004-637X/724/2/1133.

Gilbert, H. R., T. E. Holzer, J. T. Burkepile, and A. J. Hundhausen (2000), Active and Eruptive Prominences and Their Relationship to Coronal Mass Ejections, *ApJ*, *537*, 503–515, doi:10.1086/309030.

Gombosi, T. I. (Ed.) (1998), *Physics of the space environment*.

Gontikakis, C., I. Contopoulos, and H. C. Dara (2008), Distribution of coronal heating in a solar active region, *A&A*, *489*, 441–447, doi:10.1051/0004-6361:20079086.

Goossens, M., R. Erdélyi, and M. S. Ruderman (2011), Resonant MHD Waves in the Solar Atmosphere, *Space Sci. Rev.*, *158*, 289–338, doi:10.1007/s11214-010-9702-7.

Groth, C. P. T., D. L. De Zeeuw, T. I. Gombosi, and K. G. Powell (2000), Global three-dimensional MHD simulation of a space weather event: CME formation, interplanetary propagation, and interaction with the magnetosphere, *J. Geophys. Res.*, *105*, 25,053–25,078, doi:10.1029/2000JA900093.

Grotrian, W. (1939), Zur Frage der Deutung der Linien im Spektrum der Sonnenkorona, *Naturwissenschaften*, *27*, 214–214, doi:10.1007/BF01488890.

Guhathakurta, M., and R. R. Fisher (1995), Coronal streamers and fine scale structures of the low latitude corona as detected with Spartan 201-01 White Light Coronagraph, *Geophys. Res. Lett.*, *22*, 1841–1844, doi:10.1029/95GL01603.

Guhathakurta, M., G. J. Rottman, R. R. Fisher, F. Q. Orrall, and R. C. Altrock (1992), Coronal density and temperature structure from coordinated observations associated with the total solar eclipse of 1988 March 18, *ApJ*, *388*, 633–643, doi:10.1086/171180.

Habbal, S. R., and R. Rosner (1979), Thermal instabilities in magnetically confined plasmas - Solar coronal loops, *ApJ*, *234*, 1113–1121, doi:10.1086/157595.

Hahn, M., E. Landi, and D. W. Savin (2012), Evidence of Wave Damping at Low Heights in a Polar Coronal Hole, *ApJ*, *753*, 36, doi:10.1088/0004-637X/753/1/36.

Harris, E. G. (1962), Rayleigh-Taylor Instabilities of a Collapsing Cylindrical Shell in a Magnetic Field, *Physics of Fluids*, *5*, 1057–1062, doi:10.1063/1.1724473.

Hassler, D. M., G. J. Rottman, E. C. Shoub, and T. E. Holzer (1990), Line broadening of MG X 609 and 625 A coronal emission lines observed above the solar limb, *ApJ*, *348*, L77–L80, doi:10.1086/185635.

He, J.-S., C.-Y. Tu, H. Tian, and E. Marsch (2010), Solar wind origins in coronal holes and in the quiet Sun, *Advances in Space Research*, *45*, 303–309, doi:10.1016/j.asr.2009.07.020.

Heyvaerts, J., and E. R. Priest (1983), Coronal heating by phase-mixed shear Alfven waves, *A&A*, *117*, 220–234.

Hirayama, T. (1971), Spectral Analysis of Four Quiescent Prominences Observed at the Peruvian Eclipse, *Sol. Phys.*, *17*, 50–75, doi:10.1007/BF00152861.

Hirayama, T. (1986), The density and thickness of quiescent prominences, in *NASA Conference Publication*, *NASA Conference Publication*, vol. 2442, edited by A. I. Poland, pp. 149–153.

Hollweg, J. V. (1986), Transition region, corona, and solar wind in coronal holes, *J. Geophys. Res.*, *91*, 4111–4125, doi:10.1029/JA091iA04p04111.

Howard, R. A., et al. (2008), Sun Earth Connection Coronal and Heliospheric Investigation (SECCHI), *Space Sci. Rev.*, *136*, 67–115, doi:10.1007/s11214-008-9341-4.

Huang, Z., R. A. Frazin, E. Landi, W. B. Manchester, A. M. Vásquez, and T. I. Gombosi (2012), Newly Discovered Global Temperature Structures in the Quiet Sun at Solar Minimum, *ApJ*, *755*, 86, doi:10.1088/0004-637X/755/2/86.

Hundhausen, A. J. (1972), *Coronal Expansion and Solar Wind*.

Isenberg, P. A. (1990), Investigations of a turbulence-driven solar wind model, *J. Geophys. Res.*, *95*, 6437–6442, doi:10.1029/JA095iA05p06437.

Jess, D. B., M. Mathioudakis, R. Erdélyi, P. J. Crockett, F. P. Keenan, and D. J. Christian (2009), Alfvén Waves in the Lower Solar Atmosphere, *Science*, *323*, 1582–, doi:10.1126/science.1168680.

Jess, D. B., S. Shelyag, M. Mathioudakis, P. H. Keys, D. J. Christian, and F. P. Keenan (2012), Propagating Wave Phenomena Detected in Observations and Simulations of the Lower Solar Atmosphere, *ApJ*, *746*, 183, doi:10.1088/0004-637X/746/2/183.

Kano, R., and S. Tsuneta (1995), Scaling Law of Solar Coronal Loops Obtained with YOHKOH, *ApJ*, *454*, 934, doi:10.1086/176547.

Katsukawa, Y., and S. Tsuneta (2001), Small Fluctuation of Coronal X-Ray Intensity and a Signature of Nanoflares, *ApJ*, *557*, 343–350, doi:10.1086/321636.

Klimchuk, J. A. (2006), On Solving the Coronal Heating Problem, *Sol. Phys.*, *234*, 41–77, doi:10.1007/s11207-006-0055-z.

Klimchuk, J. A., S. K. Antiochos, and J. T. Mariska (1987), A numerical study of the nonlinear thermal stability of solar loops, *ApJ*, *320*, 409–417, doi:10.1086/165554.

Klimchuk, J. A., S. Patsourakos, and P. J. Cargill (2008), Highly Efficient Modeling of Dynamic Coronal Loops, *ApJ*, *682*, 1351–1362, doi:10.1086/589426.

Kohl, J. L., et al. (1995), The Ultraviolet Coronagraph Spectrometer for the Solar and Heliospheric Observatory, *Sol. Phys.*, *162*, 313–356, doi:10.1007/BF00733433.

Koutchmy, S. (1988), Space-borne coronagraphy, *Space Sci. Rev.*, *47*, 95–143, doi:10.1007/BF00223238.

Koutchmy, S., and M. Livshits (1992), Coronal Streamers, *Space Sci. Rev.*, *61*, 393–417, doi:10.1007/BF00222313.

Koutchmy, S., V. A. Koutvitsky, M. M. Molodensky, L. S. Solov'iev, and O. Koutchmy (1994), Magnetic configuration of coronal streamers and threads, *Space Sci. Rev.*, *70*, 283–288, doi:10.1007/BF00777881.

Krishna Prasad, S., J. Singh, and K. Ichimoto (2013), Thermal Structure of Coronal Loops as Seen with Norikura Coronagraph, *ApJ*, *765*, L46, doi:10.1088/2041-8205/765/2/L46.

Kruskal, M., and M. Schwarzschild (1954), Some Instabilities of a Completely Ionized Plasma, *Royal Society of London Proceedings Series A*, *223*, 348–360, doi:10.1098/rspa.1954.0120.

Kucera, T. A., and E. Landi (2006), Ultraviolet Observations of Prominence Activation and Cool Loop Dynamics, *ApJ*, *645*, 1525–1536, doi:10.1086/504398.

Kucera, T. A., S. E. Gibson, D. J. Schmit, E. Landi, and D. Tripathi (2012), Temperature and Extreme-ultraviolet Intensity in a Coronal Prominence Cavity and Streamer, *ApJ*, *757*, 73, doi:10.1088/0004-637X/757/1/73.

Labrosse, N., P. Heinzel, J.-C. Vial, T. Kucera, S. Parenti, S. Gunár, B. Schmieder, and G. Kilper (2010), Physics of Solar Prominences: I —Spectral Diagnostics and Non-LTE Modelling, *Space Sci. Rev.*, *151*, 243–332, doi:10.1007/s11214-010-9630-6.

Landi, E., and P. Testa (2014), The Temperature of Quiescent Streamers during Solar Cycles 23 and 24, *ApJ*, *787*, 33, doi:10.1088/0004-637X/787/1/33.

Landi, E., U. Feldman, and K. P. Dere (2002), CHIANTI-An Atomic Database for Emission Lines. V. Comparison with an Isothermal Spectrum Observed with SUMER, *ApJS*, *139*, 281–296, doi:10.1086/337949.

Landi, E., U. Feldman, and G. A. Doschek (2006), Plasma Diagnostics of the Large-Scale Corona with SUMER. I. Measurements at the West Limb, *ApJ*, *643*, 1258–1270, doi:10.1086/503247.

Landi, E., G. Del Zanna, P. R. Young, K. P. Dere, and H. E. Mason (2012), CHIANTI—An Atomic Database for Emission Lines. XII. Version 7 of the Database, *ApJ*, *744*, 99, doi:10.1088/0004-637X/744/2/99.

Landi, E., P. R. Young, K. P. Dere, G. Del Zanna, and H. E. Mason (2013), CHIANTI—An Atomic Database for Emission Lines. XIII. Soft X-Ray Improvements and Other Changes, *ApJ*, *763*, 86, doi:10.1088/0004-637X/763/2/86.

Landman, D. A. (1986), Physical conditions in the cool parts of prominences and spicules - The effects of model atom level truncation on the derived plasma parameters, *ApJ*, *305*, 546–552, doi:10.1086/164267.

Lau, Y. Y., J. C. Zier, I. M. Rittersdorf, M. R. Weis, and R. M. Gilgenbach (2011), Anisotropy and feedthrough in magneto-Rayleigh-Taylor instability, *Phys. Rev. E*, *83*(6), 066405, doi:10.1103/PhysRevE.83.066405.

Li, J., J. C. Raymond, L. W. Acton, J. L. Kohl, M. Romoli, G. Noci, and G. Naletto (1998a), Physical Structure of a Coronal Streamer in the Closed-Field Region as Observed from UVCS/SOHO and SXT/Yohkoh, *ApJ*, *506*, 431–438, doi:10.1086/306244.

Li, K., B. Schmieder, J.-M. Malherbe, T. Roudier, and J.-E. Wiik (1998b), Physical properties of the quiescent prominence of 5June 1996, from Hα observations, *Sol. Phys.*, *183*, 323–338, doi:10.1023/A:1005060613653.

Li, X., S. R. Habbal, J. V. Hollweg, and R. Esser (1999), Heating and cooling of protons by turbulence-driven ion cyclotron waves in the fast solar wind, *J. Geophys. Res.*, *104*, 2521–2536, doi:10.1029/1998JA900126.

Lin, Y., O. Engvold, L. Rouppe van der Voort, J. E. Wiik, and T. E. Berger (2005), Thin Threads of Solar Filaments, *Sol. Phys.*, *226*, 239–254, doi:10.1007/s11207-005-6876-3.

Low, B. C. (1996), Solar Activity and the Corona, *Sol. Phys.*, *167*, 217–265, doi: 10.1007/BF00146338.

Mackay, D. H., J. T. Karpen, J. L. Ballester, B. Schmieder, and G. Aulanier (2010), Physics of Solar Prominences: II—Magnetic Structure and Dynamics, *Space Sci. Rev.*, *151*, 333–399, doi:10.1007/s11214-010-9628-0.

Mariska, J. T. (1980), Relative chemical abundances in different solar regions, *ApJ*, *235*, 268–273, doi:10.1086/157630.

Mariska, J. T., G. A. Doschek, and U. Feldman (1979), Extreme-ultraviolet limb spectra of a prominence observed from SKYLAB, *ApJ*, *232*, 929–939, doi:10.1086/157356.

Matsumoto, T., and T. K. Suzuki (2012), Connecting the Sun and the Solar Wind: The First 2.5-dimensional Self-consistent MHD Simulation under the Alfvén Wave Scenario, *ApJ*, *749*, 8, doi:10.1088/0004-637X/749/1/8.

Matthaeus, W. H., G. P. Zank, S. Oughton, D. J. Mullan, and P. Dmitruk (1999), Coronal Heating by Magnetohydrodynamic Turbulence Driven by Reflected Low-Frequency Waves, *ApJ*, *523*, L93–L96, doi:10.1086/312259.

McComas, D. J., et al. (2009), IBEX—Interstellar Boundary Explorer, *Space Sci. Rev.*, *146*, 11–33, doi:10.1007/s11214-009-9499-4.

McIntosh, S. W., B. de Pontieu, M. Carlsson, V. Hansteen, P. Boerner, and M. Goossens (2011), Alfvénic waves with sufficient energy to power the quiet solar corona and fast solar wind, *Nature*, *475*, 477–480, doi:10.1038/nature10235.

Moran, T. G. (2001), Interpretation of coronal off-limb spectral line width measurements, *A&A*, *374*, L9–L11, doi:10.1051/0004-6361:20010643.

Nagai, F. (1980), A model of hot loops associated with solar flares. I - Gasdynamics in the loops, *Sol. Phys.*, *68*, 351–379, doi:10.1007/BF00156874.

Narain, U., and P. Ulmschneider (1990), Chromospheric and coronal heating mechanisms, *Space Sci. Rev.*, *54*, 377–445, doi:10.1007/BF00177801.

Narain, U., and P. Ulmschneider (1996), Chromospheric and Coronal Heating Mechanisms II, *Space Sci. Rev.*, *75*, 453–509, doi:10.1007/BF00833341.

Neugebauer, M., and C. W. Snyder (1966), Mariner 2 Observations of the Solar Wind, 1, Average Properties, *J. Geophys. Res.*, *71*, 4469.

Noci, G. (1981), Siphon flows in the solar corona, *Sol. Phys.*, *69*, 63–76, doi:10.1007/BF00151256.

Noci, G., et al. (1997), The quiescent corona and slow solar wind, in *Fifth SOHO Workshop: The Corona and Solar Wind Near Minimum Activity*, *ESA Special Publication*, vol. 404, edited by A. Wilson, p. 75.

Noyes, R. W., A. K. Dupree, M. C. E. Huber, W. H. Parkinson, E. M. Reeves, and G. L. Withbroe (1972), Extreme-Ultraviolet Emission from Solar Prominences, *ApJ*, *178*, 515–526, doi:10.1086/151812.

Nuevo, F. A., A. M. Vásquez, R. A. Frazin, Z. Huang, and W. B. Manchester (2012), The 3D solar corona Cycle 24 rising phase from SDO/AIA tomography, in *IAU Symposium*, *IAU Symposium*, vol. 286, edited by C. H. Mandrini and D. F. Webb, pp. 238–241, doi:10.1017/S1743921312004905.

Nuevo, F. A., Z. Huang, R. Frazin, i. Ward B. Manchester, M. Jin, and A. M. Vsquez (2013), Evolution of the global temperature structure of the solar corona during the minimum between solar cycles 23 and 24, *ApJ*, *773*(1), 9.

Ofman, L. (2000), Source regions of the slow solar wind in coronal streamers, *Geophys. Res. Lett.*, *27*, 2885–2888, doi:10.1029/2000GL000097.

Ofman, L. (2009), Three-Dimensional Magnetohydrodynamic Models of Twisted Multithreaded Coronal Loop Oscillations, *ApJ*, *694*, 502–511, doi:10.1088/0004-637X/694/1/502.

Ofman, L., T. A. Kucera, Z. Mouradian, and A. I. Poland (1998), SUMER Observations of the Evolution and the Disappearance of a Solar Prominence, *Sol. Phys.*, *183*, 97–106, doi:10.1023/A:1005052923972.

Ofman, L., L. Abbo, and S. Giordano (2011), Multi-fluid Model of a Streamer at Solar Minimum and Comparison with Observations, *ApJ*, *734*, 30, doi:10.1088/0004-637X/734/1/30.

Oliver, R. (2009), Prominence Seismology Using Small Amplitude Oscillations, *Space Sci. Rev.*, *149*, 175–197, doi:10.1007/s11214-009-9527-4.

O'Neill, I., and X. Li (2005), Coronal loops heated by turbulence-driven Alfvén waves: A two fluid model, *A&A*, *435*, 1159–1167, doi:10.1051/0004-6361:20041596.

Oran, E. S., J. T. Mariska, and J. P. Boris (1982), The condensational instability in the solar transition region and corona, *ApJ*, *254*, 349–360, doi:10.1086/159739.

Oran, R., B. van der Holst, E. Landi, M. Jin, I. V. Sokolov, and T. I. Gombosi (2013), A Global Wave-driven Magnetohydrodynamic Solar Model with a Unified Treatment of Open and Closed Magnetic Field Topologies, *ApJ*, *778*, 176, doi:10.1088/0004-637X/778/2/176.

Orlando, S., G. Peres, and S. Serio (1995a), Models of stationary siphon flows in stratified, thermally conducting coronal loops. II. Shocked solutions., *A&A*, *300*, 549.

Orlando, S., G. Peres, and S. Serio (1995b), Models of stationary siphon flows in stratified, thermally conducting coronal loops. 1: Regular solutions, *A&A*, *294*, 861–873.

Orrall, F. Q., and E. J. Schmahl (1976), The prominence-corona interface compared with the chromosphere-corona transition region, *Sol. Phys.*, *50*, 365–381, doi:10.1007/BF00155299.

Osterbrock, D. E. (1961), The Heating of the Solar Chromosphere, Plages, and Corona by Magnetohydrodynamic Waves., *ApJ*, *134*, 347, doi:10.1086/147165.

Parenti, S. (2014), Solar Prominences: Observations, *Living Reviews in Solar Physics*, *11*, 1, doi:10.12942/lrsp-2014-1.

Parenti, S., and J.-C. Vial (2007), Prominence and quiet-Sun plasma parameters derived from FUV spectral emission, *A&A*, *469*, 1109–1115, doi:10.1051/0004-6361:20077196.

Parenti, S., B. J. I. Bromage, G. Poletto, G. Noci, and G. E. Raymond, J. C.and Bromage (2000), Characteristics of solar coronal streamers. Element abundance, temperature and density from coordinated CDS and UVCS SOHO observations, *A&A*, *363*, 800–814.

Parker, E. N. (1958), Dynamics of the Interplanetary Gas and Magnetic Fields., *ApJ*, *128*, 664, doi:10.1086/146579.

Parker, E. N. (1988), Nanoflares and the solar X-ray corona, *ApJ*, *330*, 474–479, doi:10.1086/166485.

Pasachoff, J. M., V. Rušin, M. Saniga, H. Druckmüllerová, and B. A. Babcock (2011), Structure and Dynamics of the 2009 July 22 Eclipse White-light Corona, *ApJ*, *742*, 29, doi:10.1088/0004-637X/742/1/29.

Patsourakos, S., and J. A. Klimchuk (2005), Coronal Loop Heating by Nanoflares: The Impact of the Field-aligned Distribution of the Heating on Loop Observations, *ApJ*, *628*, 1023–1030, doi:10.1086/430662.

Patsourakos, S., and J. A. Klimchuk (2006), Nonthermal Spectral Line Broadening and the Nanoflare Model, *ApJ*, *647*, 1452–1465, doi:10.1086/505517.

Peres, G., S. Serio, G. S. Vaiana, and R. Rosner (1982), Coronal closed structures. IV - Hydrodynamical stability and response to heating perturbations, *ApJ*, *252*, 791–799, doi:10.1086/159601.

Porter, L. J., and J. A. Klimchuk (1995), Soft X-Ray Loops and Coronal Heating, *ApJ*, *454*, 499, doi:10.1086/176501.

Powell, K. G., P. L. Roe, T. J. Linde, T. I. Gombosi, and D. L. de Zeeuw (1999), A Solution-Adaptive Upwind Scheme for Ideal Magnetohydrodynamics, *Journal of Computational Physics*, *154*, 284–309, doi:10.1006/jcph.1999.6299.

Raymond, J. C., et al. (1997), Composition of Coronal Streamers from the SOHO Ultraviolet Coronagraph Spectrometer, *Sol. Phys.*, *175*, 645–665, doi:10.1023/A:1004948423169.

Reale, F. (2010), Coronal loops: Observations and modeling of confined plasma, *Living Reviews in Solar Physics*, *7*(5), doi:10.12942/lrsp-2010-5.

Reale, F., G. Nigro, F. Malara, G. Peres, and P. Veltri (2005), Modeling a Coronal Loop Heated by Magnetohydrodynamic Turbulence Nanoflares, *ApJ*, *633*, 489–498, doi:10.1086/444409.

Reale, F., M. Guarrasi, P. Testa, E. E. DeLuca, G. Peres, and L. Golub (2011), Solar Dynamics Observatory Discovers Thin High Temperature Strands in Coronal Active Regions, *ApJ*, *736*, L16, doi:10.1088/2041-8205/736/1/L16.

Rosner, R., W. H. Tucker, and G. S. Vaiana (1978), Dynamics of the quiescent solar corona, *ApJ*, *220*, 643–645, doi:10.1086/155949.

Schatzman, E. (1949), The heating of the solar corona and chromosphere, *Annales d'Astrophysique*, *12*, 203.

Schrijver, C. J. (2001), Catastrophic cooling and high-speed downflow in quiescent solar coronal loops observed with TRACE, *Sol. Phys.*, *198*, 325–345, doi:10.1023/A:1005211925515.

Schrijver, C. J., and A. M. Title (2003), The Magnetic Connection between the Solar Photosphere and the Corona, *ApJ*, *597*, L165–L168, doi:10.1086/379870.

Schrijver, C. J., G. H. J. van den Oord, and R. Mewe (1994), The optical thickness of stellar coronae in EUV lines, *A&A*, *289*, L23–L26.

Schrijver, C. J., A. M. Title, A. A. van Ballegooijen, H. J. Hagenaar, and R. A. Shine (1997), Sustaining the Quiet Photospheric Network: The Balance of Flux Emergence, Fragmentation, Merging, and Cancellation, *ApJ*, *487*, 424, doi:10.1086/304581.

Schrijver, C. J., A. W. Sandman, M. J. Aschwanden, and M. L. De Rosa (2004), The Coronal Heating Mechanism as Identified by Full-Sun Visualizations, *ApJ*, *615*, 512–525, doi:10.1086/424028.

Schwadron, N. A., and D. J. McComas (2003), Solar Wind Scaling Law, *ApJ*, *599*, 1395–1403, doi:10.1086/379541.

Serio, S., G. Peres, G. S. Vaiana, L. Golub, and R. Rosner (1981), Closed coronal structures. II - Generalized hydrostatic model, *ApJ*, *243*, 288–300, doi:10.1086/158597.

Shearer, P., R. A. Frazin, A. O. Hero, III, and A. C. Gilbert (2012), The First Stray Light Corrected Extreme-ultraviolet Images of Solar Coronal Holes, *ApJ*, *749*, L8, doi:10.1088/2041-8205/749/1/L8.

Sinars, D. B., et al. (2010), Measurements of Magneto-Rayleigh-Taylor Instability Growth during the Implosion of Initially Solid Al Tubes Driven by the 20-MA, 100-ns Z Facility, *Physical Review Letters*, *105*(18), 185001, doi:10.1103/PhysRevLett.105.185001.

Sokolov, I. V., B. van der Holst, R. Oran, C. Downs, I. I. Roussev, M. Jin, W. B. Manchester, IV, R. M. Evans, and T. I. Gombosi (2013), Magnetohydrodynamic Waves and Coronal Heating: Unifying Empirical and MHD Turbulence Models, *ApJ*, *764*, 23, doi:10.1088/0004-637X/764/1/23.

St. Cyr, O. C., and D. F. Webb (1991), Activity associated with coronal mass ejections at solar minimum - SMM observations from 1984-1986, *Sol. Phys.*, *136*, 379–394, doi:10.1007/BF00146543.

Steinolfson, R. S., S. T. Suess, and S. T. Wu (1982), The steady global corona, *ApJ*, *255*, 730–742, doi:10.1086/159872.

Stone, E. C., A. C. Cummings, F. B. McDonald, B. C. Heikkila, N. Lal, and W. R. Webber (2008), An asymmetric solar wind termination shock, *Nature*, *454*, 71–74, doi:10.1038/nature07022.

Strang, G. (1988), *Linear Algebra and its Applications*, Harcourt Brace Jovanovich.

Sturrock, P. A., and S. M. Smith (1968), Magnetic-Field Structure Associated with Coronal Streamers, *Sol. Phys.*, *5*, 87–101, doi:10.1007/BF00147122.

Suess, S. T., A.-H. Wang, and S. T. Wu (1996), Volumetric heating in coronal streamers, *J. Geophys. Res.*, *101*, 19,957–19,966, doi:10.1029/96JA01458.

Sun, X., Y. Liu, J. T. Hoeksema, K. Hayashi, and X. Zhao (2011), A New Method for Polar Field Interpolation, *Sol. Phys.*, *270*, 9–22, doi:10.1007/s11207-011-9751-4.

Suzuki, T. K. (2006), Forecasting Solar Wind Speeds, *ApJ*, *640*, L75–L78, doi:10.1086/503102.

Tandberg-Hanssen, E. (1974), Solar prominences, *Geophysics and Astrophysics Monographs*, *12*.

Tandberg-Hanssen, E. (1995), *The Nature of Solar Prominences*, *Astrophysics and Space Science Library*, vol. 199, Kluwer, Dordrecht; Boston, doi:10.1007/978-94-017-3396-0.

Tandberg-Hanssen, E. (1998), The History of Solar Prominence Research (Review), in *IAU Colloq. 167: New Perspectives on Solar Prominences*, *Astronomical Society of the Pacific Conference Series*, vol. 150, edited by D. F. Webb, B. Schmieder, and D. M. Rust, p. 11.

Taylor, G. (1950), The Instability of Liquid Surfaces when Accelerated in a Direction Perpendicular to their Planes. I, *Royal Society of London Proceedings Series A*, *201*, 192–196, doi:10.1098/rspa.1950.0052.

Thomas, J. H. (1988), Siphon flows in isolated magnetic flux tubes, *ApJ*, *333*, 407–419, doi:10.1086/166756.

Tomczyk, S., and S. W. McIntosh (2009), Time-Distance Seismology of the Solar Corona with CoMP, *ApJ*, *697*, 1384–1391, doi:10.1088/0004-637X/697/2/1384.

Tomczyk, S., S. W. McIntosh, S. L. Keil, P. G. Judge, T. Schad, D. H. Seeley, and J. Edmondson (2007), Alfvén Waves in the Solar Corona, *Science*, *317*, 1192–, doi:10.1126/science.1143304.

Tóth, G., et al. (2005), Space Weather Modeling Framework: A new tool for the space science community, *Journal of Geophysical Research (Space Physics)*, *110*, A12226, doi:10.1029/2005JA011126.

Tóth, G., B. van der Holst, and Z. Huang (2011), Obtaining Potential Field Solutions with Spherical Harmonics and Finite Differences, *ApJ*, *732*, 102–+, doi:10.1088/0004-637X/732/2/102.

Tóth, G., et al. (2012), Adaptive numerical algorithms in space weather modeling, *Journal of Computational Physics*, *231*, 870–903, doi:10.1016/j.jcp.2011.02.006.

Tripathi, D., H. E. Mason, B. N. Dwivedi, G. del Zanna, and P. R. Young (2009), Active Region Loops: Hinode/Extreme-Ultraviolet Imaging Spectrometer Observations, *ApJ*, *694*, 1256–1265, doi:10.1088/0004-637X/694/2/1256.

Tu, C.-Y., C. Zhou, E. Marsch, L.-D. Xia, L. Zhao, J.-X. Wang, and K. Wilhelm (2005), Solar Wind Origin in Coronal Funnels, *Science*, *308*, 519–523, doi:10.1126/science.1109447.

Vaiana, G. S., J. M. Davis, R. Giacconi, A. S. Krieger, J. K. Silk, A. F. Timothy, and M. Zombeck (1973), X-Ray Observations of Characteristic Structures and Time Variations from the Solar Corona: Preliminary Results from SKYLAB, *ApJ*, *185*, L47, doi:10.1086/181318.

van Ballegooijen, A. A., M. Asgari-Targhi, S. R. Cranmer, and E. E. DeLuca (2011), Heating of the Solar Chromosphere and Corona by Alfvén Wave Turbulence, *ApJ*, *736*, 3, doi:10.1088/0004-637X/736/1/3.

van de Hulst, H. C. (1950), The electron density of the solar corona, *Bull. Astron. Inst. Netherlands*, *11*, 135.

van der Holst, B., I. V. Sokolov, X. Meng, M. Jin, W. B. Manchester, IV, G. Tóth, and T. I. Gombosi (2014), Alfvén Wave Solar Model (AWSoM): Coronal Heating, *ApJ*, *782*, 81, doi:10.1088/0004-637X/782/2/81.

van Driel-Gesztelyi, L., and J. L. Culhane (2009), Magnetic Flux Emergence, Activity, Eruptions and Magnetic Clouds: Following Magnetic Field from the Sun to the Heliosphere, *Space Sci. Rev.*, *144*, 351–381, doi:10.1007/s11214-008-9461-x.

Vásquez, A. M., A. A. van Ballegooijen, and J. C. Raymond (2003), The Effect of Proton Temperature Anisotropy on the Solar Minimum Corona and Wind, *ApJ*, *598*, 1361–1374, doi:10.1086/379008.

Vásquez, A. M., R. A. Frazin, and F. Kamalabadi (2009), 3D Temperatures and Densities of the Solar Corona via Multi-Spacecraft EUV Tomography: Analysis of Prominence Cavities, *Sol. Phys.*, *256*, 73–85, doi:10.1007/s11207-009-9321-1.

Vásquez, A. M., R. A. Frazin, and W. B. Manchester, IV (2010), The Solar Minimum Corona from Differential Emission Measure Tomography, *ApJ*, *715*, 1352–1365, doi:10.1088/0004-637X/715/2/1352.

Vásquez, A. M., Z. Huang, W. B. Manchester, and R. A. Frazin (2011), The WHI Corona from Differential Emission Measure Tomography, *Sol. Phys.*, pp. 16–+, doi:10.1007/s11207-010-9706-1.

Vásquez, A. M., R. A. Frazin, Z. Huang, W. B. Manchester, and P. Shearer (2012), The 3D solar minimum with differential emission measure tomography, in *IAU Symposium*, *IAU Symposium*, vol. 286, edited by C. H. Mandrini and D. F. Webb, pp. 123–133, doi:10.1017/S1743921312004735.

Verdini, A., and M. Velli (2007), Alfvén Waves and Turbulence in the Solar Atmosphere and Solar Wind, *ApJ*, *662*, 669–676, doi:10.1086/510710.

Vial, J.-C., K. Olivier, A. A. Philippon, A. Vourlidas, and V. Yurchyshyn (2012), High spatial resolution VAULT H-Lyα observations and multiwavelength analysis of an active region filament, *A&A*, *541*, A108, doi:10.1051/0004-6361/201118275.

Viall, N. M., and J. A. Klimchuk (2011), Patterns of Nanoflare Storm Heating Exhibited by an Active Region Observed with Solar Dynamics Observatory/Atmospheric Imaging Assembly, *ApJ*, *738*, 24, doi:10.1088/0004-637X/738/1/24.

Wang, Y.-M., et al. (1997), Origin and Evolution of Coronal Streamer Structure During the 1996 Minimum Activity Phase, *ApJ*, *485*, 875–889.

Wang, Y.-M., N. R. Sheeley, Jr., J. H. Walters, G. E. Brueckner, R. A. Howard, D. J. Michels, P. L. Lamy, R. Schwenn, and G. M. Simnett (1998), Origin of Streamer Material in the Outer Corona, *ApJ*, *498*, L165, doi:10.1086/311321.

Wang, Y.-M., N. R. Sheeley, Jr., and N. B. Rich (2007), Coronal Pseudostreamers, *ApJ*, *658*, 1340–1348, doi:10.1086/511416.

Wang, Y.-M., R. Grappin, E. Robbrecht, and N. R. Sheeley, Jr. (2012), On the Nature of the Solar Wind from Coronal Pseudostreamers, *ApJ*, *749*, 182, doi:10.1088/0004-637X/749/2/182.

Warren, H. P. (1999), Measuring the Physical Properties of the Solar Corona: Results from SUMER/SOHO and TRACE, *Sol. Phys.*, *190*, 363–377, doi:10.1023/A:1005289726676.

Warren, H. P., and A. D. Warshall (2002), Temperature and Density Measurements in a Quiet Coronal Streamer, *ApJ*, *571*, 999–1007, doi:10.1086/340069.

Warren, H. P., A. R. Winebarger, and D. H. Brooks (2010), Evidence for Steady Heating: Observations of an Active Region Core with Hinode and TRACE, *ApJ*, *711*, 228–238, doi:10.1088/0004-637X/711/1/228.

Wedemeyer, S., B. Freytag, M. Steffen, H.-G. Ludwig, and H. Holweger (2004), Numerical simulation of the three-dimensional structure and dynamics of the non-magnetic solar chromosphere, *A&A*, *414*, 1121–1137, doi:10.1051/0004-6361:20031682.

Widing, K. G., U. Feldman, and A. K. Bhatia (1986), The extreme-ultraviolet spectrum (300-630 A) of an erupting prominence observed from SKYLAB, *ApJ*, *308*, 982–992, doi:10.1086/164566.

Wiik, J. E., K. Dere, and B. Schmieder (1993), UV prominences observed with the HRTS: structure and physical properties, *A&A*, *273*, 267.

Winebarger, A. R., H. P. Warren, and J. T. Mariska (2003), Transition Region and Coronal Explorer and Soft X-Ray Telescope Active Region Loop Observations: Comparisons with Static Solutions of the Hydrodynamic Equations, *ApJ*, *587*, 439–449, doi:10.1086/368017.

Winebarger, A. R., J. T. Schmelz, H. P. Warren, S. H. Saar, and V. L. Kashyap (2011), Using a Differential Emission Measure and Density Measurements in an Active Region Core to Test a Steady Heating Model, *ApJ*, *740*, 2, doi:10.1088/0004-637X/740/1/2.

Zhao, L., S. E. Gibson, and L. A. Fisk (2013), Association of solar wind proton flux extremes with pseudostreamers, *Journal of Geophysical Research (Space Physics)*, *118*, 2834–2841, doi:10.1002/jgra.50335.

Zirker, J. B. (1985), Prominence hydrogen lines at 10-20 microns, *Sol. Phys.*, *102*, 33–40, doi:10.1007/BF00154035.